

# VNIVERSITAT DE VALÈNCIA

DEPARTAMENTO DE FÍSICA APLICADA Y ELECTROMAGNETISMO



## High-Gradient issues in S-band RF Accelerating Structure for Hadrontherapy accelerators and Radio Frequency Quadrupoles

DOCTORAT EN FÍSICA  
ANNA VNUCHENKO

Supervisors:  
Dr. Ángeles Faus Golfe  
Dr. Benito Gimeno Martínez

Diciembre de 2019



Dra. ÁNGELES FAUS GOLFE, Ingeniero de investigación, Laboratoire de L'Accelérateur Lineaire, Université Paris-Sud 11, CNRS,  
Dr. BENITO GIMENO MARTÍNEZ, Catedrático del Departamento de Física Aplicada y Electromagnetismo de la Universitat de València, y miembro del Institut de Física Corpuscular (IFIC),

CERTIFIQUEN:

Que la present memòria *High Gradient issues in S-band RF acceleration structure for hadron therapy accelerators and Radio Frequency Quadrupoles* ha estat realitzada baix la nostra direcció en el Departamento de Física Aplicada y Electromagnetismo de la Universitat de València per Anna Vnuchenko i constitueix la seua Tesi Doctoral.

I per a que així conste, firmem el present Certificat.

Firmat: Ángeles Faus Golfe

Firmat: Benito Gimeno Martínez



# Acknowledgements

I would like to express my gratitude to the Instituto de Física Corpuscular (IFIC-CSIC) and the University of Valencia (UV) for giving me the opportunity to realize this work in the field of accelerators physics. I am sincerely grateful to my supervisor, Dr. Angeles Faus Golfe, for her always encouraging support and leadership despite the distance during these years. And also to my supervisor, Dr. Benito Gimeno Martinez, for his kind advices, support and a positive look at all the difficulties.

Thanks to all the CLIC-RF group at CERN for the precious scientific and technical support to the high gradient test program and for letting me participate in this research project. I truly want to thank to Dr. Walter Wuensch for supervising me throughout my time at CERN. I appreciate his guidance, great ideas, many useful advice, a lots of discussion and his patience. I would like to thank Dr. Nuria Catalan Lasheras, Dr. Igor Syratchev and Dr. Alexej Grudiev, for the enriching discussions about the preparation, development and analysis of the test. Also to thank Dr. Theodoros Argyropoulos for his first my supervising at CERN and introduction me to RF. And thanks to Gerard McMonagle for constant help with klystron/modulator system and Dr. Benjamin Woolley with LLRF. I am grateful to my Xbox colleagues Benjamin, Stefano, Sam, Jan, Veronica, Thom, Matteo for their help in setting up and running the cavities experiment.

Thanks to the ADAM group for their hospitality and letting me participate in the high-power test of the RFQ used at test bench at CERN, and in particular, to Dr. Luis Navarro for the guiding me with measurements and development of the DAQ, Dr. Michele Caldara for the help of current measurement, Dario Soriano Guillen for constant help in the lab, and also Dr. Alberto De Giovanni and Dr. Yevgeniy Ivanisenko for advice.

Further thanks go to the teams with whom I perform my experiments at Linac4. Special thanks to Dr. Carlo Rossi, Dr. Rolf Wegner and Dr. Suitbert Ramberger for given me chance of carrying on this measurement, their help and advice.

Many thanks to the people directly involved in this project at IFIC: Prof. Juan Fuster Verdu, Dr. Daniel Esperante Pereira, Dr. Marçà Boronat and Cesar Blanch.

Thanks to the European Union's Horizon 2020 research and innovation programme for funding the Optimization of Medical Accelerators (OMA) project under grant agreement No 675265. This Marie Skłodowska-Curie ITN project has been a wonderful start up for my scientific career. Thanks to Prof. Dr. Carsten P. Welsch for coordinating such a wonderful training network. Thanks to all the OMA fellows, a marvellous bunch of extremely enthusiastic, hard-working and committed young researchers, for all the great

---

moments we had together. I hope we will find opportunity to see each other again.

I also would like to thank all persons not mentioned above, especially all collaborators from all over the world, working together under development the linear accelerators, for the discussions with them during workshops and conferences. I would like to thank all the persons I had the opportunity to work and discuss with, even if it was not possible to present the work here, in particular Dr. Andrea Latina for his help in beam dynamics simulation for PRAE project.

Special thanks to my work colleagues and friends Iaroslava Profatilova and Anastasiya Magazinik for your support and share the good and bad moments of our lives. And also many thanks to friends whose names I do not indicate, for your sincere support me in this adventure.

Finally, special and very well-deserved thanks to my family, especially my husband, for their essential support, help and patience throughout the time of this thesis. Even if at distance you have always been present and you have always believed in me.

# Resumen

Durante las dos últimas décadas, dentro del campo de la física de altas energía (High Energy Physics - HEP) se ha avanzado significativamente en el desarrollo de la tecnología de radio frecuencia de alto gradiente (High Gradient Radio Frequency – HG RF). Uno de los principales desafíos está relacionado con la estabilidad de los componentes clave, especialmente las estructuras aceleradoras (AS). Estos avances han permitido aumentar el gradiente de aceleración hasta 100 - 120 MV/m, alcanzando cerca 200 MV/m de campo eléctrico superficial. Las mejoras en el diseño de las AS, junto con las nuevas técnicas de fabricación y una mejor comprensión de los fenómenos que limitan la potencia máxima, están posibilitando la construcción de aceleradores lineales mucho más compactos y eficientes. Existen un gran número de aplicaciones en las cuales se pretende aprovechar las ventajas de los aceleradores lineales de alto gradiente. Esta tecnología se puede extender a múltiples aplicaciones fuera del campo de la HEP, como por ejemplo la construcción de Free Electron Lasers (FEL), aceleradores de dispersión inversa Compton, y aceleradores lineales para aplicaciones médicas e industriales.

Una de las aplicaciones más prometedoras de esta tecnología es el campo de la hadronterapia. El uso de haces acelerados de partículas pesadas (protones o iones), los cuales presentan una deposición de energía muy localizada, permite realizar una cirugía del tumor y evitar daños en los tejidos sanos circundantes. Además, el concepto de aceleradores lineales comienza a cobrar interés gracias a la ventaja de modularidad y rapidez en el control de la energía final del haz, el cual permite realizar en sesiones de tratamiento de menor duración.

Actualmente, los prototipos de AS no superconductoras a 12 GHz, testeados dentro del proyecto CLIC del CERN, han permitido establecer el proceso de fabricación, así como un conjunto pruebas experimentales sistemáticas, a baja y alta potencia. Sin embargo, la operación a alta potencia de las estructuras de RF está limitada por los procesos no deseados, tales como: dark-current, calentamiento de las superficies, estabilidad del vacío, electromigración, multipactor y breakdowns (BD). Esta tesis doctoral se centra en el estudio de los BD como una de las principales limitaciones a la hora de optimizar el rendimiento de los AS, y su relación con los altos campos electromagnéticos producidos en el interior de las estructuras.

Los BDs influyen en el rendimiento de la estructura y la calidad del haz acelerado. Estos eventos conducen a la activación del material, pueden producir daños en la superficie, radiación, deterioro del vacío, e incluso afectar a la frecuencia de resonancia de la estructura

---

o cambian el avance de fase entre las celdas, afectando a la sincronía entre la estructura y las partículas que se quiere acelerar. Los BDs son un fenómeno muy importante que limita el gradiente operativo máximo y la fiabilidad de todo un acelerador. El objetivo consiste en el desarrollo de esta tecnología de alto gradiente de conductividad normal para su aplicación en los diferentes campos multidisciplinarios que pretenden aprovechar sus ventajas.

El diseño de la geometría de la estructura es extremadamente importante para optimizar la eficiencia energética y el funcionamiento del acelerador. Las estructuras, después de la fabricación, tienen que trabajar, inicialmente, a baja potencia y deben condicionarse, aumentando la potencia progresivamente, hasta alcanzar el gradiente operativo máximo. El estudio de los BD permite una mejor comprensión de las limitaciones de los aceleradores de HG, y disminuye el tiempo requerido para el condicionamiento, mejorando el rendimiento de las estructuras. En los últimos años, laboratorios de todo el mundo, han dedicado mucho esfuerzo en comprender la física detrás de este fenómeno. A pesar del progreso en esta área de investigación, la probabilidad y el comportamiento de los BD todavía requiere investigación. En consecuencia es necesario de equipos que incluyan diagnósticos avanzados para la detección y análisis de los BD, como parte de las estructuras del acelerador.

Esta tesis doctoral puede estructurarse en tres partes fundamentales, con el objetivo de: brindar una visión general de la teoría empleada; mostrar los resultados de las pruebas a 3 GHz de AS para aplicaciones en hadronterapia (HT), y los estudios de los BD en los cuádruplos de radiofrecuencia (RFQ) a bajas (352.2 MHz) y altas (750 MHz) frecuencias.

La primera parte se centra en la introducción de los conceptos básicos sobre aceleradores lineales de HG, así como en la definición de sus parámetros más importantes. El gradiente de aceleración puede definirse como el potencial axial por unidad de longitud que proporciona la ganancia de energía a una partícula cargada, a medida que pasa a través del AS y que está directamente relacionada con la intensidad de los campos eléctricos presentes en el eje axial. El factor de calidad  $Q$  y la impedancia  $R$  (shunt impedance) indican la eficiencia de las estructuras para alcanzar dicho gradiente, debido a las pérdidas de energía eléctrica. El diseño de la geometría de la estructura es vital para optimizar estos parámetros y lograr una operación eficiente del acelerador.

El rendimiento del acelerador, generalmente, viene limitado por la frecuencia de los BD o Break Down Rate (BDR), que caracteriza la probabilidad de aparición de un BD en una AS, definido como la relación del número de BD observados durante la operación, dividido por el número total de pulsos de RF enviados a la estructura. La baja probabilidad de BD y la durabilidad, suelen ser indicadores de un buen rendimiento de una estructura HG RF. Las unidades de medida estándar son  $\text{bpp}$  (BD por pulso), o  $\text{bpp}/m$  que se obtiene normalizando este valor a la longitud del sistema acelerador.

Experimentalmente se ha observado una fuerte dependencia del BDR con el gradiente  $E_{acc}$ , y con el ancho de pulso,  $\tau_p$ , descrita por la ley de escala  $E_{acc}^{30} \tau_p^5$ . Esta dependencia puede ser explicada debido a la existencia de defectos y nano protusiones en la superficie interior de la estructura. La fuerte influencia del campo eléctrico conduce al crecimiento de los nuevos emisores que pueden desencadenar BD. Esto degrada el factor de calidad  $Q$

---

de la cavidad y afecta la resistividad superficial del cobre.

Contrariamente al criterio de Kilpatrick, que se utiliza comúnmente para el diseño de AS, el campo eléctrico superficial no permite predecir el límite de gradiente que puede alcanzar una estructura, a pesar de la importancia de esta magnitud en el mecanismo de formación de BD. Este criterio tiene algunas limitaciones porque no incluye la dependencia de la longitud del pulso, ni el BDR a la hora de estimar la probabilidad de aparición de un BD. Hoy en día, el condicionamiento de RF permite llegar a campos más altos, así como los avances en tecnología del mecanizado y limpieza de superficies, junto con los sistemas de ultra alto vacío.

Por esta razón, se deben tener en cuenta otras restricciones al diseñar estructuras HG. Por un lado, el calentamiento de la superficie producido por los pulsos de alta potencia que provoca una degradación de la superficie, aumentando así las posibilidades de BD, especialmente en las regiones donde el campo magnético es más intenso. Por otro lado, se introduce una nueva cantidad conocida como el vector de Poynting modificado,  $S_c$ , que consiste en una combinación de la densidad de potencia real e imaginaria del vector de Poynting. Esta magnitud permite tener en cuenta el acoplamiento de la potencia de RF disipada en los emisores de campo de superficie, y los campos no lineales generados por la emisión de campo. Todavía se requieren estudios adicionales para estimar la influencia del vector de Poynting modificado, y el campo eléctrico superficial asumiendo un gradiente máximo.

Dado que la tecnología basada en aceleradores lineales, conocida como linacs, parece una de las opciones más prometedoras para hadronterapia (HT) por la reducción de tamaño, costo, complejidad y por su mayor eficiencia de trabajo, parte del trabajo se ha centrado en la implementación de la tecnología HG con fines médicos. Las principales ventajas de los linacs radican en la posibilidad de cambiar activamente la energía del haz reduciendo el tiempo de tratamiento debido a la alta frecuencia de repetición. Estas características son ideales para poder tratar órganos móviles permitiendo así el acceso a un mayor número de pacientes.

Basándose en los resultados durante el desarrollo de HG ASs, la Fundación italiana TERA (Fondazione per Adroterapia Oncologica) ha propuesto recientemente un nueva máquina para protonterapia basada totalmente en linacs. La idea principal del proyecto es construir AS de 3 GHz montados sobre un pórtico giratorio y usando un RFQ, de alta frecuencia (HF) (750 MHz) como elemento inyector. Una máquina construida completamente con linacs podría alcanzar el 100 % de transmisión del haz y un funcionamiento sin pérdidas, además, la instalación no requeriría ningún blindaje significativo. El uso de HG en estructuras RFQ también está reduciendo las dimensiones y los costos de construcción. Reducir la longitud total de los aceleradores es muy importante ya que las instalaciones podrían ubicarse en centros hospitalarios, sin requerir grandes instalaciones específicas. Pero los requisitos para poder realizar un tratamiento médico imponen un límite a la probabilidad de BD de  $7.7 \times 10^{-7}$  *bpp/m* en todos los componentes de aceleración para tener menos de un BD por sesión de tratamiento completo. Para proporcionar tales condiciones, se requiere un control del comportamiento de BD en las diferentes etapas de aceleración.

---

En este contexto, la segunda parte de esta tesis doctoral se centra en el estudio de las limitaciones en el rendimiento de los aceleradores de HG para HT, debido a los BD en las estructuras del acelerador. El diseño y la fabricación de un prototipo de HG para linacs de protones de uso médico, ha sido financiado por el grupo de Conocimiento y Transferencia en el CERN. El primer prototipo, una estructura Backward Travelling Wave en S-band (2.9985 GHz) conocida como S-band BTW HT se ha diseñado para lograr un gradiente de aceleración de aproximadamente 50 MV/m, con un campo superficial máximo de más de 200 MV/m, optimizado para protones de 76 MeV de energía. Esto permitiría reducir considerablemente el tamaño del acelerador, tal y como se propone en el proyecto Turning Linac for Proton Therapy (TULIP). El principio de diseño de esta estructura es muy similar a los prototipos CLIC. Ambos están operacionalmente limitados por el campo eléctrico superficial máximo ( $\approx 250$  MV/m) y un BDR máximo ( $\approx 10^{-6}$  bpp/m). La estructura ha sido diseñada, fabricada y probada en el CERN. En esta parte se describe el diseño de RF de la estructura.

Para alcanzar los parámetros nominales de dicha estructura, se realizó el proceso de condicionamiento, sometiénola a una serie de pulsos de RF y aumentando gradualmente la potencia. Las pruebas de alta potencia del AS de banda S se han llevado a cabo en las instalaciones de prueba de S-band en el CERN. El Sbox del CERN ha sido optimizado para probar las estructuras de aceleración y los componentes de RF a mayor potencia. El laboratorio consta de la instrumentación necesaria para medir la potencia incidente, reflejada y transmitida en la estructura. Se utiliza un sistema de control y un algoritmo de operación para mantener el BDR por debajo de un valor máximo. La estructura se condicionó a HG usando el mismo protocolo que para las estructuras CLIC 12 GHz, logrando el gradiente máximo de diseño e incluso superándolo. Este estudio puede servir como punta de lanza del uso de un linac HG para HT. La cavidad está diseñada con un gradiente de más del doble de lo que se ha alcanzado en cavidades previamente probadas a la misma frecuencia. El objetivo principal de este prototipo es explorar los límites de BD de este tipo de cavidades de banda S. La viabilidad de dicha estructura abrirá muchas posibilidades para su uso en diferentes proyectos, principalmente debido al tamaño reducido de la instalación. El programa de prueba de alta potencia se realizó para comprender los procesos físicos asociados con los BD en RF y para determinar los mecanismos que limitan el gradiente y causan daños a la estructura. El rendimiento de la estructura cambia con el tiempo y tiene una fuerte dependencia del gradiente de aceleración y la longitud del pulso. Una vez condicionada y alcanzado el gradiente de diseño, las medidas del BDR se realizaron a diferentes niveles de potencia, manteniendo una longitud de pulso fija. La reducción del BDR indica el estado de condicionamiento de la estructura. Se ha determinado la ley de escala medida para S-band BTW HT en diferentes gradientes, pero el resultado es bastante diferente de la ley de escala empírica para otros prototipos de HG a 12 y 30 GHz. Los experimentos deben realizarse con mayor estadística para evaluar el efecto de los BD en el funcionamiento de la estructura HG.

Se han realizado diferentes estudios para entender mejor las limitaciones de BD en la estructura BTW HT de banda S. El posicionamiento de los BD a lo largo de las múltiples celdas de la estructura ha permitido comprender los factores limitantes del diseño para

---

evitar generar daños en las AS durante la operación. Esto debido a que el diseño RF busca una distribución uniforme de BD en todas las celdas. Para determinar la ubicación de los BD se han utilizado diferentes métodos. Estos métodos fueron adaptados de los utilizados previamente en estructuras de aceleración de banda X. Los resultados obtenidos para la S-Band BTW HT muestran que no hay evidencias de la existencia de ningún *hot spot*. La ubicación de BD está directamente relacionada con la distribución de campo en la estructura.

Otro fenómeno importante que requiere de investigación es la emisión de electrones por efecto de campo y la corriente oscura resultante. Su estudio es importante porque puede causar absorción de energía de RF, ruido de fondo en los monitores de posición del haz y también radiación ionizante. Por lo tanto, se realizaron varias medidas para determinar el nivel de emisiones en las estructura S-band BTW HT. Se ha medido la dependencia de la corriente oscura con la longitud del pulso y la magnitud del campo aplicado observando que el valor disminuye con el tiempo, siguiendo el proceso de condicionamiento. La amplitud de la corriente oscura emitida por la estructura sigue el modelo de Fowler-Nordheim. El *enhancement factor* o factor de amplificación obtenido es comparable a los valores de los prototipos de X-band probados en el CERN. Estos resultados muestran la mejora de la superficie de la AS durante el proceso de condicionamiento, como es habitual en estos casos.

El análisis comparativo de los históricos de condicionamiento del prototipo S-band BTW HT permite reducir los tiempos, con el objetivo de optimizar el rendimiento y minimizar la probabilidad de BD. Un modo de operación estable es necesario para el buen funcionamiento de todos los aceleradores lineales, en particular, para la terapia de protones, ya que éstas requieren de una operación sin BD durante toda una sesión de tratamiento. Después de la prueba de alta potencia se han llevado a cabo mediciones de RF de baja potencia para determinar los cambios de las propiedades de RF de la BTW HT de banda S. Además, también se ha realizado una inspección visual con boroscopio para ubicar los BD y para ver la ocurrencia relativa BD en las diferentes áreas de la superficie interna donde el campo electromagnético alcanzó valores máximos. Estos resultados complementarios confirman la confiabilidad del análisis de datos basado en la diferencia en el tiempo de las señales de RF. Se realizó una comparación detallada de los históricos de condicionamiento para determinar el mejor procedimiento, con el objetivo de evaluar el diseño de RF y la tecnología de fabricación. El proceso de condicionamiento está limitado por el algoritmo, la potencia de entrada disponible, y la velocidad de condicionamiento individual de la estructura. A modo comparativo, se han utilizado diferentes parámetros. Por ejemplo, el gradiente de aceleración no es un parámetro relevante para predecir el mejor rendimiento de la estructura, ya que el rendimiento depende de la influencia de múltiples factores. Otras cantidades, como el campo eléctrico superficial y el vector de Poynting modificado, se han utilizado para describir este proceso. Para poder comparar directamente el comportamiento de los diferentes AS, los resultados se han normalizado a los parámetros nominales, utilizando la longitud del pulso y el BDR. Se han comparado los históricos de condicionamiento con los diferentes parámetros para identificar cual es la mejor opción para hacer dichas comparaciones.

---

En particular, el estudio del comportamiento a largo plazo, de este tipo de AS fue de especial interés, con el fin de encontrar el gradiente máximo para una operación estable, y así estimar el tiempo requerido para completar el proceso de condicionamiento. Los prototipos CLIC y la estructura de la S-band para aplicaciones médicas tienen diferentes requisitos en términos de estabilidad de operación; sin embargo, los resultados de la prueba en S-band AS parecen consistentes con los resultados de los experimentos de las X-band. Todos estos resultados confirman que la BTW HT de banda S garantiza los parámetros necesarios para la hadronterapia, además de dar información adicional sobre la aparición de BD en el NC HG AS con diferentes diseños. El conocimiento adquirido en esta tesis se puede utilizar para desarrollar más bancos de pruebas para AS y componentes RF, a fin de calcular el blindaje necesario para la instalación y realizar más estudios sobre la generación de arcos de vacío.

La última parte de este trabajo está dedicada al estudio de los BD en las RFQ. Las estructuras RFQ se utilizan comúnmente como inyectores, en los principales laboratorios e industrias, donde se utilizan aceleradores lineales de iones. La RFQ representa la mejor opción de transporte entre los haces no agrupados, provenientes de la fuente de iones y los haces agrupados que se requieren en las AS. La tecnología HG, en este tipo de estructura, ofrece una mayor capacidad de carga espacial y la posibilidad de reducir la longitud total de los aceleradores. Para mejorar el rendimiento de las RFQ, es necesario aumentar el gradiente, lo que significa maximizar el campo en las *vane-tip*. Esto se puede hacer, teniendo en cuenta la proporción entre la aceptación transversal, la eficiencia de aceleración, y minimizando el radio de curvatura transversal. Se han adoptado una serie de soluciones de diseño innovadoras con frecuencias y gradientes más altos para minimizar el costo y contribuir al futuro de la industrialización. Se estudiaron dos RFQ, una con alta frecuencia (HF-RFQ a 750 MHz) y otra con baja frecuencia (352.2 MHz). Es importante tener en cuenta que el rendimiento logrado y el comportamiento a largo plazo de estas estructuras se han llevado a cabo por primera vez de manera sistemática en este tipo de dispositivos.

La HF-RFQ es una estructura compleja, que requiere de mayor precisión de mecanizado debido a sus estrictas tolerancias. El HF-RFQ es el RFQ más compacto jamás construido, opera a 750 MHz y es capaz de producir haces de baja intensidad sin pérdidas significativas. Esta estructura tiene aproximadamente el doble de frecuencia que las RFQ existentes. Esta RFQ está diseñada para aplicaciones de baja corriente que requieren pequeñas dimensiones, bajo costo, bajas emisiones de radiación, mantenimiento mínimo, y alta portabilidad. Los primeros HF-RFQ se han construido, como alternativa a los ciclotrones, en la fase de inyección a un linac que funciona a una frecuencia más alta. Su diseño es lo suficientemente general como para ser utilizado en muchas otras aplicaciones, como la producción de radioisótopos médicos y el escaneo con haces de iones, y también para la fabricación de componentes industriales y el análisis de obras de arte.

El estudio de los BD se ha realizado durante la operación y prueba del HF-RFQ utilizado en los experimentos LIGHT e instalado en el área experimental del CERN. El sistema LIGHT fue diseñado para proporcionar un haz de protones de alta calidad con una energía de hasta 230 MeV, necesaria para el tratamiento eficaz de tumores profundos con

---

terapia de protones. Uno de los objetivos de esta instalación es reducir significativamente el costo del tratamiento y poder instalar, dichas máquinas en centros de atención médica pequeños o medianos.

La compañía AVO ha integrado con éxito, las diferentes secciones principales del linac en un primer prototipo. El diseño LIGHT se compone de diferentes tipos de secciones lineales de aceleración, y en una de ellas se encuentra la RFQ. Este prototipo ha sido construido por el CERN, con el apoyo del grupo de transferencia de conocimiento. La RFQ de 750 MHz se ha construido en base a la experiencia previa en el diseño de AS dentro del proyecto Linac4, adaptándola a las tecnologías TERA anteriores y la experiencia en estructuras HG del grupo CLIC del CERN. La frecuencia del RFQ ha sido seleccionada para ser un sub-armónico de 3 GHz como se requiere para la aplicación en una terapia de protones. Esto debido a que las frecuencias más altas disminuyen la aceptación, aumentan la densidad de pérdida de potencia y dificultan el mecanizado de las primeras celdas.

La medición de BDs en este HF-RFQ se realizó durante el condicionamiento con haz de los diferentes componentes de RF. Los datos han sido tomados sin alterar el régimen normal de operación. Inicialmente, los datos de la forma de onda se tomaron con un osciloscopio, y después se desarrolló el sistema de adquisición de datos. Se realizó el estudio primario de la ubicación de BD. El RFQ no está equipado con una configuración de diagnóstico que admita las mediciones de todas las señales necesarias para determinar la ubicación de los BD. Pero aún así, según los resultados obtenidos, se pueden sacar conclusiones sobre la ubicación dominante. En general, hemos probado que este tipo de RFQ son adecuadas para cumplir los requisitos que exigen las aplicaciones de HG.

Otra RFQ que se ha estudiado en esta tesis doctoral es la RFQ de 352.2 MHz, utilizada como parte del complejo de inyectores de Linac4 para el Gran Colisionador de Hadrones (LHC). Su rendimiento a HG y el comportamiento de los BD ha sido el aspecto fundamental de este estudio. El RFQ está diseñado para acelerar un haz H- desde la fuente de iones hasta conseguir los parámetros requeridos, ya que los parámetros del haz de salida del RFQ deben ser compatibles con la *chopper line* existente en Linac4. Los estudios BD en el Linac4 RFQ se han realizado principalmente utilizando señales acopladas en los ejes del sintonizador. Las señales reflejadas y los lectores de vacío se han utilizado como confirmación de la actividad de BD. Estos acoples se usan para monitorizar los campos electromagnéticos dentro de la cavidad RFQ, durante la operación, y para mantener el campo constante. El Linac4 RFQ ha sido operado con diferentes potencias, longitudes de pulso, con y sin haz, lo que hace posible estudiar el comportamiento de la estructura con varios parámetros.

Los datos obtenidos muestran un número creciente, no lineal, de BD durante la operación. Esta alta actividad puede ser causada, no solo por limitaciones del diseño, sino también por factores externos. Cabe destacar el número de BD que se produjo cuando se cambió la longitud del pulso. Esto indica la necesidad de implementar un algoritmo de condicionamiento, que garantice que el BDR y los niveles de vacío se mantienen dentro de los márgenes de operación segura. Las medidas de BD en la RFQ requieren condiciones adecuadas para evitar la influencia de otros factores como el gas, las partículas cargadas provenientes de la fuente de iones, y la potencia reflejada en la estructura. Solo después de

---

la eliminación de estos factores externos, se pudo estudiar adecuadamente el rendimiento de RFQ.

El comportamiento del RFQ durante un evento BD es muy diferente de los estudios hechos a las AS en HG. Sobre la base de las observaciones de los eventos de BD, se desarrollaron técnicas para determinar la ubicación de BD utilizando todas las señales de RF disponibles. También, se han realizado simulaciones de la distribución del campo electromagnético para el RFQ. La zona más interesante está cerca de los iris, donde el campo eléctrico de superficie es el más alto. Los intentos de simular la distribución del campo durante los BD se han realizado como un cortocircuito entre los *vanes* más cercanos.

Los campos durante un BD cambian drásticamente tal y como que se observó en las estructuras previas. Midiendo la frecuencia en las sondas de potencia se puede obtener que las frecuencias no resonantes aparecen durante BD, y los valores dependen de la ubicación. Los BD dividen el volumen en dos áreas: la primera con una variación de frecuencia mínima, y la segunda con un amplio rango de frecuencia. Para explorar este fenómeno en detalle se requieren más medidas, por lo que el DAQ requiere de más cambios. Sin embargo, se ha cuantificado el rendimiento de la RFQ de Linac4 y los principales factores que lo limitan. Se determinó la relación del BDR y el gradiente con y sin has. Estos resultados deberán tenerse en cuenta en el diseño de la próxima generación de RFQ con el objetivo de aumentar el gradiente.

Para completar el análisis del BD, se midió la corriente oscura y el factor Q en ambas RFQ. Generalmente, el funcionamiento de un AS está limitado por los BD, causados por los altos campos eléctricos superficiales presentes en los *vanes*, en el caso de las RFQ. El campo máximo alcanzado, durante las pruebas, produce una corriente emitida considerable (corriente oscura). Esto puede causar absorción de energía del campo RF, y radiación ambiental. Se ha intentado medir las corrientes oscuras, monitorizando el voltaje de la cavidad para diferentes niveles potencia de RF, y también utilizando los detectores de corriente presentes en la línea del haz. Los resultados obtenidos fueron compatibles con las distribuciones de campo del modelo de diseño de la estructura. También se obtuvo el factor de calidad. El propósito de estos experimentos es ver cómo el factor Q se ve afectado por el BD, ya que estos valores varían de un evento a otro. Esta información también se puede utilizar para identificar la ubicación de BD.

Para una mejor comprensión del comportamiento de BD e identificación de los principales parámetros limitantes, se necesita un montaje experimental dedicado, como el que se empleó para la estructura en S-band, ya descrita en la parte anterior. Cabe destacar que, para medir los BD en las estructuras RFQ se ha realizado una actualización de los DAQ en cada uno de los sistemas. El sistema proporciona una interfaz única de monitoreo de parámetros y registro de datos. Los principales cambios realizados se describen en los Apéndices. Esta técnica de medición de BD puede utilizarse en otras instalaciones donde se requiere limitación y control de eventos de BD.

# Abstract

The achievement of high-gradient in the linac structures is a key issue in design facility for high-energy physics and other applications.

This thesis is focused on the study of the high-gradient limitations in the normal-conducting radio-frequency accelerating structures. One of the effects that could appear during high power operation of such structures is the RF vacuum arcs or breakdowns. This occurs due to the high electromagnetic fields in the structure. Such events have an impact on the structure performance and the quality of the accelerated beam. Breakdowns lead to surface damage that can detune the resonant frequency of the structure and change the phase advance between cells which is important for synchronizing the structure with the beam. The achievement of a high gradient in the structures of a linear accelerator is a key fundamental issue in an accelerator installation of hadrontherapy, so it must be studied in detail. Therefore this phenomenon requires a detailed study on the dedicated developed systems.

The Chapter 1 of this thesis includes an overview of the whole theory regarding these studies. A general introduction of the RF theory and the basic concepts related to linear accelerators is given. Some examples of the accelerating structure designs are given, the analysis of which will be carried out in subsequent chapters. The main limiting quantities and the issues related to RF breakdown phenomena are also discussed in detail. The advantages that high gradient technology offers for medical application and a summary of the current activities in the development of high gradient hadron therapy linacs are also described.

In Chapter 2 the high power tests on a 3 GHz prototype for hadron therapy, which have been carried out at the CERN Sbox, are described in detail. The tests have been successfully performed and the maximum operation limit of a linac in terms of maximum achievable fields and breakdown probability have been determined. The data analysis techniques used for localization of breakdowns in this structure are presented in detail in comparison with post-processing results. A statistical investigation of the breakdown occurrences is also made to understand the underlying processes of these events. The data collected have been compared with CLIC X-band RF prototypes results in order to estimate the structure performance. The description of the high-power set-up and the updates are described also in this chapter.

In Chapter 3 a first systematic study of breakdown events in RFQs is presented. Two RFQs designed for different frequencies and applications are considered. The design fea-

---

tures and the relative merits of these structures are discussed. The long term behaviour of the RFQs is also presented. The main changes observed during breakdown events are discussed and a technique of identification of breakdown location is proposed based on these observations. These studies have been applied to determine the breakdown limitations and to predict the structure performances.

The main conclusions are made in Chapter 4. The experimental work presented in this thesis is carried out in order to compare the physics of breakdowns occurring in the high-gradient accelerating structures and RFQs. The final goal of the overall breakdown research is to understand the phenomenon, to maximize the structure performance and to confirm the ability of using high-gradient technologies for various applications.

\* \* \* \* \*

La investigación de estructuras de microondas de alto gradiente en aceleradores lineales es un tema clave en instalaciones de física de altas energías, y en particular en sistemas de física médica basados en hadronterapia.

Esta Tesis Doctoral se centra en el estudio de los problemas que surgen al emplear sistemas de alto gradiente en estructuras aceleradoras de radiofrecuencia no superconductoras. Uno de los efectos que aparecen durante la operación de alta potencia en estos sistemas son los arcos de vacío de RF, llamados *breakdown*. Esto ocurre debido a los altos campos electromagnéticos de RF que aparecen en las estructuras aceleradoras. Tales eventos tienen un impacto en el rendimiento de la estructura y en la calidad del sistema. Los *breakdown* generan daños en la superficie que pueden desintonizar la frecuencia de resonancia de la estructura, y en consecuencia cambiar el avance de fase entre las cavidades aceleradoras, lo cual es importante para sincronizar la estructura con el haz. El logro de un alto gradiente en las estructuras de un acelerador lineal es un tema fundamental clave en una instalación aceleradora de hadronterapia, por lo que debe ser estudiado con detalle.

El Capítulo 1 de esta Tesis incluye una visión general de los aceleradores de partículas. Se presenta una introducción general de la teoría de RF y los conceptos básicos relacionados con aceleradores lineales. Se dan algunos ejemplos de los diseños de estructuras de aceleración, cuyo análisis se llevará a cabo en capítulos posteriores. Los principales parámetros y los problemas relacionados con el *breakdown* también se discuten en detalle. También se describen las ventajas que ofrece la tecnología de alto gradiente para aplicaciones médicas, junto con un resumen de las actividades actuales en el desarrollo de aceleradores lineales de terapia con hadrones.

En el Capítulo 2 se describen con detalle los experimentos de alta potencia en un prototipo de 3 GHz para la terapia de hadrones que se han llevado a cabo en el CERN Sbox. Las pruebas se han realizado con éxito, y se ha determinado el límite máximo de operación de un acelerador lineal en términos de los campos máximos que se pueden alcanzar. Además del acondicionamiento, se han realizado otras mediciones. Las técnicas de análisis de datos utilizadas para la localización de *breakdown* en esta estructura se presentan en detalle en comparación con los resultados del post-procesamiento. También se realiza una investigación estadística de los eventos de ruptura para comprender los procesos subyacentes de estos eventos. Los datos recopilados se compararon con los resultados de

---

los prototipos de RF de la banda X de CERN-CLIC para estimar el rendimiento de la estructura. La descripción de la configuración de alta potencia, y las actualizaciones también se describen en este capítulo.

En el Capítulo 3 se presenta un primer estudio sistemático de eventos de ruptura en sistemas RFQ. Se han estudiado dos RFQ diseñadas para diferentes frecuencias y aplicaciones. Se discuten las características de diseño de estas estructuras. También se presenta el comportamiento a largo plazo de ambas RFQ. Se discuten los principales cambios observados durante los eventos de ruptura, y se propone una técnica de identificación de la ubicación de la ruptura basada en estas observaciones. Estos estudios han servido para predecir los rendimientos de la estructura.

Las principales conclusiones de esta Tesis Doctoral se presentan en el Capítulo 4.. El objetivo final de la investigación general es comprender el fenómeno del *breakdown* para maximizar el rendimiento de este tipo de estructuras, y confirmar la capacidad de usar tecnologías de alto gradiente para diversas aplicaciones, especialmente en Física Médica.

\* \* \* \* \*

Aconseguir un alt gradient en estructures acceleradores lineals (linacs) és un tema clau en el disseny de les instal·lacions en el camp de la física d'alta energia i d'altres aplicacions.

Aquesta tesi es centra en l'estudi de les limitacions de les estructures acceleradores d'alt gradient, de radiofreqüència, no superconductores. Un dels efectes que podrien aparèixer durant l'operació d'aquestes estructures, a alta potència, són els arcs elèctrics de buit o *breakdowns*. Aquests fenòmens es produeixen a causa dels alts camps electromagnètics dintre de l'estructura i tenen un impacte en el rendiment de la mateixa i la qualitat del feix accelerat. Els "arcs de buit" produeixen danys en la superfície que poden afectar a la freqüència de ressonància i canviar l'avanç de fase entre cel·les, modificant un paràmetre important per a la sincronització de l'estructura amb el feix. Per tant, aquest fenomen requereix d'un estudi detallat.

El capítol 1 d'aquesta tesi inclou una visió general de tota la teoria necessària per a realitzar aquests estudis. Primer una introducció general de la teoria de la radiofreqüència i els conceptes bàsics relacionats amb els acceleradors lineals. S'explica breument alguns exemples dels dissenys d'estructures acceleradores, l'anàlisi de les quals es realitzarà en capítols posteriors. També es discuteixen, detalladament, les principals quantitats que limiten l'operació de les estructures i els problemes relacionats amb els fenòmens relacionats amb la radiofreqüència. També es descriuen els avantatges que ofereix la tecnologia d'alt gradient per a l'aplicació mèdica. Finalment, es presenta un resum de l'estat de activitats actuals en el desenvolupament de linacs d'alt gradients per a la teràpia amb hadrons.

Al capítol 2 es descriuen, amb detall, les proves d'alta potència realitzades sobre un prototip de estructura acceleradores, de 3 GHz, per a teràpia amb hadrons, realitzades a les instal·lacions del CERN Sbox. Les proves s'han realitzat amb èxit, obtenint el límit de potència màxima al qual es pot operar aquest tipus de linac, en termes de màxim camp assolible i la probabilitat de produir arcs elèctrics en el buit. Les tècniques d'anàlisi de dades, utilitzades per a la localització dels arcs elèctrics, es descriuen amb detall, comparant-les amb els resultats anteriors. També es descriu els estudis estadístics dels

---

arcs elèctrics en el buit, per comprendre els processos subjacents d'aquests processos. Les dades recopilades s'han comparat amb resultats de prototips RF de CLIC, en banda X, per tal d'estimar el rendiment de l'estructura. La descripció de la configuració del muntatge i les actualitzacions realitzades també es descriuen en aquest capítol.

Al Capítol 3 es presenta un primer estudi sistemàtic del *breakdowns* en estructures RFQs. S'han estudiat dues RFQ dissenyades per a freqüències i aplicacions diferents. Primerament es discuteixen les característiques de disseny i les millores relatives a cada estructura. També es presenta el comportament a llarg termini de les RFQ. Es discuteixen els principals canvis observats durant els *breakdowns* i es proposa una tècnica per identificar la seva ubicació a partir d'aquestes observacions. Aquests estudis han servit per determinar les limitacions de les estructures i predir el seu comportament.

Les principals conclusions es descriuen al capítol 4. El treball experimental presentat en aquesta tesi s'ha realitzat amb l'objectiu de comparar la física darrera el arcs elèctrics en el buit, produïts en les estructures acceleradores d'alt gradient i les RFQ. L'objectiu final de la investigació ha sigut desglossar y comprendre aquest fenomen, per a maximitzar el rendiment de les estructures i demostrar la capacitat d'aplicació d'aquestes tecnologies per a diverses aplicacions.

# Contents

<b>Acknowledgements</b>	<b>i</b>
<b>Resumen</b>	<b>iii</b>
<b>Abstract</b>	<b>xi</b>
<b>1 High-Gradient issues in Normal-Conducting RF structures</b>	<b>1</b>
1.1 High-Gradient Normal-Conducting RF structures . . . . .	2
1.1.1 Particle acceleration . . . . .	2
1.1.2 Main characteristics of RF structures . . . . .	3
1.1.3 Travelling Wave and Standing Wave Structures . . . . .	5
1.1.4 The Radio Frequency Quadrupoles . . . . .	8
1.2 High-Gradient limiting quantities . . . . .	11
1.3 RF structure applications in hadron therapy linacs . . . . .	17
<b>2 Breakdown studies of a S-band HG RF AS for hadron therapy applications</b>	<b>21</b>
2.1 The S-band BTW HT description and main features . . . . .	22
2.2 Low-power analysis of the S-band BTW HT . . . . .	23
2.3 Sbox high-power set-up description and update . . . . .	24
2.4 High-power conditioning and analysis of results . . . . .	30
2.4.1 Conditioning of the S-band BTW HT accelerating structure . . . . .	31
2.4.2 RF breakdown localization . . . . .	34
2.4.3 Investigation of limiting values of modified Poynting vector . . . . .	38
2.4.4 Dark current analysis . . . . .	39
2.4.5 A statistical analysis of breakdowns . . . . .	42
2.4.6 Post-processing analysis . . . . .	45
2.5 Comparative analysis of RF accelerating structures . . . . .	50
<b>3 Experimental studies of RF breakdowns in RFQs</b>	<b>57</b>
3.1 Breakdown measurements in 750 MHz HF-RFQ for hadron therapy applications . . . . .	58
3.1.1 The LIGHT system and the HF-RFQ . . . . .	59

---

3.1.2	Description of experimental area for the LIGHT accelerator . . . . .	61
3.1.3	Description of the breakdown measurement set-up at ADAM test area at CERN . . . . .	63
3.1.4	BD measurements and data analysis . . . . .	66
3.2	Breakdown measurements in 352.2 MHz Linac4 RFQ . . . . .	70
3.2.1	Description of Linac4 and 352.2 MHz Linac4 RFQ . . . . .	70
3.2.2	Update of the data acquisition system of Linac4 RFQ . . . . .	74
3.2.3	Linac4 RFQ breakdown measurement and data analysis . . . . .	77
<b>4</b>	<b>Conclusions</b>	<b>91</b>
<b>A</b>	<b>DAQ upgrade at CERN's Sbox</b>	<b>95</b>
<b>B</b>	<b>DAQ upgrade of HF-RFQ at the ADAM test stand at CERN</b>	<b>99</b>
<b>C</b>	<b>DAQ update of Linac4 RFQ</b>	<b>103</b>
	<b>Bibliography</b>	<b>107</b>

# Chapter 1

## High-Gradient issues in Normal-Conducting RF structures

During the last two decades, there has been a significant progress in the development of High Gradient (HG) technology for High Energy Physics Linear Colliders (HEP-LC) applications. One of the main challenges is related to the reliability of key components, such the Accelerating Structures (AS). The Japanese Linear Collider (JLC) [1], the Compact Linear Collider (CLIC) [2,3] and the Next Linear Collider (NLC) [4] projects have all contributed to progress in increasing the achievable HG from 20–30 MV/m up to 100–120 MV/m. This high accelerating gradient corresponds to approximately 200 MV/m peak surface electric field [3] and has been achieved through an enhanced AS RF designs, an improvement in the fabrication technologies and a better understanding of vacuum RF arcs or RF breakdown (BD) phenomena [5–7].

As a result, prototypes of AS for Normal-Conducting (NC) linear accelerators at High-Frequency (12 GHz) start to have an established process of fabrication and systematic low power and high power experimental tests. However, HG operation of RF structures is limited by the undesired BDs that cause beam losses which in turn can lead to material activation, surface damages, radiation and vacuum deterioration. RF BDs in AS limits the maximum operational gradient and the reliability of the entire accelerator. An effort to deep understanding of this phenomena is ongoing in many labs around the world.

HG-RF technology has also a lot of impact in any other applications apart of HEP-LC, as Free Electron Lasers (FEL), Compton back-scattering accelerators and linacs (linear accelerators) for medical and industrial applications. In the following we will introduce the basics of RF linear accelerators and we will discuss the main limiting parameters, the performance and the applications of the HG-RF AS, in particular for two kinds of RF devices: the Backward Travelling Wave (BTW) AS and the Radio Frequency Quadrupoles (RFQ).

## 1.1 High-Gradient Normal-Conducting RF structures

NC AS are metallic resonant cavities used to accelerate beams of charged particles by means of the interaction of the particles with the electromagnetic (EM) fields confined in such volume. The beam is accelerated (gain energy) by a set of these cavities. AS design depends on the type of particle that is being accelerated and the required final energy. A detailed study of AS is very important for HG NC RF linear accelerators because this component determines the main performances of the facility. We will discuss later in this chapter the main RF parameters and limiting quantities of HG RF structures.

### 1.1.1 Particle acceleration

To accelerate charged particles, EM field oscillate in time in a certain volume with a **frequency**  $f$  as a sinusoidal function in the Radio-Frequency (RF) range from MHz to GHz. The **energy gain**  $W$  of a particle of charge  $q$  longitudinally travelling through the RF structure can be obtained from a simple model using the axial **RF voltage**  $V_0$ , the **synchronous phase**  $\phi_s$  and the **transit time factor**  $T$  according to the Panofsky equation [8]:

$$\Delta W = qV_0T \cos(\phi_s) \quad (1.1)$$

The synchronous phase represents the relative phase of the RF field with respect to the beam and the transit time factor takes into account the time variation of the field during particle transit through the **length**  $L_0$  of the structure. The longitudinal RF voltage is:

$$V_0 \equiv \langle E_{acc} \rangle L_0 \quad (1.2)$$

where the average **accelerating gradient**  $\langle E_{acc} \rangle$  corresponds to the axial potential per unit length which cause a charged particle energy gain during the interaction with the RF fields of the AS. RF AS are typically characterized by their accelerating gradient  $E_{acc}$ , that is directly related to the longitudinal electric field  $E_z$  on the axis of the beam direction, which can be written in terms of the longitudinal position  $z$  and time  $t$  as follows:

$$E_z(z, t) = E_{acc}(z) \cos(\omega t(z) + \phi_s) \quad (1.3)$$

where  $\omega = 2\pi f$  is the **angular frequency**. The energy gain of a charged particle crossing a gap  $L$  is:

$$\Delta W = q \int_{-L/2}^{L/2} E_{acc}(z) \cos(\omega t(z) + \phi_s) dz \quad (1.4)$$

The transit time factor will be defined as

$$T \equiv \frac{1}{V_0} \left( \int_{-L/2}^{L/2} E_{acc}(z) \cos \omega t(z) dz - \tan \phi_s \int_{-L/2}^{L/2} E_{acc}(z) \sin \omega t(z) dz \right) \quad (1.5)$$

and describes the reduction in the energy gain  $\Delta W$  caused by the sinusoidal time variation of the field in the accelerating gap. It takes into account the change in time of  $E_z$  while the particle crosses the cavity with a finite speed.

### 1.1.2 Main characteristics of RF structures

AS consists of a series of periodic cells, aligned in a straight line and coupled by irises of a certain aperture, that store the EM energy and provide a longitudinal voltage given in Eq. (1.2), see Fig. 1.1. The characteristic of AS are determined in term of their figures of merit, some of the more relevant are discussed here.

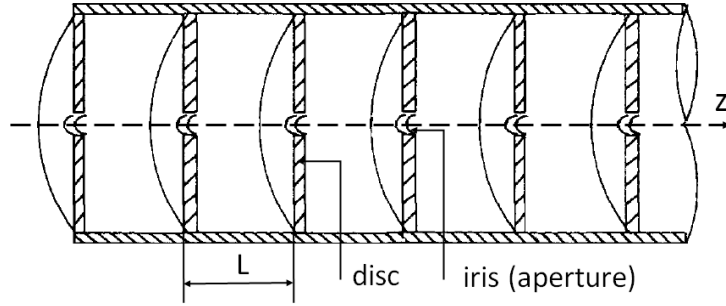


Figure 1.1: Schematic view of an AS.

**Shunt impedance**  $r_s$  is the ratio between the square of the axial voltage  $V_0$  produced and the dissipated power in the cavity walls  $P$ :

$$r_s = \frac{V_0^2}{P} \quad (1.6)$$

it is important to notice that the shunt impedance is independent of the excitation level of the cavity. This energy is dissipated in the cavity walls due to the finite electric conductivity. We could define an **effective shunt impedance**  $r$  (measured in  $\Omega$ ) as the ratio of the average effective electric field squared ( $V_0 T$ ) to the power  $P$  dissipated on the wall surface:

$$r = \frac{(V_0 T)^2}{P} = r_s T^2 \quad (1.7)$$

This depends on the cavity mode, geometry and on the velocity of the particle to be accelerated. Sometimes the **effective shunt impedance per unit length**  $ZT^2$  or  $ZTT$  is also defined and this quantity gives a measure of the effective shunt impedance independent of the cavity length:

$$ZT^2 = \frac{(V_0 T)^2}{P/L} \quad (1.8)$$

**Quality factor**  $Q$  is the ratio between the stored energy  $W$  and the power dissipated per RF cycle multiplied by the RF angular frequency  $\omega$ :

$$Q = \frac{\omega W}{P} \quad (1.9)$$

$Q$  takes into account the losses due to the finite conductivity of the cavity walls. An **external quality factor**  $Q_{ext}$  is a factor that describes the degeneration of  $Q$  due to the generator and diagnostic impedances:

$$Q_{ext} = \frac{\omega W}{P_{ext}} \quad (1.10)$$

A **loaded quality factor**  $Q_{load}$  takes into account not only the power dissipated into the cavity wall  $P$ , but also the extra power lost  $P_{ext}$  when the cavity is connected to a waveguide or when there is a non negligible beam loading:

$$Q_{load} = \frac{\omega W}{(P + P_{ext})} \quad (1.11)$$

this means that

$$Q_{load} = \frac{1}{\frac{1}{Q} + \frac{1}{Q_{ext}}} \quad (1.12)$$

The measurement method currently used for determine  $Q_{load}$  calculates the slope of the decay of the cavity voltage when the pulse is over. This is done by assuming that the decay can be described by the function:

$$V(t) = A \cdot e^{-t/\tau} \quad (1.13)$$

where  $A$  is a constant and  $\tau$  is the cavity time constant. Starting with the logarithm of the cavity voltage which could be defined as  $\ln(V_{cav}) = \ln(A) - \frac{t}{\tau}$ , where  $k = -\frac{1}{\tau}$  is the slope of this curve [9], we have:

$$Q_{load} = -\frac{\omega}{2k}, \quad (1.14)$$

The ratio between the effective shunt impedance and the quality factor  $r/Q$  is a measure of accelerating field for a certain stored energy at a given frequency:

$$\frac{r}{Q} = \frac{V^2}{\omega W} \quad (1.15)$$

The  $r/Q$  thus simply quantifies how effectively the cavity converts stored energy into acceleration. The  $r/Q$  is a pure geometric qualification factor and is independent of material and machining quality.

**Coupling factor**  $\beta_c$  of a waveguide to a cavity system is a measure of how much power coming from the power transfer line (external load) is being used to feed the cavity. The coupling factor is given by the ratio of  $Q$  over  $Q_{ext}$ :

$$\beta_c = \frac{Q}{Q_{ext}} = \frac{P_{ext}}{P} \quad (1.16)$$

Substituting Eq. (1.16) into Eq. (1.12), we find:

$$Q_{load} = \frac{Q}{(1 + \beta_c)} \quad (1.17)$$

When  $\beta_c < 1$  the waveguide and the cavity are *undercoupled*. When  $\beta_c > 1$  the waveguide and the cavity are *overcoupled*. When  $\beta_c = 1$  the waveguide and the cavity are *critically coupled*, and then  $Q = Q_{ext}$  and  $Q_{load} = Q/2$ .

The quantity of power reflected by the coupling slot, is given by the **reflection coefficient**  $\Gamma$ :

$$\Gamma = \frac{1 - \beta_c}{1 + \beta_c} \quad (1.18)$$

To have a matched state in the critically coupled case, we need  $\beta_c = 1$  and  $\Gamma = 0$ . This means that the incident power from the generator delivered into the cavity through the input power coupler is maximum.

The cavity not only receive an input wave from the generator, but reflects a wave back through the coupler. The **effective reflective voltage** and power in the input to the AS is the sum of the direct-reflected wave from the coupler and the reflected wave from the cavity. A detailed explanation can be found in [8].

Almost all of the fundamental RF parameters described before are frequency dependent. Assume an NC RF cavity with fixed accelerating gradient, fixed total energy gain and fixed total length. The transit-time factor and the fields are independent of frequency. The power dissipated into the cavity wall scales as  $f^{-1/2}$ . Therefore, higher frequency gives reduced power loss. Quality factor is also depend as  $f^{-1/2}$ . The effective shunt impedance per unit length scales as  $f^{1/2}$ , so shunt impedance increases at higher frequency. Consequently, NC AS operating at high frequencies require less power. The operating frequency  $f$  have to be selected in the process of optimizing the structure parameters. But a significant limitation comes from technical reasons like the availability of the power supply.

### 1.1.3 Travelling Wave and Standing Wave Structures

Different classifications of structure designs can be found in [10], but we will focus in this particular case on Travelling Wave (TW) and Standing Wave (SW) structures.

#### Travelling Wave Structure

TW AS is a kind of uniform cross-section waveguide structure with a periodic disk loading in which the RF power enters into the cavity through an input coupler, flows consistently along each cell to an output coupler. Typically, the end of the structure is connected to a matched power load. A schematic view is shown in the left part of Fig. 1.2.

The speed of the accelerated particles is synchronized with the RF **phase velocity**:

$$v_{ph} = \frac{\omega}{k} = 2\pi \frac{f}{k} \quad (1.19)$$

this is the velocity which represents the proportionality between the angular frequency  $\omega$  and the wavenumber (or angular wave number)  $k$ .

After selecting the operating frequency, the dimensions of the cells are determined for a given phase advance per cell as:

$$\Delta\phi = k(f) \cdot L_{cell} \quad (1.20)$$

where  $L_{cell}$  is the length of the cell or the distance between two irises. The velocity at which the RF power transmit through TW AS is the **group velocity**  $v_g$  defined as:

$$v_g = \frac{d\omega}{dk} = 2\pi L_{cell} \frac{df}{d(\Delta\phi)} \quad (1.21)$$

The group velocity determines the **filling time**, which is calculated as the time for the wave propagation from input to output end of the structure of length  $L$ :

$$t_{fill} = \int_0^L \frac{dz}{v_g(z)} \quad (1.22)$$

In a **Constant-Impedance** (CI) TW AS with uniform cell geometry [8], the RF power and the electric field decay along the wave propagation with constant  $v_g$ , therefore the filling time is:

$$t_{fill} = \frac{L}{v_g} = \alpha L \frac{2Q_{load}}{\omega} \quad (1.23)$$

where  $\alpha$  is the field attenuation per unit length.

In case of a **Constant-Gradient** (CG) TW AS, the accelerating field is constant along the cells. Therefore, for a constant field, the TW power and also the group velocity decrease linearly with beam direction. To achieve the CG design, the iris radius have to be tapered. The acceleration gradient,  $E_{acc}$ , per unit length of a CG TW AS is calculated by

$$E_{acc} = \sqrt{\frac{P_{in} r_s (1 - e^{-2\alpha})}{L_0}} \quad (1.24)$$

where  $P_{in}$  is the input RF power. The main advantages of CG TW AS is the lower value of the peak surface field for the same energy gain.

## Standing Wave Structure

A SW pattern can be obtained by simply closing both sides of the disc-loaded structure. In this case, the power is fed a single coupler and propagates with the same velocity along all the cells of the AS. The multiple wave reflections from the structure ends build a SW that corresponds to the electromagnetic eigenmodes. The additional boundary conditions suggest perfectly conducting walls with discrete frequencies and phase changes. The fields of adjacent cells couple via coupling holes or through properly designed coupling slots.

The N-cell structure behaves as a system composed by N coupled oscillators with RF modes which characterized by a cell-to-cell phase advance ( $n\pi/N$ ). The frequency of the n-th mode can be calculated from the dispersion formula:

$$w_n = \frac{w_0}{\sqrt{1 + k \cos(n\pi/N)}}, \quad n = 1, 2, \dots, N \quad (1.25)$$

where  $w_0$  is the frequency of the uncoupled single cells and  $k$  is the strength of the cell-to-cell coupling. Therefore a cavity with a larger number of cell  $N$  has more modes in the same frequency range and consequently the smaller frequency difference between the nearest modes.

The **filling time** is the time that it takes to build-up the fields and is given by the following expression:

$$t_{fill} = \frac{Q_{load}}{w} \quad (1.26)$$

The cavity cells are filled uniformly in time. The value of filling time is typically in the order of  $\mu s$ .

Fig. 1.2 illustrates the filling process of the SW and TW structures. TW AS is filled in space, which means that basically cell after cell is filled with power. The fields in SW AS increase in time almost simultaneously in all cells.

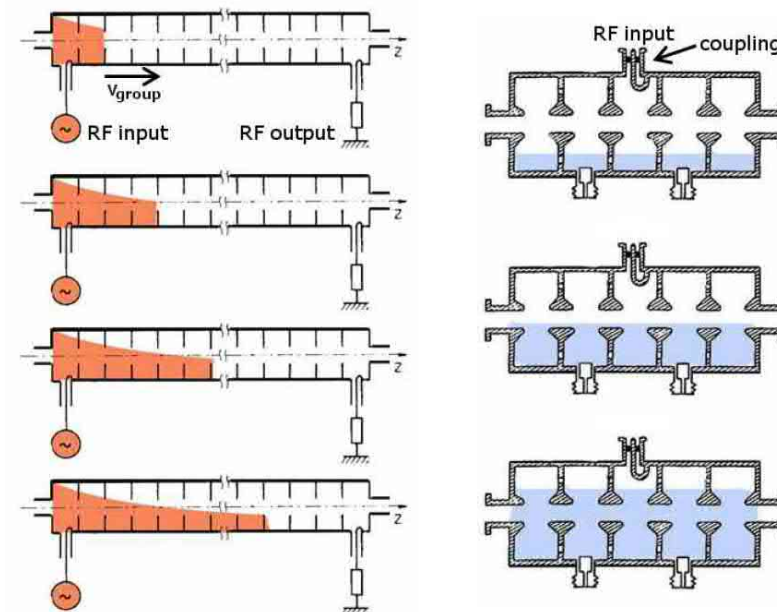


Figure 1.2: Schematic illustration of a TWS (left) and SWS (right).

## Backward TW structure

In order to improve the structure shunt impedance, a novel design taking as starting point the TW AS known as Backward TW structure (BTW) could be introduced. The BTW AS combines the advantages of TW and SW. The main characteristic of this structure is the presence of a backward magnetic coupling, obtained by the aperture of the coupling holes in the wall between successive cells, insuring a high shunt impedance [12]. Another feature of a BTW is the absence of coupling cells which makes the structure more compact in the transverse plane and leaves space for the cooling channels. AS also has shorter filling time. A schematic mechanical drawing of a BTW prototype [13] is shown in Fig. 1.3.

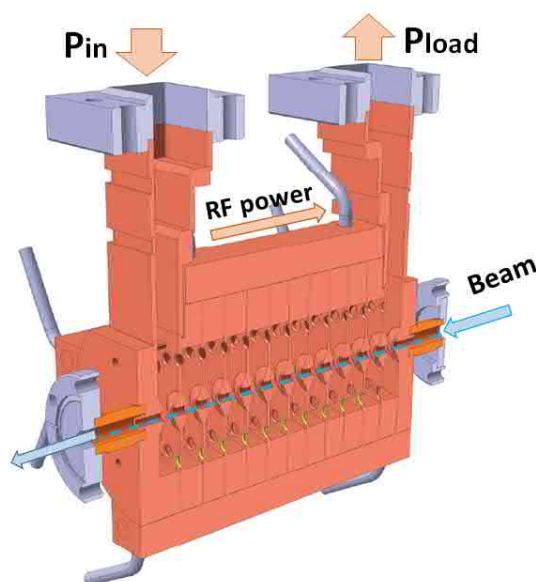


Figure 1.3: Cut view of a BTW prototype. The arrows indicate the direction of RF power and beam in structure where  $P_{in}$  is the input RF power and  $P_{load}$  is power dumped into the RF load.

### 1.1.4 The Radio Frequency Quadrupoles

The RFQ is a linear accelerator which focuses, bunches and accelerates a continuous beam of charged particles with high efficiency and emittance preservation. The focusing as well as the bunching and acceleration are performed by an RF electric field [14]. The RFQ is especially suited for the acceleration of beam with low velocities in the range about 0.01-0.06 times the speed of light.

A RFQ is composed of a cavity loaded with four conducting electrodes located along the beam axis and therefore forced to resonate in the  $TE_{210}$  mode [15,16]. The resonant frequency of an RFQ and beam dynamics is generally defined by the geometry of the electrodes. Basically, the resonators can be divided into two different types: the 4-rod and

the 4-vane RFQs. Other structures (split coaxial, double H) are not considered here. The main differences concern the RF mode and the geometric form of the resonators and of the quadrupole electrodes. An example of the two types of RFQs is shown in Fig. 1.4.

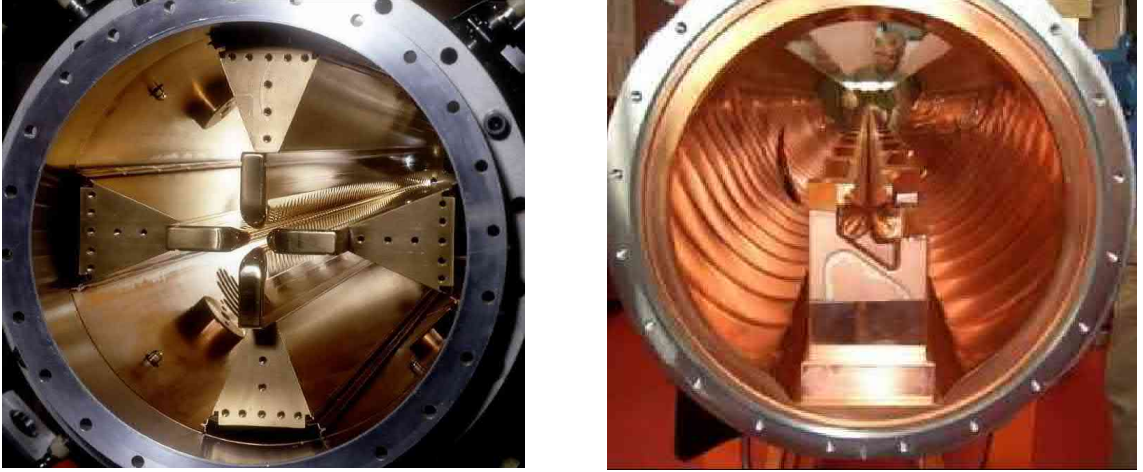


Figure 1.4: Inside view of the 4-vane CERN RFQ2 [17] (left) and 4-rod SARAF RFQ [18] (right).

The **4-vane RFQ** consist of four vanes symmetrically placed within a cavity. The transverse electric field is located near the vane tips and the magnetic field, which is longitudinal in the interior of the cavity, is located mostly in the four outer quadrants. This type of RFQ has high efficiency, low energy losses and can be used for a frequency range from about 200 MHz up to 750 MHz.

The **4-rod RFQ** is composed of rods placed conversely in the centre of the cylindrical cavity by holding bars. This type of RFQ is non-symmetric and a simple mode structure that is easy to manufacture (see Fig. 1.4: right). Each cell is a resonator and their dimensions are independent from the frequency. The electric field is concentrated near the rods, and the magnetic field is near the inductive stems. The current flows along the base from one stem to the next. This can lead to some problems with end cell due to strong current in the holding bars and occur some thermal expansions issues. Usually the 4-rod RFQ is preferred at frequency below 200 MHz because of its compact size. At higher frequencies, the rods become smaller and are difficult to manufacture.

The principle of operation is similar in all types of RFQ's. The tips of the vanes have ripples or longitudinal modulations as shown in Fig. 1.5. The acceleration is performed by periodically modulating the electrodes in the longitudinal direction. The potential on the tips of the vanes  $V_{vane}$  at a given frequency  $\omega$  is:

$$V_{vane} = \pm \frac{V}{2} \sin(\omega t). \quad (1.27)$$

where  $V$  is a voltage applied to the electrodes. The ability to focus and accelerate the beam improves with higher vane tip voltage. The limit is constrained by the peak field

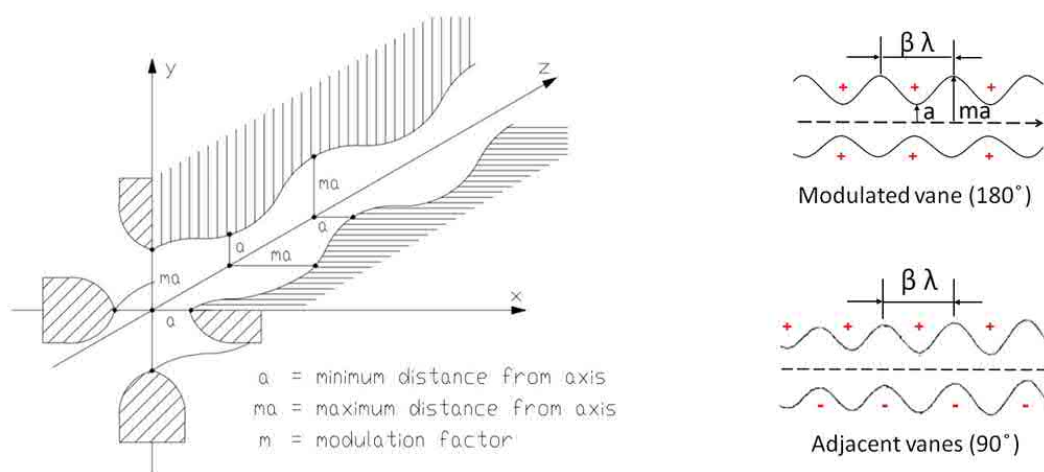


Figure 1.5: Longitudinal modulation (left) and pole-tip shape in the  $x$ - $z$  plane (right) of the RFQ electrodes.

that can be sustained between the vane tips as it leads to BDs. The aperture  $a$  and the modulation parameter  $m$  determine the focusing strength of RF quadrupole field generated by alternative voltage on the electrodes over a period length equal to  $\beta\lambda$ . Accordingly, the transverse component of electric field is constant along the length, but the longitudinal component changes sign every  $\beta\lambda/2$  [14].

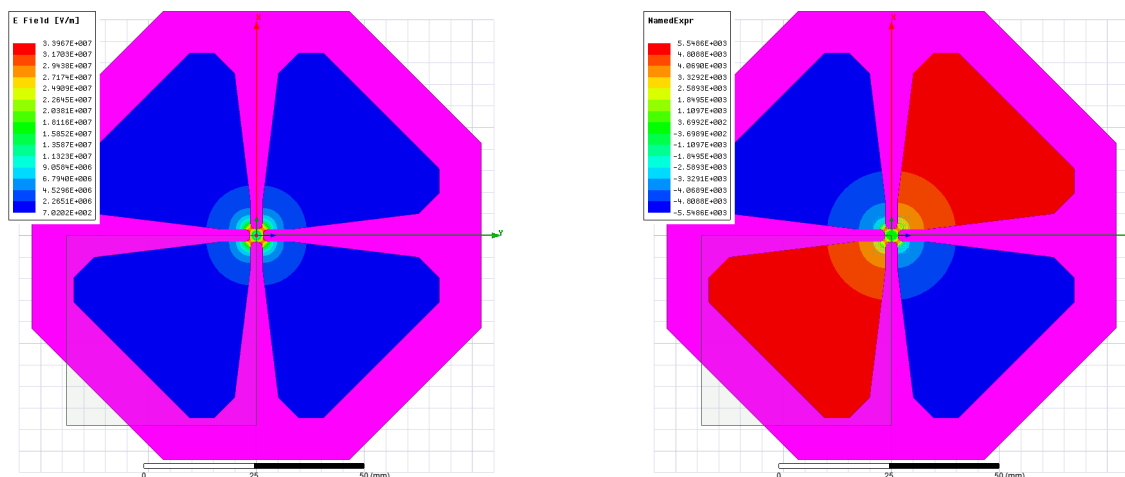


Figure 1.6: Quadrupole mode of electric  $E_z$  (left) and  $z$ -component of magnetic  $B_z$  (right) field.

Nowadays, the RFQ generates up to 35 MV/m surface electric field between inter-vane gaps. This high electric field provide strong focusing for non-relativistic particle beam. The Fig. 1.6 presents the field distribution in the transverse section of common quadrupole mode. The real RFQ operating mode is not a pure  $TE_{210}$  due to the vane tip modulation

but the axial field strength is much smaller than the focusing field. The amplitude of the longitudinal field component  $E_z$  is proportional to the depth of the modulation  $m$ .

The RFQ is mainly used as an intermediate section that matches the beam from an ion source to higher energy accelerator. Therefore it has to be able to accept a low energy beam with strong space charge which occurs during beam bunching. Non-linear fields lead to emittance growth. High peak fields provide higher acceptance and greater space charge capability. But high vane tip voltage imposes restrictions on tighter alignment tolerances during manufacture, increases power consumption and affects the BDs probability. Careful optimization of the RFQ's geometry is therefore necessary to achieve the higher accelerating gradient and minimum RF power consumption.

The compact size, the loss-free operation, the minimum shielding and the efficient RF focusing features make RFQ one of the most important accelerator cavity structures in modern ion linear accelerator technology.

## 1.2 High-Gradient limiting quantities

During high power operation of HG AS the following effects could appear:

- Dark currents - electron emission from the cavity surface under influence of RF fields which can be accelerate over longer distances.
- Pulsed surface heating - an effect on a surface temperature. The heat generated by an intense RF pulse on the metal surface can cause the surface currents that lead to cyclical stress and damage the surface.
- Dynamic vacuum - an effect related to field current that desorbs gasses and cause pressure rises during the RF pulse.
- Electromigration - an effect of surface currents that cause cyclical stress and break up the surface.
- Multipactor - discharge that can appear in RF devices working under high vacuum conditions. An initial set of electrons can couple to the electromagnetic fields describing resonant trajectories and colliding repeatedly with material walls. Under certain conditions, each collision can produce new secondary electrons in a process leading to an exponential growth of the electron population [21].
- BD - an RF initiated surface plasma process.

This thesis will focus on BD studies. BDs are the major limitation in the performance achievement of a HG NC AS. These BDs are due to intense EM fields on the walls of the structures. Important effort has been devoted in last years to understand the underlying physics of this phenomenon. Despite the significant progress made in this area of research, the occurrence and behaviour of the BD still requires dedicated R&D studies. The BDs have a negative effect on the normal operation of the cavities. They damage the inner

surface of the AS and degrade their performance during long term operation [22]. Fig. 1.7 shows a photograph of a crater created by BDs in an X-band RF AS, taken using a scanning electron microscope.

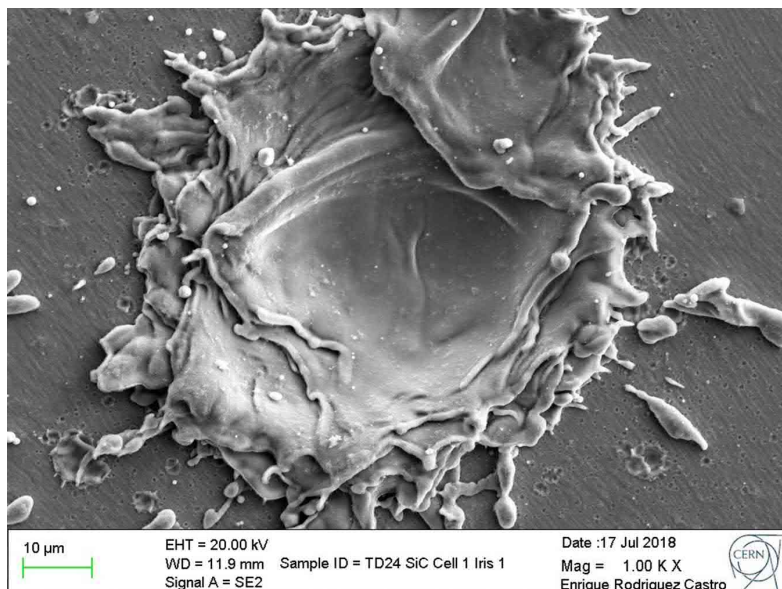


Figure 1.7: Crater provoked by a BD in an X-band RF AS (TD24SiC N1 tested at CERN).

The RF BDs in AS interrupts the RF power flow and transversely kicks the beam leading to emittance growth or even the loss of the beam [20]. The BD is activated by defects, imperfections or dislocations in the inner surface of the ASs. Crystalline structures like copper, generally used to build the cavities, are not too strong and susceptible to be damaged by the application of strong external EM fields. The application of an external EM field stress the surface and causes new defects.

Prior to the occurrence of a BD, a series of preceding processes take place: the high EM field causes electrons and then ions emission from the surface to the vacuum due to the strong heating of the surface area, building up a plasma or ionized gaseous substance that becomes increasingly electrically conductive. The emitted current from the plasma is accelerated by the incoming RF fields resulting in an impedance mismatch. This leads to the development of an arc discharge. An RF BD suddenly changes the electric parameters of the structure, conducting to large reflection back to the RF source and a termination of the transmitted power. The strong EM-field can potentially damage the structure and high-power RF components and RF sources.

To characterize the probability of BDs appearance in an AS, the concept of **Break Down Rate** (BDR) is commonly used. The BDR is defined as the ratio of the number of BDs observed during the operation compare to the total number of RF pulses sent to the structure during the measurement. Low BDR and long lifetimes use to be concomitant indicators of a HG performance of an RF structure. The units of measurement are *bpp* (BD per pulse) or *bpp/m* which is obtained by normalizing the BDR to AS length.

### The Kilpatrick's criterion

The AS generates a strong EM field, specially formed at an operating frequency  $f$ , to ensure good energy efficiency. High electric field level is considered to be one of the main causes of vacuum BDs. The **Kilpartick criterion** is often used as basis for **peak surface electric field limit**. The criterion results from experimental data and relates surface electric field  $E_k$  with the frequency following the expression [23, 24]:

$$f[MHz] = 1.64 \cdot E_k^2[MV/m] \cdot e^{-8.5/E_k[MV/m]} \quad (1.28)$$

Nowadays RF conditioning allows to reach higher fields than Kilpatrick's observations. This result is influenced by the latest technology in the surface machining and cleaning, together with systems achieving extremely high vacuum. This criterion has some limitations because it does not include the dependence from pulse length and BDR to estimate the sparking probability. Nevertheless, this relation is still used as a guideline for the design of structures with high-duty cycle or CW systems at frequencies lower than 1 GHz.

### The Fowler-Nordheim field emission law

The **field emission** (FE) is an important part of the BD's process. It is considered as a pre-BD phenomenon, and is related to the maximum achievable field. During normal operation when the RF field is inside the AS, electrons are emitted from the surface's micro-protrusions which is referred as current. These protrusions locally change the electric field. As a consequence, the electron emission can be enhanced by the shape and the size of the field emitters. This phenomenon is described by so called **Fowler–Nordheim law** [25, 26] that gives the **electron current density**  $j_{FE}$  as a function of the external electric field  $E_s$  [V/m] and the work function of the metal atoms  $\phi$  [eV] in a single RF cycle:

$$j_{FE}[A/m^2] = 1.54 \times 10^{-6} \cdot 10^{4.52 \phi[eV]^{-1/2}} \cdot \frac{E_s[V/m]^2}{\phi[eV]} \exp\left(-\frac{6.53 \times 10^9 \phi[eV]^{3/2}}{E_s[V/m]}\right) \quad (1.29)$$

Small protrusions grow up on the surface and modify the electric field locally  $E_{loc}$  with an enhancement factor  $\beta_{FE}$  which is defined as:

$$\beta_{FE} \equiv \frac{E_{loc}}{E_s} \quad (1.30)$$

Local field enhancement factor takes into account the surface imperfections, roughness and impurities, that increase the effective surface field. These geometry of the surface imperfections are the main contribution of electron emission. Substituting Eq. (1.30) into Eq. (1.29), the resulting field emitted current  $I_{FE}$  can be derived as follows:

$$I_{FE}[A] = A_e \frac{1.54 \times 10^{-6} \cdot 10^{4.52} \phi[eV]^{-1/2} (\beta_{FE} E_s[V/m])^2}{\phi[eV]} \times \exp\left(-\frac{6.53 \times 10^9 \cdot \phi^{3/2}}{\beta_{FE} E_s[V/m]}\right) \quad (1.31)$$

where  $A_e$  is an effective area of field emitters.

Following this theory, the field emission currents cause pulsed local heating of the surface which acts as a trigger of vacuum arcing. A detailed description of the different stages of the vacuum arc formation can be found in [27].

### Power flow and modified Poynting vector

Based on experimental observations, a phenomenological **power flow**  $P/C$  criterion has been proposed to define the level of conditioning of AS [28]:

$$\frac{P\tau_p^\alpha}{C} < constant \quad (1.32)$$

where  $P$  is the RF power flow through the AS,  $\tau_p$  is the pulse length,  $C$  is the minimum inner cavity circumference that is usually determined by iris aperture and  $\alpha$  - a material dependent parameter, which is around 1/3 [29] for the copper. This factor  $\tau_p^{1/3}$  has been included to fulfil the scaling law between the power (or gradient) and the pulse length for a fixed BDR. According to this criteria, structures with smaller aperture allow lower power flows, but at the same time higher surface electric fields. The power flow criteria is suitable only for TW structures, since the power flow in SW structures is close to zero.

The RF power density is described by the **Poynting vector**  $\vec{S} = \vec{H} \times \vec{E}$ . The magnetic field induced in the vicinities of the field emitter is proportional to the emitted current. Because of the non-linearity of the field emission current with the field, a **modified Poynting vector**  $S_c$  is used to represents the directional energy flux density of an EM-field and can be defined as:

$$S_c = \|\text{Re}(\vec{S})\| + g_c \|\text{Im}(\vec{S})\| \quad (1.33)$$

where  $\vec{S}$  is the complex Poynting vector, and  $g_c = 1/6$  is a weighting factor introduced in order to quantify that the active power flow and field emission power flow are in phase and have a maxima at the same time. This coefficient is adjusted to best match the experimental results obtained in massive structures [30].  $S_c$  also includes the observed frequency scaling.

The field emission currents from potential BD sites cause local pulse heating with an increasing density of the field by evaporated neutral atoms. The maximum attainable temperature corresponds to the melting temperature of the tip, which will result in a BD. The goal of cell design optimization is to reduce the value of  $S_c$  and at the same time the amount of RF power for a given accelerating field that provide a high accelerating gradient with a low BD risk. The modified Poynting vector  $S_c$  can be calculated at any point of a structure. This supports the identification of the regions which are more sensitive to the BD process. In the particular case of the 12 GHz CLIC HG AS, this quantity should

not exceed the value of  $5 \text{ MW/mm}^2$  to have a BDR smaller than  $1 \times 10^{-6}$  bpp/m with a pulse length of 200 ns [32]. The threshold have to be calculated by rescaling the data to the appropriate pulse length.

Quantitative high gradient limits such as  $P/C$ , and  $S_c$  provide a method for comprehensive and thorough analysis and comparison the data from numerous AS tests, and gives guidance in the design of HG AS. The  $S_c$  explains the experimental data related to the HG limit due to the BDs, but not the reason of their appearance in normal operational regime.

### Pulsed surface heating and other related limitations

NC-AS cavities are optimized for a maximum accelerating gradient at a given incident power. The shape of the inner walls is important to minimize the peak surface electric field  $E_s$  which limits performance. Smooth shape of nose cones near the beam pipe are required where the  $E_s$  is at maximum. The peak electric and magnetic field and Poynting vector are important constraints in cavity design. The quantities are usually computed by EM solver codes as ANSYS HFSS [33] or CST [34]. Fig. 1.8 shows the distribution of electric, magnetic and modified Poynting vector fields normalized to an axial field of 1 MV/m in the cell volumes of a 3 GHz cavity for proton therapy as a matter of example.

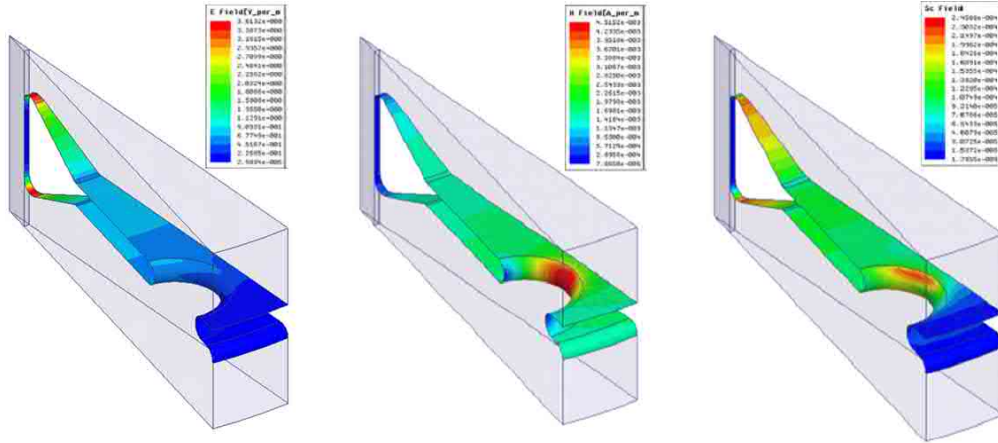


Figure 1.8: Distribution of the electric (left), the magnetic (middle) and the modified Poynting vector (right) fields normalized to an axial field of 1 MV/m in the regular cell section of the 3 GHz cavities from HFSS simulations (1/32 azimuthal symmetry).

Based on the these calculations, we can observe that the magnetic field  $H$  (Fig. 1.8: middle) is the largest on the exterior walls causing **pulse surface heating**. Therefore, a reliable water cooling system is required to maintain a constant field distribution. Pulsed surface heating  $\Delta T$  leads to material fatigue and is proportional to square root of pulse length and square root of peak magnetic field [35]:

$$\Delta T = \sqrt{\frac{\mu_0}{2\pi} \frac{\omega \tau_p}{\sigma k \rho c_H}} \hat{H}^2 \quad (1.34)$$

where  $\hat{H}$  is the maximum surface magnetic field,  $\tau_p$  is the RF pulse length,  $\rho$  is the material density,  $c_H$  is the specific heat at constant strain [ $J/kg K$ ],  $\mu$  is the vacuum permeability and  $k$  and  $\sigma$  are the thermal and electric conductivities respectively.

The maximum field can be optimized by redesigning the geometry. The limit could be applied to any cavity and any mode by calculating the EM field and pulsed temperature rise. For instance in the case of CLIC AS, the damage threshold is observed below  $\Delta T = 56$  K [36].

From equation (1.34) follows that the value of the gradient is limited by the pulse length  $\tau_p$ . In the case of copper we have:

$$\tau_p < \left( \frac{\Delta T_{max}}{4 \cdot 10^{-17}} \right)^2 \frac{1}{f E_{acc}^4} \quad (1.35)$$

The pulsed surface heating is proportional to the power flow  $P$  and the square root of the pulse length  $\tau_p$  using  $P \propto E_{acc}^2$ . According to the latest experimental results obtained during the conditioning of 12 GHz AS, the BDR follows the next scaling law [37]:

$$BDR \propto E_{acc}^{30} \tau_p^5 \quad (1.36)$$

This power-law was established on the result of the experimental data and does not contain the fundamental physics of the breakdown process. Therefore it is not necessary to consider it as a standard.

Since BDR depends on the accelerating gradient following the scaling law based on Eq. (1.36), accordingly BD activity has an impact on the temperature rise. The application of a high electric field to a metallic surface results in ion bombardment of the surface and the creation of craters. High magnetic fields can also cause surface cracking, which may behave as field emitters. This degrades the cavity quality factor  $Q$  and affects on the surface resistivity of copper.

Optimization of the cavity geometry have to be performed to get the required characteristics of the AS, which simultaneously balances surface fields, power flow, input power and other important parameters. The choice of materials, the manufacturing process and the cleaning procedures have to be taken into account since it has significant influence on the final performance. In summary, AS design has a significant impact on the total cost of the facility. Linacs have specific issues: the cost is proportional to the length of the facility but the length reduction of the AS has an inversely proportional influence on the cost of fabrication and the RF power cost. Linac layout depends on many factors, such as cost of the acceleration elements, diagnostics, support stand, vacuum system and location. These parameters should be include in the optimization process.

### 1.3 RF structure applications in hadron therapy linacs

**Hadron therapy** (HT) is a Radiation Therapy (RT) technique using proton or ion beams to treat cancer which provide precise and reliable treatment of tumours. The main advantage of HT lies in the unique physical properties of the charged hadrons, protons and carbon ions in particular, allowing them to penetrate into tissues and leave the maximum energy at the end of their path according to the Bragg curve [38]. Schematic view of Bragg peak for different particle are presented in Fig. 1.9. A flat dose distribution over the depth of the tumour can be achieved by modulating the Bragg peak [39,40]. The high accuracy of HT makes it suitable for treating tumour close to critical organs and for children.

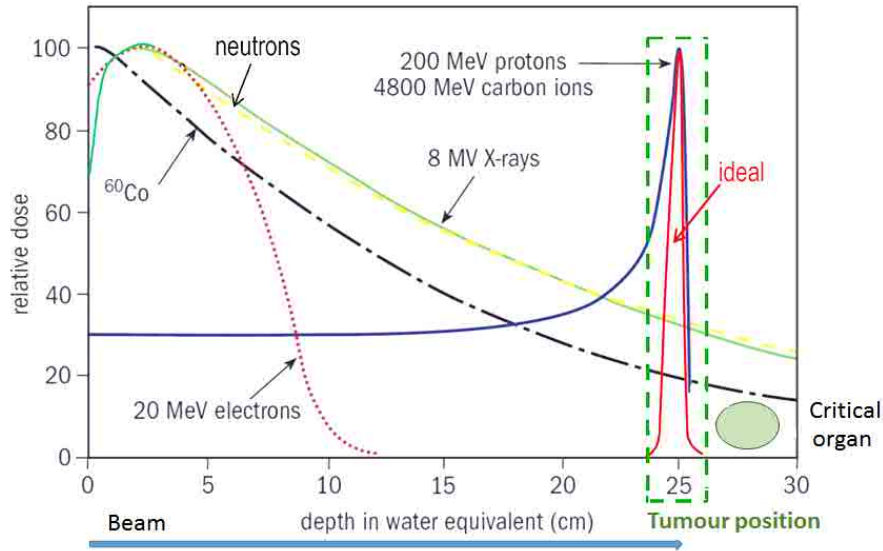


Figure 1.9: Dose distribution in water depth of different particle beams.

In the recent years the number of HT facility has rapidly increased. This is due to the fact that the number of patients needing treatment increase every year and modern equipment helps in the treatment. Cancer is the second leading cause of death globally and is estimated to account for 9.6 million death in 2018 [41]. To the present day, a total of 94 particle therapy facilities worldwide are operational, 44 are under construction and 21 are in a planning stage [42]. Most clinics are located in USA, Europe and Japan. In particular, carbon therapy is becoming a commonly accepted treatment option and the number of the centres has been growing in recent years. The cumulative number of proton and carbon ion centers as a function of time is shown in Fig. 1.10.

The facilities have to satisfy the demands of the medical requirements for the treatment procedures. The beam energy ranges have to be between 70-230 MeV for protons and 100-430 MeV/amu for carbon ions. Low emittance and high energy variation of beam are also important.

The most common accelerator for HT are synchrotron and cyclotron or synchro-

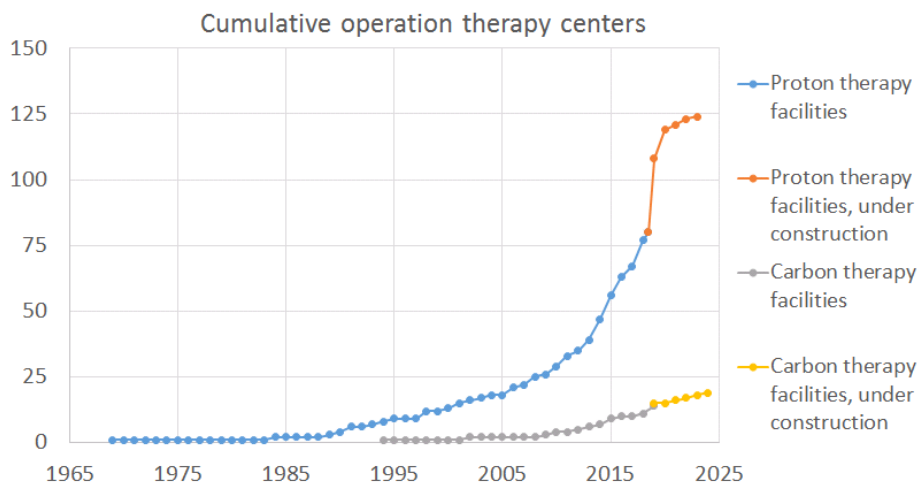


Figure 1.10: Cumulative number of HT centers as a function of time (last update: April 2019).

cyclotron. These two types of accelerators are a quite suitable acceleration technology however, they present several drawbacks and restricted abilities. The cyclotron provides proton therapy reliably and at low cost, but is mainly limited in the fixed beam extraction energy. It requires movable absorbers in the beam transport line and causes scattered particles creating a activation of the area since the beam intensity is reduced by several orders of magnitude [43]. Synchrotron are mainly used for carbon-ion therapy. The main drawback is the cost, the size, the complexity of the equipment and a low repetition rate resulting in long treatment time. All this has an impact on the limited number of patients that can be treated.

A new technology based on linac looks as one of the most promising option in HT on terms of size, cost, complexity and efficiency due to constant improvement of their technical performance and reliability. The main advantages of linacs lies in the possibility to actively change the output beam energy and reduce the treatment time due to high repetition frequency. These features are ideally suited for irradiation of moving organs with pencil beam scanning [44] and allow the access of a larger number of patients.

The first proposal to construct of a proton therapy centre based on linear accelerator was in 1991 [45]. This solution was taken up by TERA (Fondazione per Adroterapia Oncologica) Foundation, which in 1994–1995 designed a 230 MeV linac for proton therapy [46] and they designed, constructed and tested at 3 GHz AS for protons [47,48] in collaboration with CERN and INFN (Insituto Nazionale di Fisica Nucleare). The proof of principle of the use of a 3 GHz linac for acceleration of protons was achieved in 2002 with the LInac BOoster (LIBO) prototype. A 3 GHz Side-Coupled Linac (SCL) unit called LIBO with a design gradient of 15.7 MV/m has been the first prototype of a linac for proton therapy ever built and tested. The first unit of LIBO has accelerated protons from 62 to 74 MeV (see right-top picture in Fig 1.11).

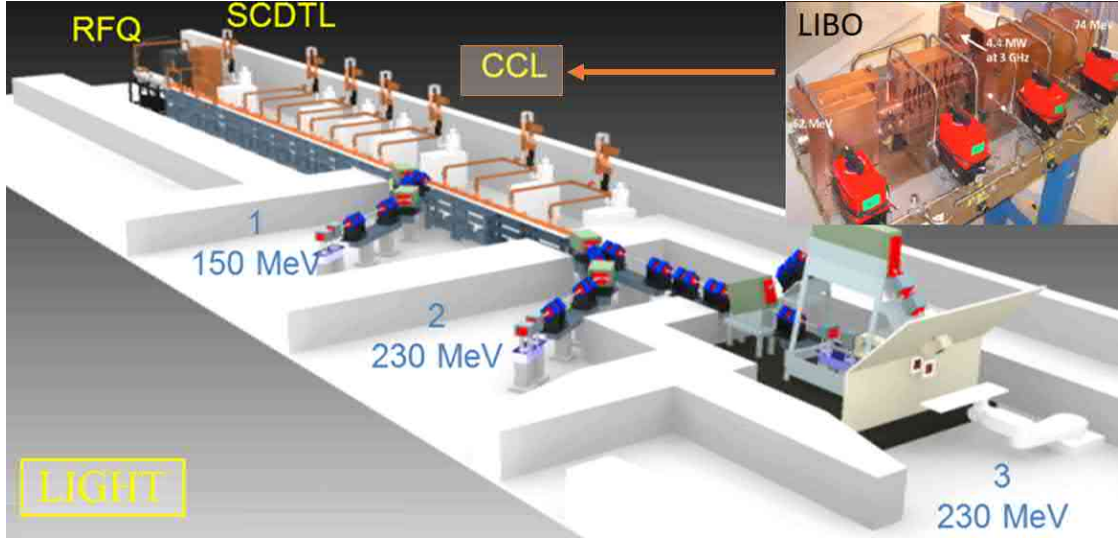


Figure 1.11: The all-linac design, proposed by A.D.A.M., for LIGHT.

Nowadays A.D.A.M (Application of Detectors and Accelerators to Medicine) [49], a spin-off company of CERN, is building a commercial all-linac machine for proton therapy [50], named LIGHT (Linac for Image Guided Hadron Therapy) [51] based on the TERA design of LIBO (Fig. 1.11). The LIGHT design is composed of three linear accelerating sections: an RFQ up to 5 MeV, an SCDTL (Side-Coupled Drift Tube Linac) up to 37.5 MeV and a CCL (Coupled Cavity Linac) up to 230 MeV. The RFQ is based on a novel design for 750 MHz, made by CERN [52–54]. This solution was specifically designed to inject particles from RFQ at 5 MeV into a 3 GHz DTL (Drift Tube Linac) structure as the one proposed by ENEA.

Based on the experience developed after the design and test of LIBO, TERA Foundation has recently proposed a design based on all-linac solution [55]. A sketch of the TULIP (Turning Linac for Protontherapy) all-linac solution studied is presented in Fig. 1.12. The principal goal of the project is to build 3 GHz AS mounted on a rotating gantry using a novel high-frequency RFQ (750 MHz) as injector. The RFQ output energy is matched into a 3 GHz low energy chain with energy up to 76 MeV and HG structures - up to 230 MeV. The design and fabrication of a HG prototype for medical proton linac has been funded by the Knowledge and Transfer (KT) group at CERN under the project 'High-gradient accelerating structures for proton therapy linacs' [56]. The first HG prototype of AS for  $\beta=0.38$  have been developed to achieve accelerating gradient about 50 MV/m for 76 MeV energy protons. The design principle of this structure is very similar to CLIC prototypes as both are operationally limited in terms of maximum surface electric field ( $\approx 250$  MV/m) and of maximum BDR ( $\approx 10^{-6}$  bpp/m). Thanks to the HG technology, TULIP's linac can be reduced to 6 m at a final energy of 230 MeV with a total weight of approximately 12 tons. This opens the possibility to install them on a rotation gantry. According to last design, 18 AS are designed at target gradient of 40 MV/m. The selected gradient is lower than

the designed limit (50 MV/m) to maintain a safety margin in terms of BDR. In addition, it gives a reduction in RF thermal load into the structure. The all-linac solution can reach 100 % transmission of a high quality beam at loss-free operation and the facility does not require any significant shielding. The high frequency RFQ is also reducing dimension and construction cost. Reducing the total length of the accelerators is very important since facilities need to be placed in hospital centers.

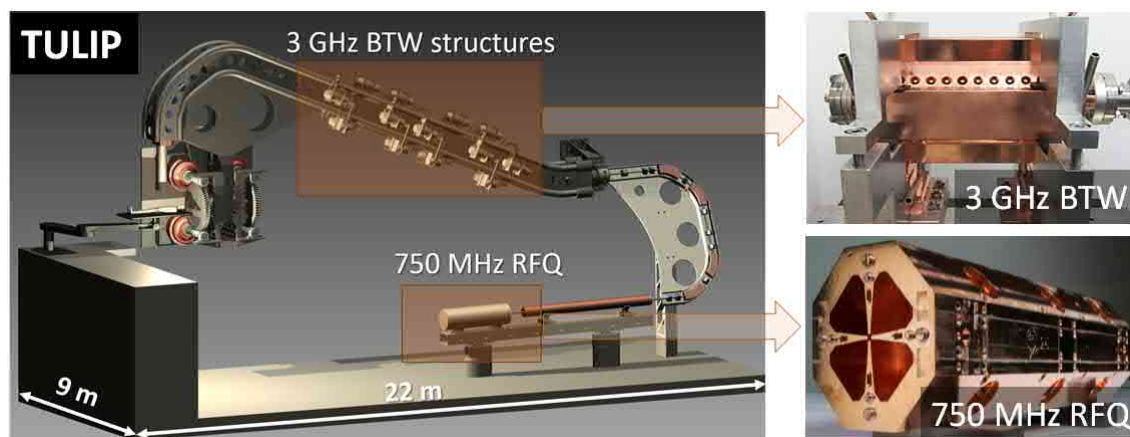


Figure 1.12: Sketch of TULIP all-linac solution and latest development components: 750 MHz RFQ and 3 GHz BTW. Courtesy of Mohammad Vaziri - TERA Foundation.

Moreover, the treatment requirements impose a limit on BD probability to  $7.7 \times 10^{-7}$  bpp/m in the all acceleration components to have less than one BD per a whole treatment session. In order to provide such conditions, a detailed study of BD at different stages of acceleration are required.

In this thesis we will focus in the study of BD phenomenon in two kinds of RF structures: a 3 GHz HG structure and 4-vane RFQs designed for applications in HT linacs. Concerning the 3 GHz AS, this study can serve as proof of principle of the use of a HG linac for HT. The cavity is designed for a gradient more than twice what has been reached in previously tested cavities at the same frequency. The main goal of this prototype is to explore the BD limits in S-band cavities. The feasibility of such a structure will open up many possibilities for using in different projects mainly due to the reduced size of the installation. The result of the high power tests of this structure will be presented in this thesis.

Concerning the RFQs, in order to provide input data for the design of future HG RFQs, measurements of the BD behaviour of two structures with different frequencies have been performed. One is a compact 750 MHz RFQ made in the framework of a program on medical applications, and the other is the RFQ for CERN's LINAC4. The results presented here will summarize the achieved performance and long-term behaviour of these structures, this is the first systematic study carried out of these promising devices.

## Chapter 2

# Breakdown studies of a S-band HG RF AS for hadron therapy applications

A novel S-band (2.9985 GHz) BTW AS for a medical proton linac, known as S-band BTW HT, has been designed, manufactured and tested at CERN [12,13]. Other version of such a concept has been studied in the past by the TERA foundation in collaboration with CLIC. The LIBO program was established and funded by the CERN KT to design, build and test this prototype HG AS.

The main goal of our studies is to confirm the efficiency of this S-band cavity and define the HG limits in terms of BDRs. This structure could be considered as one of the candidates of TULIP project as explained in Chapter 1. For the nominal operating parameters of the TULIP type of structure, the BDR is in the order of  $10^{-7}$  bpp/m, but this value is too low to provide significant statistics for assessing the potential of the structure. Therefore, the accelerating gradient dependence on the BD probability have been evaluated for higher fields. When the AS is operated at high BDR regime, the cavity surface is prone to damage. A control system and operation algorithm that keeps the BDR below a fixed value have been developed in order to stabilize the test and to increase the life span of the equipment. The results of this test will be used to refine and to determine a scaling law (Eq. (1.36)).

This chapter describes the low-power and high-power test setups, and presents a entire high power conditioning history, and discusses the main experimental results obtained from the analysis of BD behaviour. The data analysis includes the BD localization within the structure, the dark current, and the field emission study. Furthermore a comparative analysis of the conditioning histories for different prototypes was also performed. These measurements are not directly relevant to the HG performance of the structure, but it can be used to understand the BD phenomena, to explore the limitations of HG AS, and to assess the design of future HG RF structures. This includes the geometrical design of the structures, and also the RF processing schemes, the manufacturing techniques, as well as

the cleaning and the handling procedures.

## 2.1 The S-band BTW HT description and main features

The S-band BTW HT has been designed to operate with low  $\beta$  ( $\beta = 0.38$ ) protons reaching an accelerating gradient of 50 MV/m, with a corresponding maximum surface electric field of above 200 MV/m. This low value of  $\beta$  was chosen to achieve the maximum possible gradient. The S-band BTW HT uses the technology developed for CLIC with speed of light phase velocity but adapted to accelerate non-relativistic particles. The S-band TW of the AS is  $5\pi/6$  ( $150^\circ$ ) phase advance to maintain high RF efficiency and a low wakefield. The prototype has been designed to accelerate protons with an initial energy of 76 MeV. A general view of the S-band BTW HT and the regular cell is shown in Fig. 2.1. The structure consists of 12 equal length RF cells, whose aperture diameter is 5 mm. The total length of the prototype is 189.84 mm.

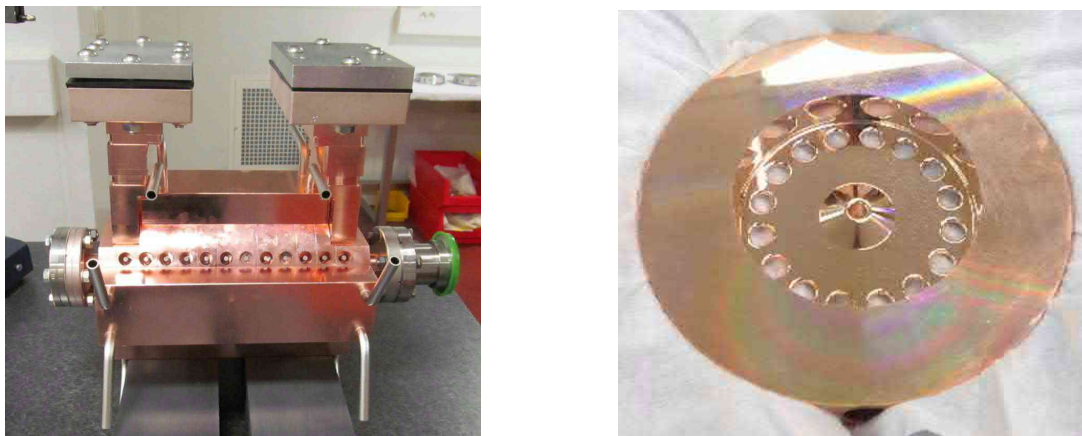


Figure 2.1: Picture of the S-band BTW HT prototype (left) and a regular cell (right).

The shape of the central part of the iris has been optimized to reduce the  $S_c$  and the RF power losses for a given gradient. The cell-to-cell coupling is made by 16 holes in the region of the highest magnetic field. This gives a magnetic coupling and results in a BTW that makes the accelerated particles to travel in the direction opposite to the power flow as shown in Fig.1.3. The number and size of the coupling holes has been optimized in order to provide the required coupling. Special shape of nose cones are added to amplify the electric field near the axis.

The S-band BTW HT is a CG with a group velocity ranging between 0.4 - 0.2 % of  $c$ . The range has been chosen as a compromise between acceptable filling time and efficient acceleration of the beam. The tapering in group velocity is made by linearly varying the radii of the coupling holes and the cell diameter. The input RF power coupler was optimized to provide impedance matching, and the radius of the coupling holes has been reduced in the region near the coupling slot (see Fig. 2.2) due to the local increase of the power flow. All the other geometrical parameters have been kept constant throughout the



Figure 2.2: Input coupler design (left) and single mechanical cell (right) of the S-band BTW HT.

structure. The most important parameters of the S-band BTW HT are summarized in Table 2.1 and a complete description can be found in [12].

Table 2.1: Main parameters of the S-band BTW HT.

Parameter	Value	Units
Phase advance ( $\Delta\phi$ )	$5\pi/6$	rad
Wall thickness	2	mm
Gap	7	mm
Nose cone angle	25	deg
Number of cells	12	
Structure length	189.9	mm
Quality factor (1st/last cell)	6954 / 7415	
Normalized $r_s$ (1st/last cell)	51.5 / 54.6	M $\Omega$ /m
Filling time ( $t_{fill}$ )	224	ns
Group velocity $v_g$ (1st/last cell)	0.39/0.21	%c
Average accelerating gradient ( $E_{acc}$ )	50	MV/m
Peak incident power ( $P_{in}$ )	20.6	MW
Max $S_c / E_{acc}^2$	$3.1 \cdot 10^{-4}$	A/V
Max $E_{acc}$ (for BDR of $10^{-6}$ bpp/m)	74.9	MV/m
Max $E_s$	219	MV/m

## 2.2 Low-power analysis of the S-band BTW HT

The S-band BTW HT followed a fabrication process established for CLIC X-band prototypes including high-precision diamond machined pieces cleaned with light etching, diffusion bonded under hydrogen atmosphere with a maximum temperature of the heat cycle of 1050 °C. The S-band BTW HT structure has been tuned via bead-pull measurements [57]

to minimise the SW pattern and to provide the desired phase advance ( $150 \pm 1.5^\circ$  for regular cells) at the operating frequency of 2.9985 GHz under vacuum at a temperature of 32 °C [58]. The measurements have been made in the laboratory at 23 °C with dry nitrogen atmosphere. The low-power measurements were carried out by the CERN RF group in the clean room for LLRF measurements.

The profile of the longitudinal electric field together with the RF phase advance per cell and the S11 parameters in the complex plane after the bead-pulling technique with reflection coefficients are shown in Fig. 2.3. The scattering parameters measured before the high-power test were  $S_{11} = -24.3$  dB,  $S_{22} = -60.2$  dB, where port 1 is the input RF port and port 2 is the output RF ports.

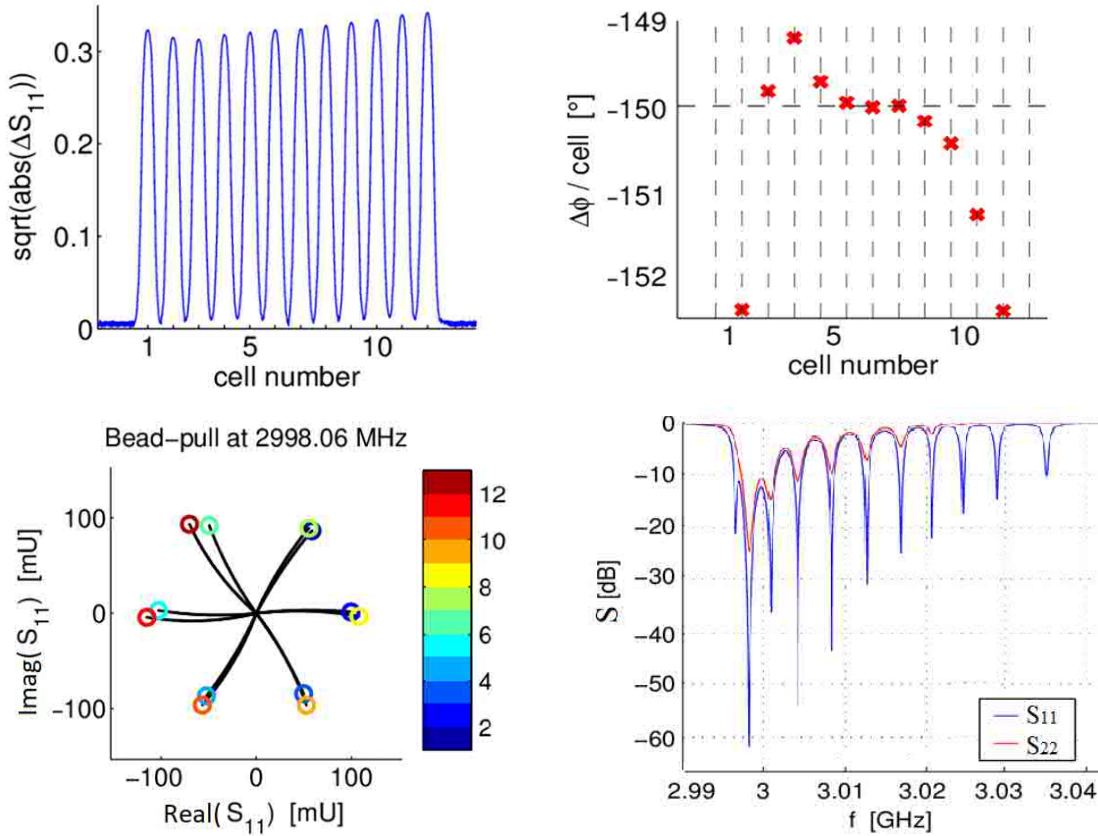


Figure 2.3: The electric field pattern in magnitude and phase (top) and S-parameters (bottom) along the structure in a dry nitrogen atmosphere at 23 °C.

### 2.3 Sbox high-power set-up description and update

The high-power test of the S-band BTW HT was performed at the S-band test facility (Sbox), located in the klystron gallery of CTF3 [59] at CERN. The AS was installed in

the bunker where X-band test facility is also placed [60], as shown in Fig. 2.4 (top).

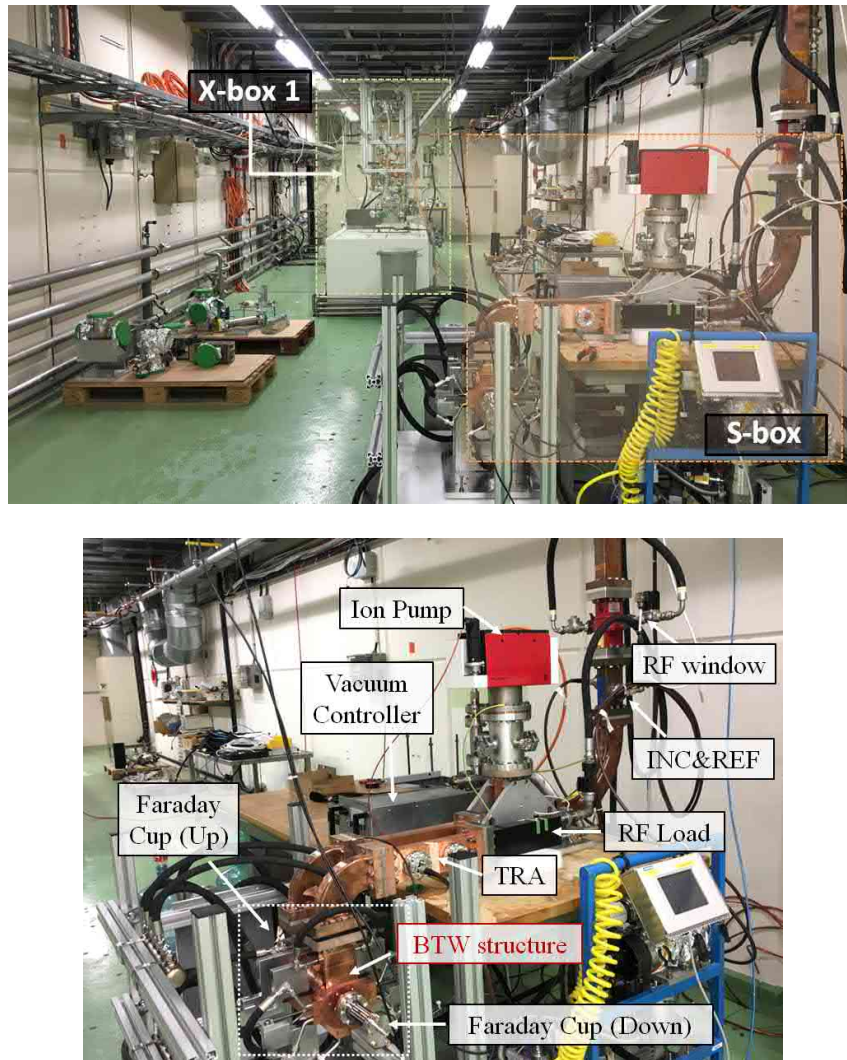


Figure 2.4: Bunker of CTF3 where Sbox is located (top). Zoom of the structure and subsystems in the S-box test area at CERN (bottom).

Before December 2017, the High Power RF (HPRF) test setup [61] was based on a 43 MW S-band klystron MKS14 [62], delivering RF pulses with a maximum length of  $5 \mu\text{s}$  at a repetition rate of 25 Hz. The klystron RF input is driven from a preamplifier stage consisting on a 400 W Solid-State Amplifier (SSA) with a gain of 56 dB, model AM10-3S-55-55R from Microwave Amplifiers. The input for this amplifier is a  $5 \mu\text{s}$  length pulsed RF signal of 2.9985 GHz coming from the Low Level RF (LLRF) system.

The power is sent through WR-284 waveguides to the Device Under Test (DUT). The high power network consists on two directional couplers, two pumping ports with one

pump attached, and a RF load at the output to terminate the waveguide network. A schematic of the high-power components of the test facility is shown in Fig. 2.5. The green arrow shows the signals sent to the control system for RF generation and the blue arrows - the signals from DUT measured for BD identification.

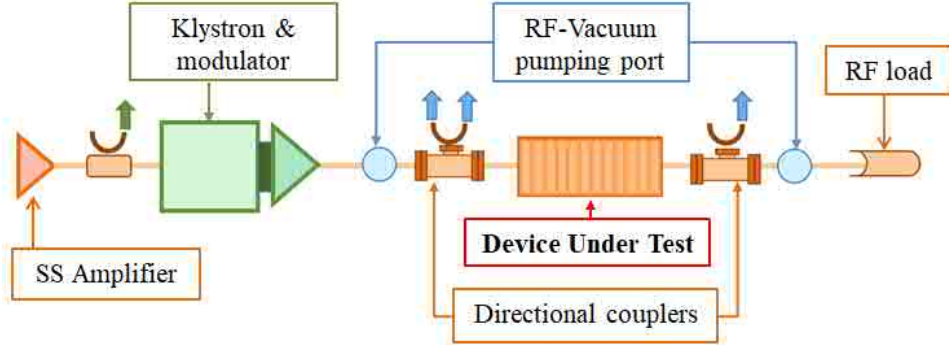


Figure 2.5: Schematic layout of the S-box high power test setup.

Two directional couplers, placed at the input and output of the DUT, are used to measure and calibrate the incident (INC), reflected (REF) and transmitted (TRA) RF power signals. Faraday Cups (FC) are placed in the upstream (Up) and downstream (Down) directions along the structure’s beam axis to measure dark current and detect BD events. The DUT is connected to an ion pump and dedicated chiller unit to adjust the cooling water temperature at 32 °C. The load and RF window are connected to the main CTF3 cooling circuit at the appropriate water flow during these runs. The ion pump is installed next to the DUT through an RF pumping port to keep Ultra-High Vacuum (UHV) below  $10^{-8}$  mbar in the DUT. A detailed view of this experimental setup is shown in bottom part of Fig. 2.4.

The RF network consists of 76 meters of waveguide. The power attenuation in S-Band (WR-284) waveguides is around 0.02 dB/m that cause large total power losses. Most of the RF line from the klystron to the cavity was under SF6 (Sulfur Hexafluoride), in order to prevent RF breakdown by resisting ionization. An RF window separated the SF6 atmosphere from the part of RF system where the DUT and subsystem were located under UHV. The klystron was protected against reflected power by a high RF power circulator.

The control and acquisition system are based on National Instruments (NI) electronics [63]. A PXI real-time system performs the acquisition of RF signals, and also control of vacuum, temperature and water cooling signals. The PXI RF generator provide the amplitude and phase modulated RF pulse to drive the preamplifier which drives the klystron. The TRA and REF RF signals are diagnosed in several stages to optimize the pulse modulation, and to protect the system from an unexpected rise of REF signals.

The detection of the BD events in the S-band BTW HT is made possible by using the acquired signals and the final data are stored. The operation of the test stand is controlled and interfaced by a simplified version of the Xbox-2 LabVIEW software [64], which allows the user to control the RF power level, to modulate the phase waveform, and

to automatize the conditioning of the structure [65]. The RF signals from the directional couplers are digitized in a NI-5761 ADC installed on the PXI crate, and they are used as feedback of the power operation of the system. The amplitude and the phase of these 3 GHz signals are down-mixed to 62.5 MHz and digitized in 250 Msps analog-to-digital converter (ADCs), having sample rate of 1.6 sample/s with a 12 bit resolution.

The data analysis is based on amplitude and phase of three RF power signals (INC, REF, TRA) and two FC currents signals. The data collected by the acquisition system is analysed offline. The control system of the klystron-modulator unit receives the triggering signals from the PXI. Data are collected and processed by the PXI controller for every pulse, and interlocks the system upon detection of setted values of RF REF and FC signals, which would be an indication of BD. The RF power turned off after every BD or vacuum spike during the test and then ramp up again. All signals of each BD event and the two previous normal pulses are stored in a TDMS-format file per day in the hard disk of the PXI. Regular pulses are also stored every minute when BD has not occurred. In addition, the history of vacuum levels of the network, the delivered power to the DUT, and the pulse length are averaged and logged every second. The INC, REF and TRA power signals have been recalibrated, and the fitted parameters have been used in the LabVIEW code to relate the mV signals read by the PXI crate into MW RF power. Additional regular calibrations were done regularly during the high-power test.

Initially, the launch and adjustment of the klystron and the modulator are carried out manually. After that, the settings are transferred to a remote control. The triggers are generated by an FPGA contained in the PXI crate. The FPGA is used to ensure that the hardware continue runs in case of a software crash on the real-time system. The interlock and trigger systems runs on the same FPGA, allowing the system to be interlocked by stopping the triggers that are sent to the klystron/modulator or the PXI's RF vector generator card. The PXI controller includes the interlocks on the flow-meters of the cooling water of the structure and the load, the pressure-meter, and the temperature-meter attached to the load. There are also independent interlocks of the bunker related to the safety chain of CTF3 facility. The bunker zone is controlled by radiation monitors including an alarm system.

In order to improve the performance of the setup, an upgrade has been made in December 2017. The LLRF and HPRF have been changed, the waveguide length has been reduced, and a new klystron, a modulator and a control system have been installed. The RF deflector has been moved to a new system. The stable operation of a new modulator provides the ability to conduct testing at higher power and long pulse length. The new 43 MW S-band klystron MKS07 is used to delivers RF pulses up to 5  $\mu$ s with a repetition rate of 50 Hz. This high frequency system serves to reduce the time required to condition and test of the AS. The HPRF of Sbox before and after update are presented on Fig. 2.6. A schematic description of the LLRF and HPRF components, the instrumentation for BD diagnostic and upgraded acquisition subsystems of Sbox, with the associated LLRF signals, are sketched in Fig. 2.7.

The upgraded klystron-modulator is no longer compatible with the CLEAR control systems and has its own interlocking system. The SSA is controlled directly from the

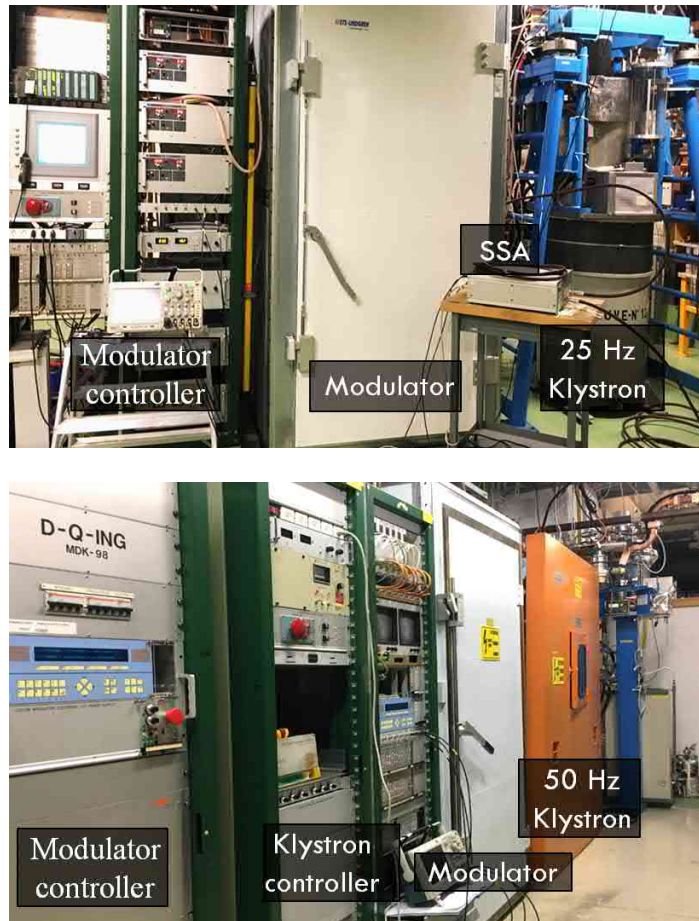


Figure 2.6: Picture of the HPRF of the S-band test stand before (top) and after (bottom) upgrade: klystron, modulator and control system.

LLRF output of the PXI. The system was designed such that the interlock signal can be reset manually or automatically by the control system, but the modulator cannot be restarted remotely.

The timing signals now come directly from the PXI via a pulse repeater which acts as a Transistor-Transistor Logic (TTL) to a Blocking Conversion system (BLO) [66] converter. All of the timings are set up such that the start of RF power (SRFP), the end of RF power (ERFP) and the LLRF signals arrive at the correct time. Timing of the klystron pulse from the modulator (SKLY) is adjusted from a LabVIEW GUI. The cables that carry the signal to the LLRF racks are attached directly to the high power coupler. At the LLRF rack, the signals are attenuated and sent into the instrumentation. A schematic view of the DAQ that connects the PXI and the klystron is shown in Fig. 2.8. The electronic devices responsible for RF generation were assembled to one rack located next to HPRF (see Fig. 2.9).

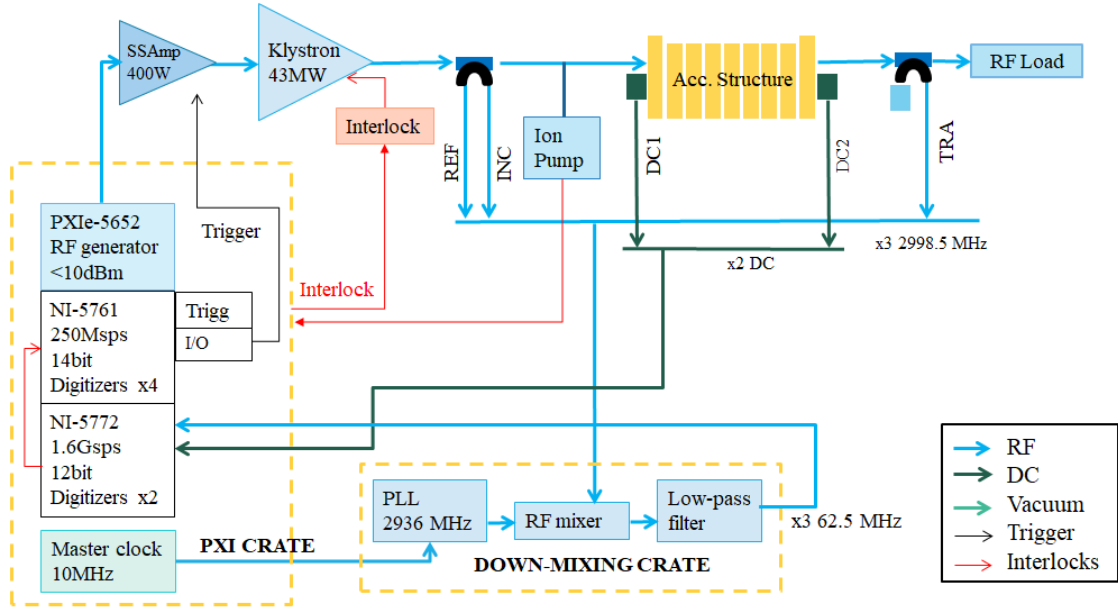


Figure 2.7: Schematic layout with the main components of the high power test set-up after upgrade in December 2017.

The diagnostic set-up and the BD identification procedure were kept unchanged. Only the ability to measure the surface temperature of the structure was added. This temperature measurement becomes important when the AS is operated at high power which exceeded the value set by design. The temperature of the AS is acquired with Resistance Temperature Detectors (RTD) attached to the outer copper wall of the cavity, and the detected signals are recorded and visualised via the LabVIEW's user interface.

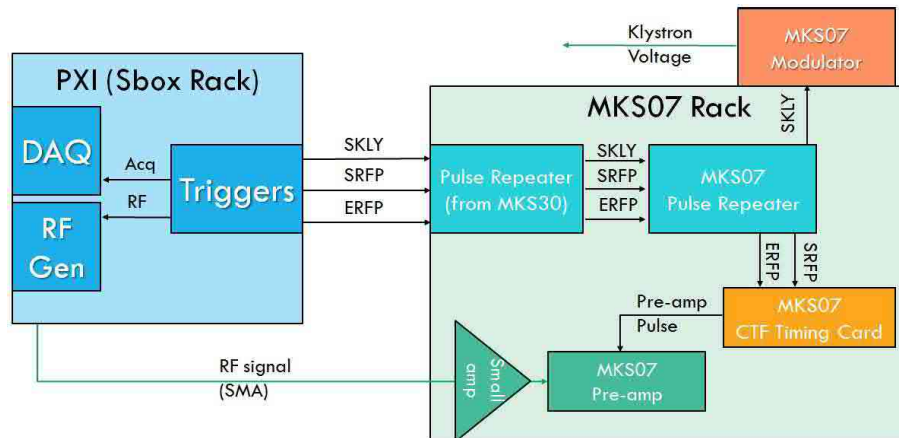


Figure 2.8: Details of the acquisition subsystems of the Sbox test facility: connection between the PXI and the klystron

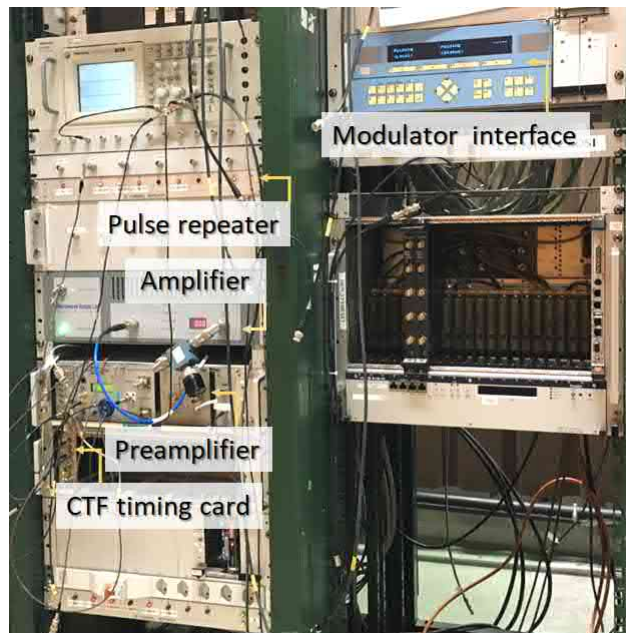


Figure 2.9: RF generation stand as part of the LLRF of the Sbox after December 2017.

Due to insufficient computing resources in the existing code and for further requirements, the software has been also rewritten following a simplified version of the Xbox-3 LabVIEW [64, 67]. The software sets up the sample rate, the input voltage range, the offset, the trigger delay, and records the length of the RF input power. A buffer has been set up to visualize the current and the previous pulse, in case of an interlock. The timestamps have been replaced by a pulse counter to calculate the BDR. This will give us the opportunity to perform more accurate conditioning algorithm in terms of number of pulses. The vacuum feedback algorithm has been also added as additional conditioning strategies. The settings concerning the phase of the pulse have been included to the DAQ: the time at which the phase flip occurs, its magnitude and its shape. A phase correction can be applied across the whole pulse in order to correct errors introduced by the modulator's voltage droop. The automatic phase flattening algorithm is enabled by default. The system was successfully tested in operation, but the final replacement of the software did not occur after to the completion of the conditioning of the S-band BTW HT. Some additional software information can be found in Appendix A. The software can be used for subsequent testing of the AS as well as other RF components.

In summary, this updated version of the test bench gave us the opportunity to complete the test without power limitation and with a double repetition rate.

## 2.4 High-power conditioning and analysis of results

The HG RF structure test program has been conducted to understand the physical processes associated with RF BDs, and to determine the mechanisms limiting the gradient

and causing structure damage. In order to reach the targeted low BDR, the conditioning process with a series of RF pulses, increasing the power gradually is required. In addition, the production and assembly techniques of the cavities needs constant improvement. The performance of the AS is highly dependent on the fabrication technology and on the quality control.

The high-power tests of the S-band BTW HT have been carried out at the S-band test facility from December 2016 to May 2018. The structure was conditioned to high gradient using the same protocol as for CLIC 12 GHz structures [68]. However after the RF high power test, it was found that the structure was installed backwards – which means that the power was fed into the low group velocity region end and, it was consequently far from CG. Therefore the field distribution was no longer uniform and the maximum field have been found in the first cell and decreases gradually towards the end as shown in Fig. 2.10.

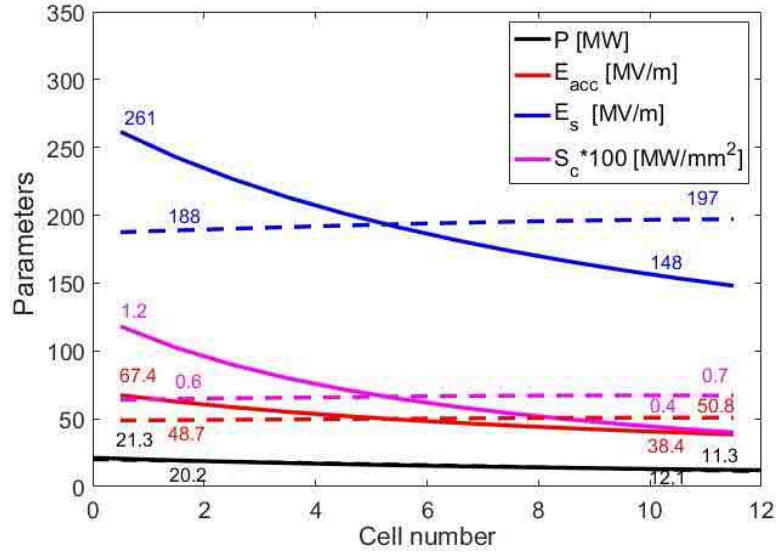


Figure 2.10: Distribution of the RF parameters along the structure cells for normal (dashed lines) and backward (solid lines) filled at average unloaded gradient of 50 MV/m (red: accelerating gradient; blue: maximum surface electric field; magenta: maximum modified Poynting vector).

### 2.4.1 Conditioning of the S-band BTW HT accelerating structure

After fabrication, an RF AS is not capable of sustaining the design gradient, in order to achieve the full performance, a process known as conditioning is needed. This process requires a long time of operation to bring the structure to operational parameters. The conditioning algorithm [68] developed for CLIC X-band AS in the Xboxes [69,70] was used for the S-band BTW HT.

This conditioning is carried out by increasing the input power level in a controlled

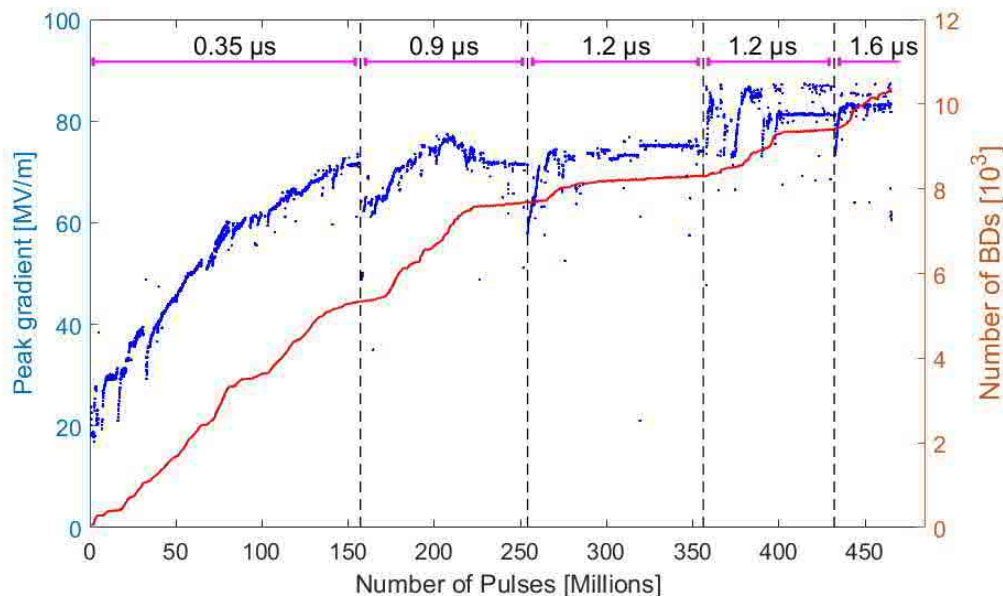


Figure 2.11: Conditioning history of the BTW prototype tested at CERN S-box. The plot represents the accelerating gradient (blue) and breakdown number (red) versus the number of pulses, at different pulse lengths indicated on top.

manner with a limit level of BDR at  $3 \times 10^{-5}$  BDs per pulse and with a vacuum level below an acceptable threshold, typically  $1 \times 10^{-7}$  mbar. A small initial pulse length of  $0.35 \mu\text{s}$  with rise time of  $0.075 \mu\text{s}$  was used to avoid damaging the structure. The structure has reached above  $70 \text{ MV/m}$  after 150 million pulses of  $0.35 \mu\text{s}$ . Then, the accelerating gradient was reduced about 15%, the pulse length was incremented  $0.3 \mu\text{s}$  with rise time equal to the filling time ( $t_{fill} = 0.224 \mu\text{s}$ ) of the structure. When the gradient exceeded above  $70 \text{ MV/m}$ , the process was repeated with a longer pulse. In the same way the pulse length was progressively increased up to  $1.6 \mu\text{s}$ . The vacuum level in normal operation was  $2.6 \times 10^{-8}$  mbar. Since the waveguide components were tested before, the conditioning was focused on the activity of the structure. A strong vacuum activity was observed at the beginning of testing due to surface contamination by oxide layers. The RF conditioning of an AS involves processing with large number of RF pulses over a long period of time. The Fig. 2.11 represents the accelerating gradient and the cumulative number of BDs with respect to the number of triggered pulses, at the different pulse lengths indicated on top. The structure is fully conditioned when the value of the BDR is stable and consistent with the requirements. For the case of the S-band BTW HT, it took about 450 million RF pulses and one thousand BDs. The AS was tested at RF power from zero to up 33 MW and achieved a peak gradient of  $83 \text{ MV/m}$  in the first cell with  $1.6 \mu\text{s}$  pulse length, and a BDR of  $3 \times 10^{-5}$  bpp/m at the end of the test.

The performance of an AS is evaluated by the BDR. This parameter changes over

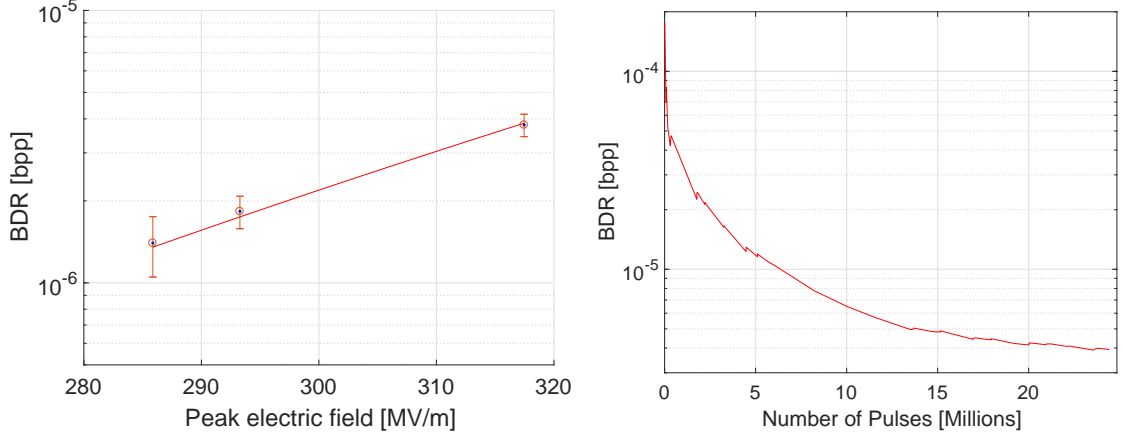


Figure 2.12: Measurements of BDR dependence with the peak surface electric field during conditioning at  $1.2 \mu\text{s}$  pulse length performed for the S-band BTW HT. The data are fitted by the next expression:  $BDR \propto E_{acc}^{10}$  (left). BDR with respect to the accumulated number of pulses during conditioning with constant power 31 MW (accelerating gradient is around 81 MV/m) and  $1.2 \mu\text{s}$  pulse length (right).

time and have a strong dependence on the accelerating gradient and the pulse length. After the structure was sufficiently conditioned and reached the designed gradient, the BDR measurements have been performed at different power level at fixed pulse length. The reduction of the BDR for a certain field level indicates the conditioning status of the cavity. To measure the BDR, the total number of BD events has been counted for a given number of pulses. The measured scaling law for S-band BTW HT at different gradients (peak surface electric field) is given by  $BDR \propto E^{10}$  as represented in Fig. 2.12 (left). This law is quite different from the empirical scaling law determined for other HG prototypes at 12 and 30 GHz which is  $BDR \propto E^{30}$ . This can be an evidence a frequency independence of the data. The error bars of the BDR in Fig.2.12 (right) represents the statistical error. The relative error bar of the low BDR points is high because a small number of BD events occur at low-power. Error tolerance estimation is considered within a reasonable testing time at the available repetition rate. A constant power running is also very important to define long term evolution. The experiments need to be performed with higher statistics in order to evaluate the effect of BDs on the operation of the HG structure. Typically, the AS keep conditioning during all the processing time.

As shown in the right part of Fig. 2.12, the BDR decay reduced to  $4 \times 10^{-6}$  bpp, measured for a peak power corresponding to 81 MV/m close to the limiting value. This value can be used as specification parameter of the AS for certain initial conditions. The maximum modified Poynting vector was about  $1.155 \text{ MW/mm}^2$ . A significant improvement in the performance is observed during the test. The BDR is one of the main indicators of the performance of the AS since the BDs have an impact on the beam stability during a treatment session.

### 2.4.2 RF breakdown localization

The RF design of an AS is targeting at a uniform distribution of BDs in all the cells. A ‘hot cell’ or high BDR in one cell would limit the conditioning and performance of the whole structure.

The main diagnostic signals used for BD detections in TW AS are the amplitude and the phase of RF power signals (INC, TRA and REF), and the dark current measurements. The BD acts as a short circuit, which causes a rapid increase in the REF and a loss in the TRA signals and this is accompanied by an electron emission detected by the Up and Down FCs. When a BD occurs, the value of the dark current signals raises and saturates the ADCs. The total current generated by the BD will be higher since only a small fraction solid angle of the current can be captured by the FC. The shape of these signals before and during a BD are shown in Fig. 2.13. The dark current signal is inverted in the plot for illustration purposes. Initial negative sign of the plot indicates that the collected charge carrying particles are electrons.

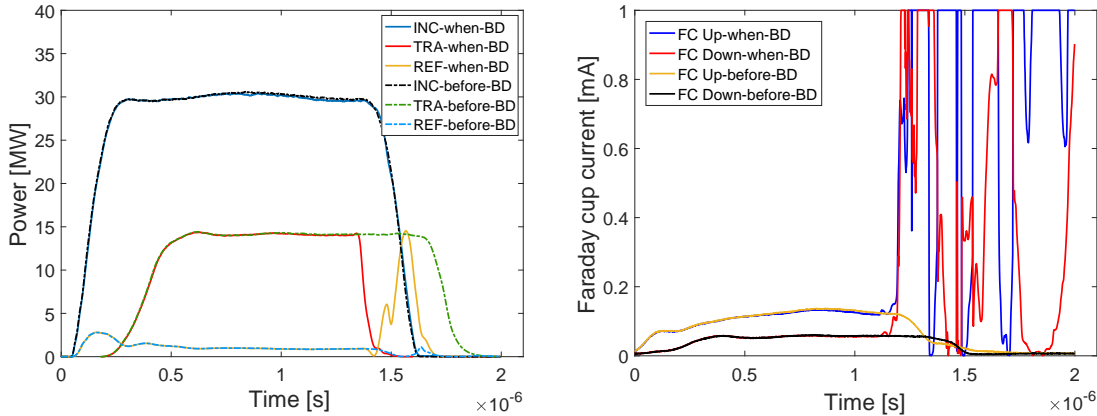


Figure 2.13: Typical INC, TRA and REF (left) and dark current (right) signals on a pulse before (dashed lines) and during (solid lines) BD collected from the S-band BTW HT tested at Sbox.

Three methods have been used for determining the spatial distribution of the BDs along the multiple cells of the AS, known as ‘edge’, ‘BD phase’ and ‘dark current’ methods. The BD distributions have been analysed during whole test time to understand the limiting factors of the design and avoid damage to the AS.

#### Edge method

The edge method is based on the timing difference of the falling edge of the TRA ( $t_{TRA}$ ) and the rising edge of the REF ( $t_{REF}$ ) signals [70]. The method consists of determining this timing difference and compare the time the wave needs to travel from the BD position to the input and output couplers, assuming that the change in TRA and REF power occurs simultaneously. This time difference can be defined as:

$$t_d^{edge} = t_{REF} - t_{TRA} + t_{fill} \quad (2.1)$$

The measurements range between 0 and twice the filling time if the breakdown is triggered inside the structure. From the group velocity profile, which is set from the design parameters of the AS, it is possible to translate the time difference information into a measure of the length travelled by the RF wave and to the cell location. The group velocity of the first and the last cells of the S-band BTW HT correspond to 0.39/0.21 %*c*. It should be also taken into account that the AS was installed in the backward direction. Fig. 2.14 displays the BD distribution for the entire run of the AS, translated into a cell number and normalized to the total number of BDs.

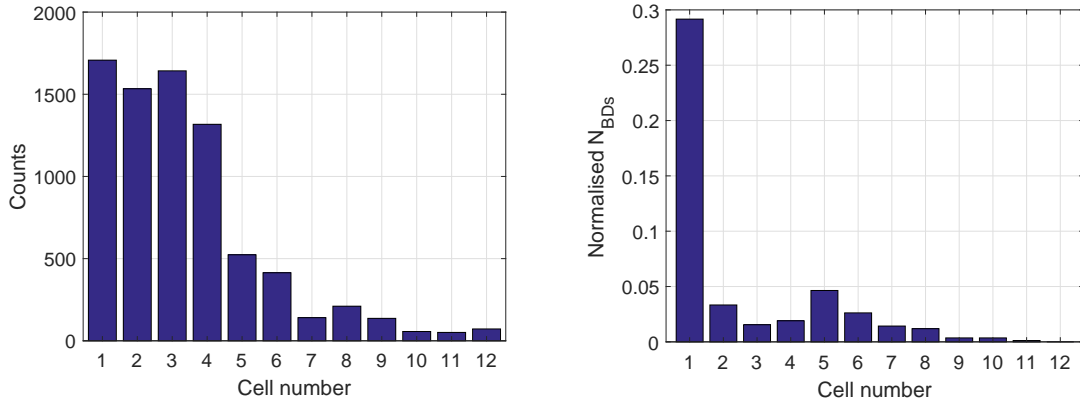


Figure 2.14: BDs localization in the S-band BTW HT determined via the edge method for the entire run (left) and the last months of the test (right).

According to the result calculated via this method, BDs occurred predominantly towards the input of the AS. The right part of Fig. 2.14 shows that the BDs are mainly in the first cell at the end of run. This could be explained by the fact that the highest surface field quantities occur in the first part of the structure due to the single-feed geometry of the input coupler and its detuning.

### Phase method

Another method has been used to increase the resolution of the BD localization. This method is based on comparing the measured phase of the REF and INC signals [70, 71], assuming that the reflection is always produced from the same place in the cell and BD phases are spaced 150° in case of the S-band BTW HT. The resulting signal represents the phase shift between the measured phase of the incident signal and the phase of the delayed reflection, when the BD is triggered:

$$\phi_{BD} = \phi_{REF}(t + t_d) - \phi_{INC}(t) \quad (2.2)$$

The resulting phase distribution is represented in the left part of Fig. 2.15. The measured phases are wrapped into the interval between 0 - 360°, and distributed around six peaks at about 150° of distance which corresponds to the phase advance between the cells of the structure. The six populations are clearly separated, that confirms the high resolution of the BD phase method. The right part of Fig. 2.15 demonstrates the interconnection between the timing and the phase methods. The time difference can be recalculated into cell numbers as in the edge method. The location of the BDs in phase does not look completely uniform due to the time resolution constraints of the LLRF detection system. This method shows that the BD distribution in the structure is similar to the edge method.

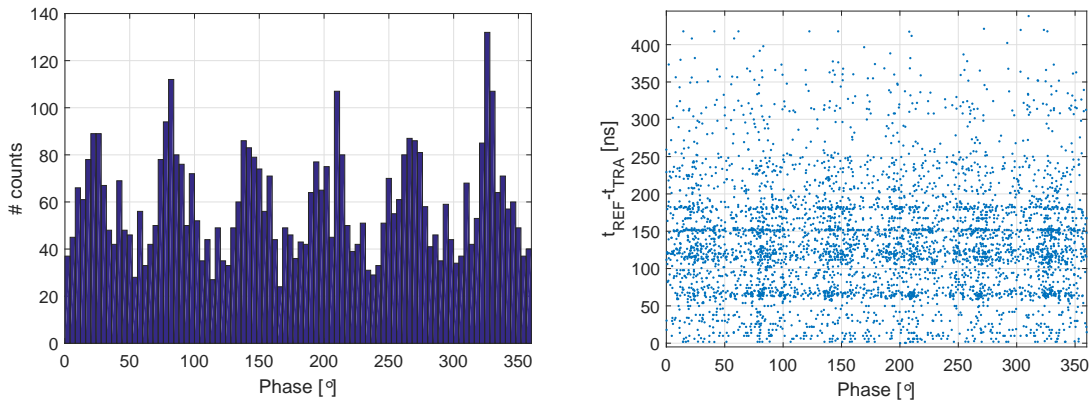


Figure 2.15: Distribution of breakdown phase measurements along the structure (right) and accumulative number (left) obtained from BD recorded during the test of the S-band BTW HT with the phase method.

### Faraday cup method

The Faraday-cup method uses the signal from the FC situated upstream from the cavity versus the falling edge of the TRA signal. When a BD occurs, a big spike in the FC signals is observed, as shown in Fig. 2.13. The design of the S-band BTW HT structure is quite specific, because the beam acceleration occurs opposite to the direction of the electric field. For this reason, the upstream dark current is significantly higher than the downstream current. These FC signals are saturated and give inaccurate timing to determine the BD location. It is also important to note that the FC signal has a sample rate that is different from the TRA signal. In order to use both signals together, the FC signal was interpolated so that the distance between each point is the same as for the TRA signal.

Fig. 2.16 shows the BD distribution along the AS based on FC method. The distribution is different compared to the edge and phase methods. The reason of these differences could be an alignment problem and variable waveform at low energy. The FC method is more suitable for determining the BD location for RF signals with a long pulse length relative to the rise time and a high dark current output, but FC method is not suitable for

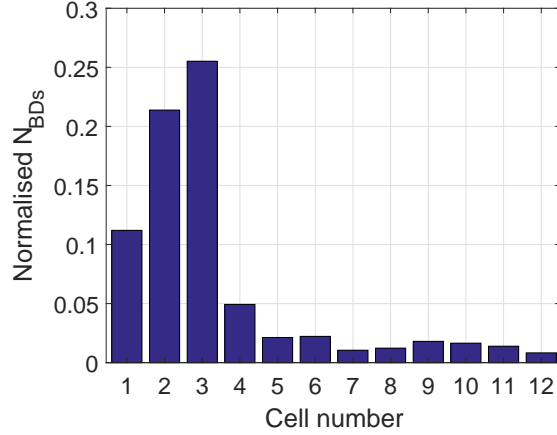


Figure 2.16: BDs localization in the S-band BTW TH with the FC method.

this type of AS since there are two zone with a high probability of BD location (noses and holes). The BD in the holes causes a minimum value of the dark current that complicates the measurement. Therefore FC signals are used for BD identification together with other RF signals.

To determine the state of the structure, the BD caused by antecedent BDs in the waveguide have been excluded. The appearance of such BDs was dominant in the last stage of testing due to problems with the circulator. The vacuum discharge in the waveguide not only distorts current signal but also affects the subsequent input pulses entering the cavity. An example of a BD in the structure caused by INC signal distortion is presented in Fig. 2.17. In this case, the dark current increases slightly, since only part of the input

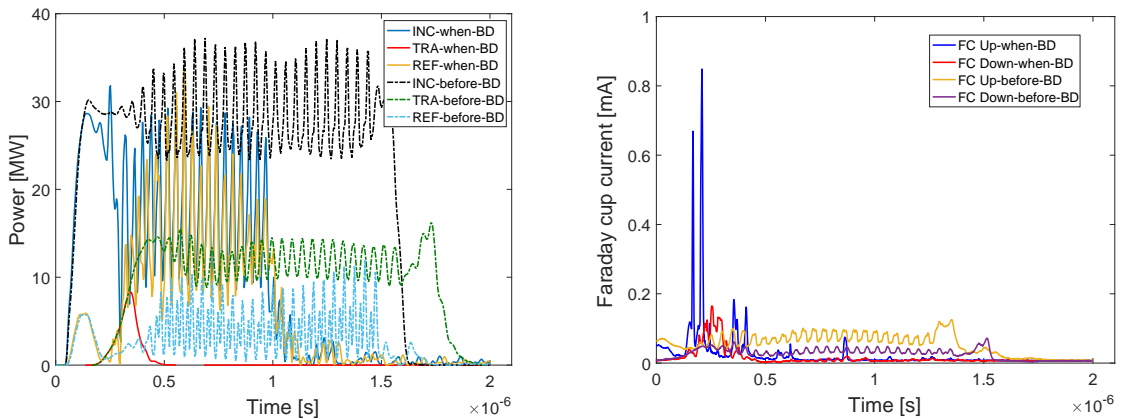


Figure 2.17: RF signals (left) and dark current signals (right) on a pulse during which a BD occurred due to BD in the waveguide. The dashed lines show the previous pulse signals.

signal is included in the structure. The frequency and location of all BDs are controlled, since this can lead to the destruction of the AS.

According to these results of the BD localization using these three methods, there are no evidence of a ‘hot spot’. The BD scattered throughout the AS, and the main number of the BD is located at the RF input region. Further increase in RF power was stopped to avoid irreversible processes in the structure and due to the circulator issues. The S-band BTW HT was tested with RF power going into the nominal output, which has lower group velocity than the nominal input. It explains the non-linear distribution of BD along the structure.

### 2.4.3 Investigation of limiting values of modified Poynting vector

$S_c$  is an important constraint for HG AS design that has been used for example to successfully increase the gradient in successive generations of CLIC X-band AS designs.  $S_c$  is a measure of the local power flow [32]. In the AS tested so far, the maximum value of  $S_c$  occurs in a region of high electric field, and tests have resulted in consistent limiting values [72, 73]. However, in this particular structure,  $S_c$  is maximum both on the noses, where the electric field is high, and on the coupling holes, where the magnetic field is also high, as shown in Fig. 1.8. An important question for further design optimization and also for the deep understanding of BD process, is if BDs are equally likely to occur, for the same  $S_c$ , on the coupling irises where the fields are primarily magnetic or on the noses where the fields are primarily electric. Consequently the possibility of distinguishing nose versus coupling hole BDs have been investigated.

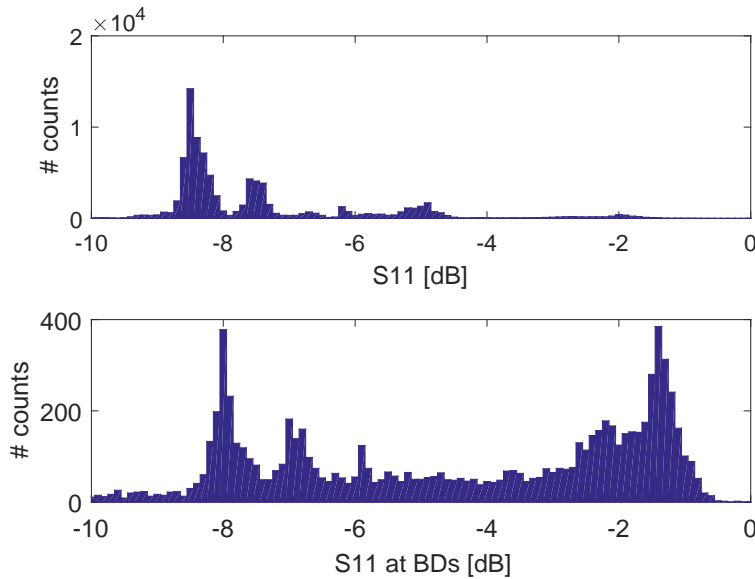


Figure 2.18:  $S_{11}$  histograms during normal pulses (top) and BD events (bottom).

In fact, the  $S_{11}$  signals during BDs show that there are two distinct populations of BDs: with a large reflection coefficient and with a relatively small one. This can be seen in Fig. 2.18. The observation of this twin-peaked distribution led to further investigation of the origin of this phenomenon. A possible hypothesis could be that BDs on the nose should cause a strong cell detuning, resulting in a large reflection coefficient, while BDs on one of the 16 coupling holes result in a small change in the coupling, and consequently a relatively small reflection coefficient.

HFSS simulations performed on the geometry models of 3D cavity [58] highlighted that the reflection difference between the BD simulated on the noses and on the coupling holes. In particular, the  $S_{11}$  is much higher when the BD happens on a RF gap, rather than on coupling holes. According to the simulated data, the reflection on the noses is in the range from 0 to -5 dB, and on the coupling holes is from -6 to -15 dB.

Taking a reflection coefficient of -6 dB as the cut-off value for separating the two BD populations, approximately the same number of BDs occurred on the nose and on the coupling holes during low power conditioning. This can be seen in Fig. 2.19 up to approximately 150 million pulses. At high power operation, the distribution shifted towards BDs occurring primarily on the noses.

The determination of the BDs location can be performed in a post-mortem analysis. However, this analysis has been postponed following the discovery that the structure had been operated backwards. The structure will be tested again, but in the correct direction, and afterwards cut open and the surface analysed.

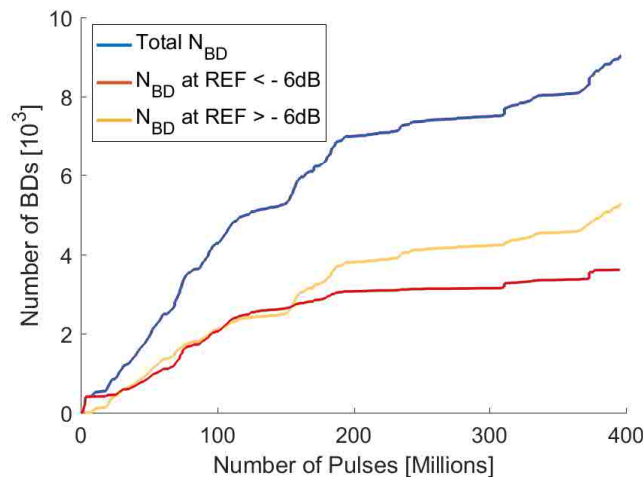


Figure 2.19: Number of BDs with reflection coefficient during the conditioning of the S-band BTW HT.

#### 2.4.4 Dark current analysis

Another important phenomenon which occurs in an AS operating at a HG is the electron field emission and the resulting dark current. It can cause RF energy absorption,

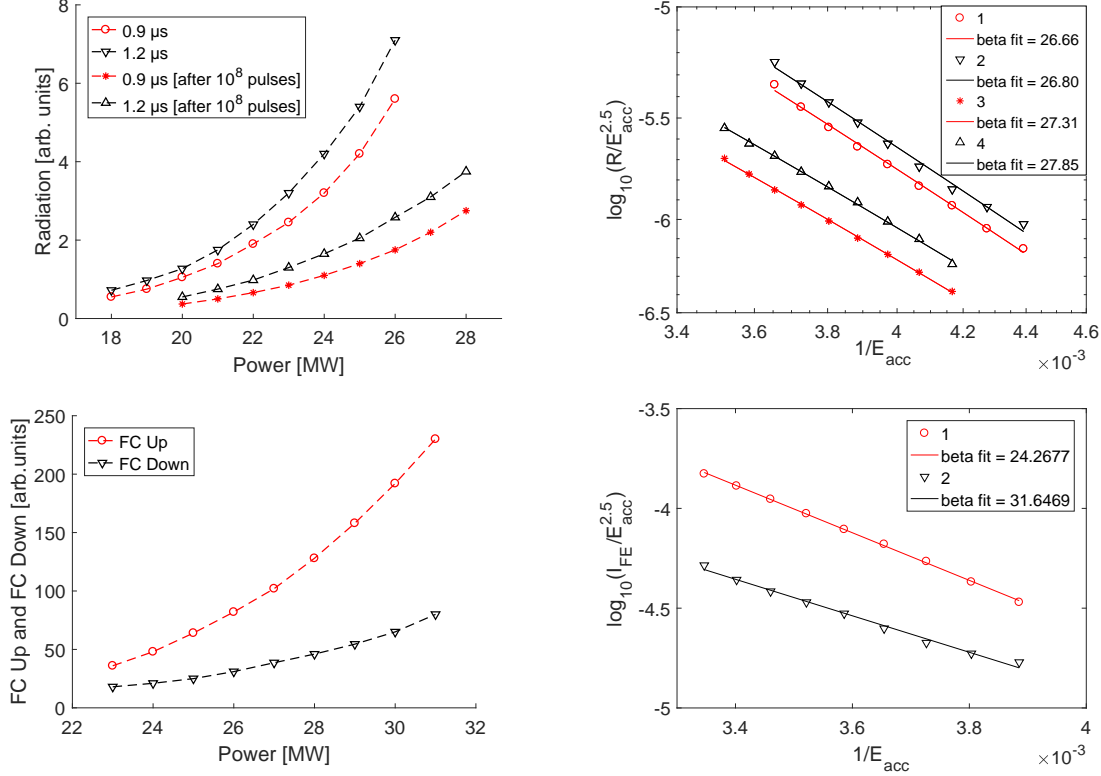


Figure 2.20: Dependence of the radiation level (top) and the dark current (bottom) as a function of the incident power during conditioning (left). Linear fit of the Fowler-Nordheim formula (right), where  $R$  is the radiation, that is proportional to the dark current.

background noise in the beam position monitors, and also ionizing radiation. Therefore several measurements for determining the electron field emission were also performed. To quantify the quality of the surface of the AS, a power scan measuring the radiation and the dark current level were performed by an ionizing radiation monitor and the Faraday cups. The top part of Fig. 2.20 shows that the radiation level of the AS depends on the pulse length and magnitude of the applied RF field. The value decreases with the testing time following condition theory. The upstream and downstream dark current values as a function of the input RF power are presented in Fig. 2.20 (bottom). The radiation and the signals measured via the FCs are considered, as these parameters are directly proportional as shown in Fig. 2.21 (left). All this information need to be taken into account for the radiation protection of facilities and equipment.

The amplitude of the dark current emitted from the AS follows the Fowler-Nordheim model described in Eq. (1.31). The numerical value of the enhancement factor  $\beta_{FE}$  can be obtained by plotting  $\log_{10}(I_{FE}/E_s^2)$  versus  $1/E_s$  [74]. In the right part of Fig. 2.20, the measured points fall on a straight line, and we could obtain the enhancement factor  $\beta_{FE}$  by calculating the inverse of the slope. The value of  $\beta_{FE}$  slightly increases with the

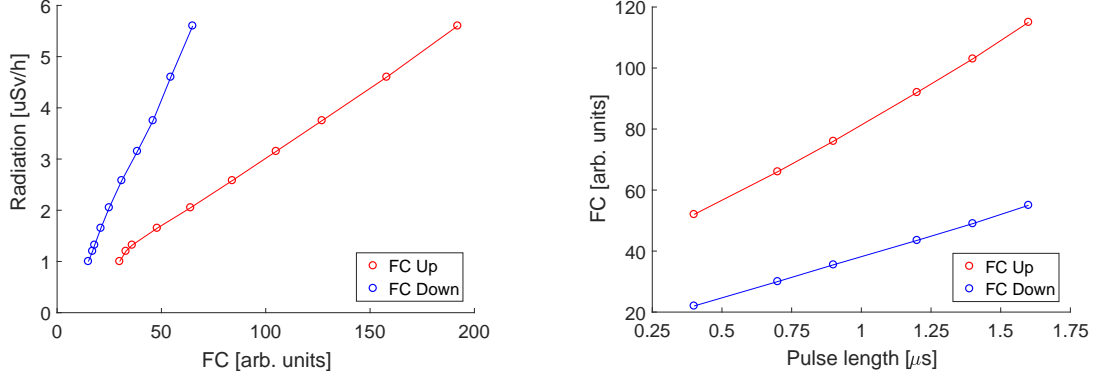


Figure 2.21: Radiation versus FC signals for pulse length of  $1.2 \mu\text{s}$  (left) and dark current versus pulse length for the accelerating gradient of  $70 \text{ MV/m}$  (right).

testing time being around  $\simeq 27$ . In the first measurement, when the pulse length was increased from  $0.9 \mu\text{s}$  to  $1.2 \mu\text{s}$ , the emission increased too, but the enhancement factor did not change significantly. After some conditioning time, there is a reduction of the emitted current. The measurement was performed when the structure reached the design parameters. The dependence of the emission current as a function of the pulse length at  $70 \text{ MV/m}$  is presented in the right part of Fig. 2.21. The value of  $\beta_{FE}$  is comparable to the values of the X-band AS tested at CERN [75]. These results show very good performance of the surface during the conditioning process.

The current measured by the Up and Down FC throughout the test of the S-band BTW HT is presented in Fig. 2.22. The value of the dark current changes during conditioning

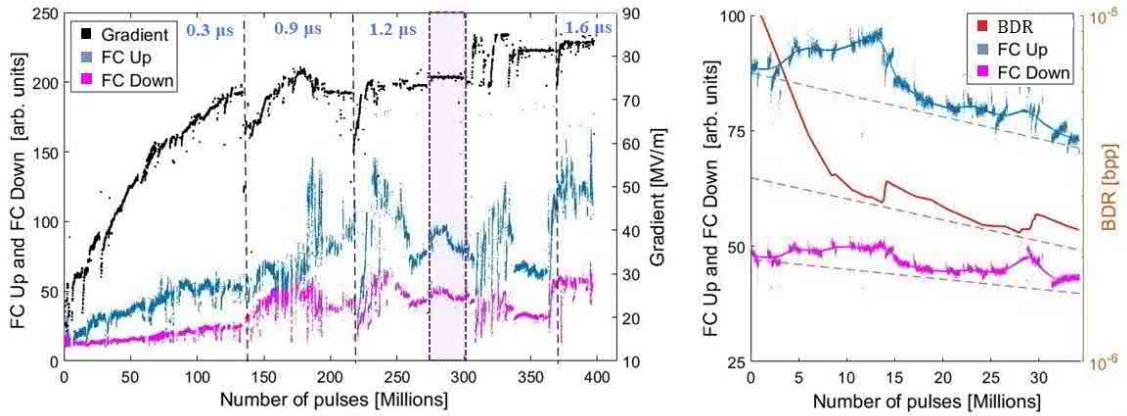


Figure 2.22: History of Up and Down FC signals during conditioning of S-band BTW HT. The vertical dashed lines separate areas with different pulse lengths (left). Zoom part of the history plot: dark currents signals together with the BDR at conditioning with constant power of  $30 \text{ MW}$  and pulse length of  $1.2 \mu\text{s}$  (right).

of the structure. The value of Up FC is about two times higher than value of Down FC which is associated with particle acceleration in the opposite direction of RF field. To evaluate the emission reduction during conditioning, a selected fragment of the history plot is presented in Fig. 2.22 (right) which corresponds to the test with a constant power of 30 MW and the pulse length of 1.2  $\mu$ s.

From these results we can conclude that the current value is different for the same accelerating gradient at different stages of conditioning. This could be explained by the activity of the structure. The values of the Up and Down FC signals at regular pulses depends on the dominant location of the BDs and the length of the incident signal.

### 2.4.5 A statistical analysis of breakdowns

A statistical analysis of the properties of the occurrence of BDs is performed to optimize accelerator conditioning and operation algorithms [76–78]. The attempts to understand the pattern of these events were also made for the medical AS prototype. The distribution of BDs over time has also been investigated. This study is interesting due to the fact that BDR during the period of measurement is not constant in time. This can be seen in Fig. 2.23, which shows the accumulated number of BDs as a function of the number of pulses for the S-band BTW HT. The variation in the slope of the curve indicates that the BDR changes during the HG operation. A staircase form is visible due to the clusters of several BDs that have been triggered in short intervals of time. The average value is about  $2.7 \times 10^{-6}$  bpp. In this case (Fig. 2.23), the BD events recorded during the conditioning process with constant power corresponding to 80 MV/m at 1.2  $\mu$ s pulse length were selected. After each BD, the pulsing was stopped to restore the system. The

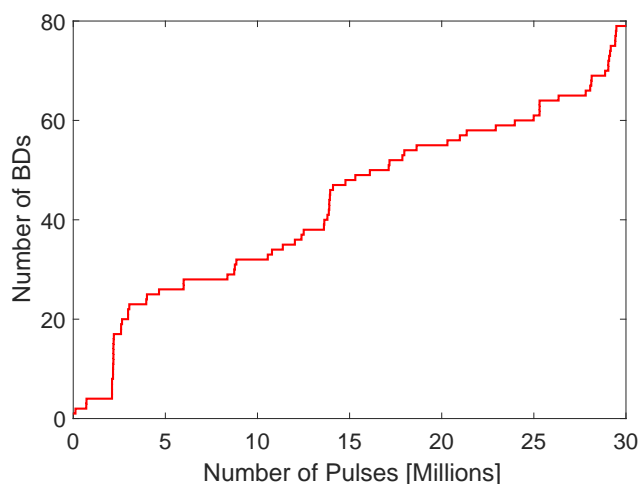


Figure 2.23: History of the cumulative number of BDs with respect to the number of triggered pulses recorded during a period of the test of the S-band BTW HT at constant power.

input power was ramped up step-wise toward a set-point value after consecutive number of pulses (typically 1500) since last BD and increased or decreased depending on whether the BD occurred according feedback loop (3000 - 7000). Control algorithm parameters were manually adjusted depending on the behaviour of the structure.

If BDs are uncorrelated random events, than they can be described by a Poisson distribution. This distribution assumes that events occur at a constant event rate independently of each other. A numerical probability density function (PDF) as a function of the number of pulses between BDs was calculated and the result are presented in Fig. 2.24. PDF has the form of a sum of two exponential which are shown as two sloping lines crossed at one point. Part of the data from the low end was not taken into account since it is occurring due to a ramp up of the power to the set point value. The two terms of the fit are used to obtain the probability of primary BDs which occur randomly and follow-up (secondary) BDs as direct result of a previous BD [78].

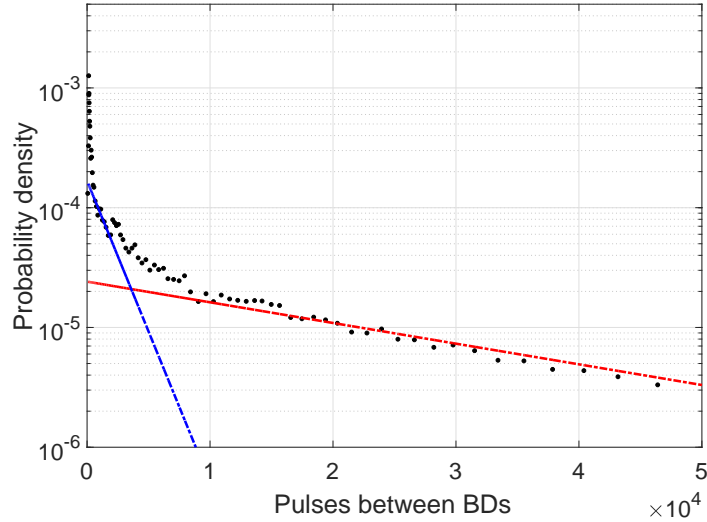


Figure 2.24: Distribution of number of pulses between consecutive BDs and two-exponential fit.

The fit of each PDF can be described by the following equation:

$$PDF(n) = A \exp(-\alpha n) + B \exp(-\beta n) \quad (2.3)$$

where  $n$  is the number of pulses between BD events. It is assumed that  $\alpha < \beta$  to denote the first term correspond to gentler slope and the second term to the steeper slope at the start of the distribution.

Based on the Poisson model, the function can be viewed as a superposition of two correlated BDR terms [78] and, in the simplest form, is represented as:

$$g\Delta(n_{pulses}) = A_1 \exp(-BDR_1\Delta(n_{pulses})) + A_2 \exp(-BDR_2\Delta(n_{pulses})) \quad (2.4)$$

where the normalization is defined by the following expression:  $A_1/BDR_1 + A_2/BDR_2 = P_1 + P_2 = 1$ .  $BDR_1$  characterizes of random primary BDs that limit the performance of the structure.  $BDR_2$  corresponds to secondary BDs that occurred as a consequence of the damage that remained from the previous event. The value of  $P_1$  and  $P_2$  estimate their integrated probability respectively. A PDF of a number of pulses to BD was computed for entire conditioning test and for each pulse length separately. The results of the fitted parameters can be found in Table 2.2.

Table 2.2: Parameters of S-band BTW HT data and the two-exponential-fit results of the PDF distributions of the number of pulses between BDs for different pulse lengths and different gradients for 1.2  $\mu$ s.

<b>Pulse length</b> [ $\mu$ s]	<b>0.35</b>	<b>0.9</b>	<b>1.2</b>	<b>1.6</b>	<b>Total</b>
Total number of BDs	5000	1899	996	948	9500
BDR [ $10^{-5}$ ] bpp	3.14	2.5	0.68	2.89	2.26
Cross point	5024	2135	75192	1100	3410
Primary BDR [ $10^{-5}$ ] bpp	4.05	5.21	0.27	3.02	3.97
Secondary BDR [ $10^{-4}$ ] bpp	3.35	14	0.53	19	5.84
$BDR_2/BDR_1$	8.27	26.87	19.63	62.91	14.71
$P_1$	0.65	0.61	0.31	0.54	0.7
$P_2$	0.35	0.38	0.69	0.46	0.3
$P_2/P_1$	0.54	0.62	2.23	0.85	0.43

<b>Gradient</b> [MV/m]	<b>55</b>	<b>56.5</b>	<b>60</b>
Total number BDs	133	82	109
BDR [1e-6] bpp	6.3	2.4	3.77
Cross point	3797	78600	29720
Primary BDR [1e-6] bpp	17.5	0.79	6.1
Secondary BDR [1e-5] bpp	0.86	4.37	7.52
$BDR_2/BDR_1$	49.2	55.3	12.3
$P_1$	0.65	0.61	0.55
$P_2$	0.35	0.39	0.45
$P_2/P_1$	0.54	0.64	0.82

The BDR of secondary BDs is much higher than the primary. A difference in the ratio  $P_2/P_1$  is observed as well. These values give an estimation of the number of secondary BDs that are produced per each primary event during the HG test. The number of primary BDs is predominant when conditioning of the structure, but this ratio may change for a well-conditioned structure. In the general case, the probability of the primary BDs versus the secondary is 60 % higher when tested according to the algorithm limited by BDR. The result obtained for 1.2  $\mu$ s demonstrates the effect of conditioning state on the BD probability function. The values for this pulse length are completely different from

others due to the fact that this measurement includes various testing modes. Therefore, testing at different values of power for this pulse length are considered separately. The results presented in the bottom part of Table 2.2 clearly demonstrate that the BDR is decreasing over time while increasing the probability of secondary BDs and the interval between them.

The BD distribution within the structure during testing at an accelerating gradient of about 80 MV/m is shown in the left part of Fig. 2.25. The most of the BDs located at the front part of the structure. The plot of the BD distribution against the number of conditioning pulses (Fig. 2.25 (right)) demonstrates that during 25 million pulses the BDs were distributed in the same region of the structure. This study shows that the individual pulse induces a secondary BD in a highly sensitive area to BD caused by a previous BD event. This can be explained in terms of strong emission current from the surface under the influence of an external electric field. A similar trend of the PDF is observed in the statistics of the previously tested CLIC X-band ASs.

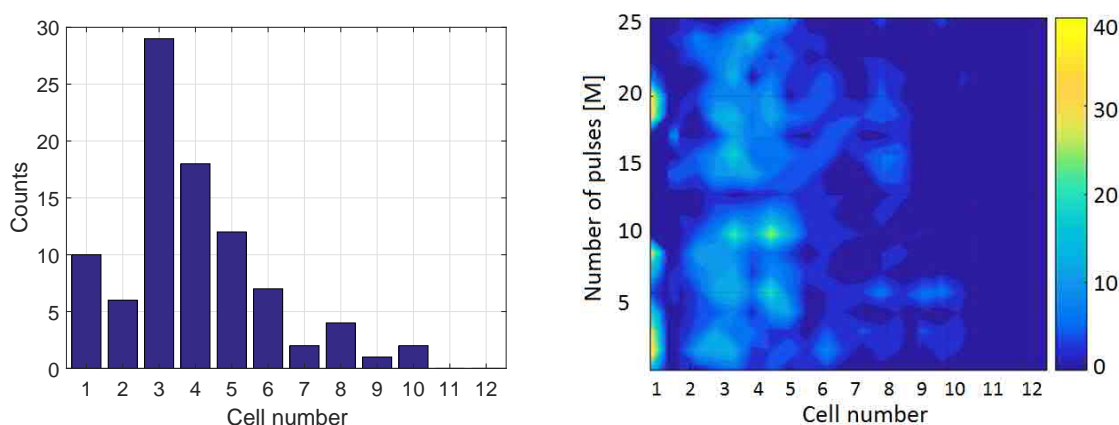


Figure 2.25: BD distribution along the structure during a period of the test with a constant accelerating gradient of about 80 MV/m

#### 2.4.6 Post-processing analysis

In order to determine the changes of the RF properties of the S-band BTW HT after the high-power test, the low-power RF measurements have been carry out. In addition, a borescope inspection has been also used to observe the visible physical damage of the inner surface.

#### Low-power RF measurements

As shown in Fig. 2.26, the AS was mounted vertically at the bead-pull setup at CERN. A dielectric bead was placed on a string aligned with the beam axis and pulled along all cells to measure the S-parameters using a VNA. During measurements the AS was under dry nitrogen flow to avoid influence of air humidity in the electric permittivity inside

the structure. The neylong string used to hold the bead causes field inhomogeneity. To correct this effect, the S-parameters measurements with and without the string have been performed. Temperature was also monitored. The frequency offset of the nitrogen, the temperature and the thread for bead-pull are calibrated. Taking into account all these conditions, the resonant frequency and the phase advance of each cell of the structure were determined. The state of the cavity cells was also inspected before and after the tuning in the same way.

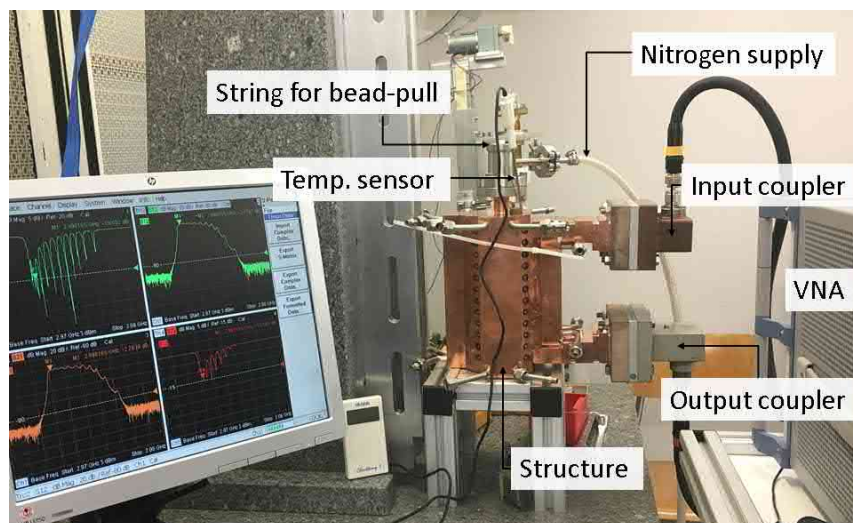


Figure 2.26: Picture of the S-band BTW HT at the post-processing test in the CERN clean room.

The further comparison of the various parameters of the S-band BTW HT have been made before (described in section 2.2) and after high power testing. The measurements of the complex scattering parameters  $S_{11}$  and  $S_{22}$ , corresponding to the input and output RF port demonstrate that the frequency of the regular cells did not change in general. There is a noticeable detuning of the last two and first two cells, which results in -20 dB input reflection at the desired conditions. The magnitude of  $S_{11}$  results have changed from -60.2 to -19.6 dB and  $S_{22}$  from -24.3 to -15 dB at the central frequency of 2.9985 GHz as shown in the top part of Fig. 2.27. The field distribution is almost flat and the phase advance per cell is in the range  $145^\circ - 155^\circ$  as illustrated in bottom part of Fig. 2.27. Small local changes can be seen in the first and the last cells of the structure after the test. Cells 3 to 10 changed only marginally in frequency (within  $\pm 0.1$  MHz), while a frequency shift of the first two and last two cells of up to 1.1 MHz occurred. The  $S_{11}$  parameters in the complex plane are slightly detuned as shown in top part of Fig. 2.27. The quality factor of the structure was insignificantly reduced from 7074 to 6823. The results are presented for nominal parameters at a operating temperature of  $32^\circ\text{C}$  under the vacuum.

The low-power RF measurements indicated that the AS has minor changes after the high power test. Therefore the structure can be reused without retuning.

2.4. High-power conditioning and analysis of results

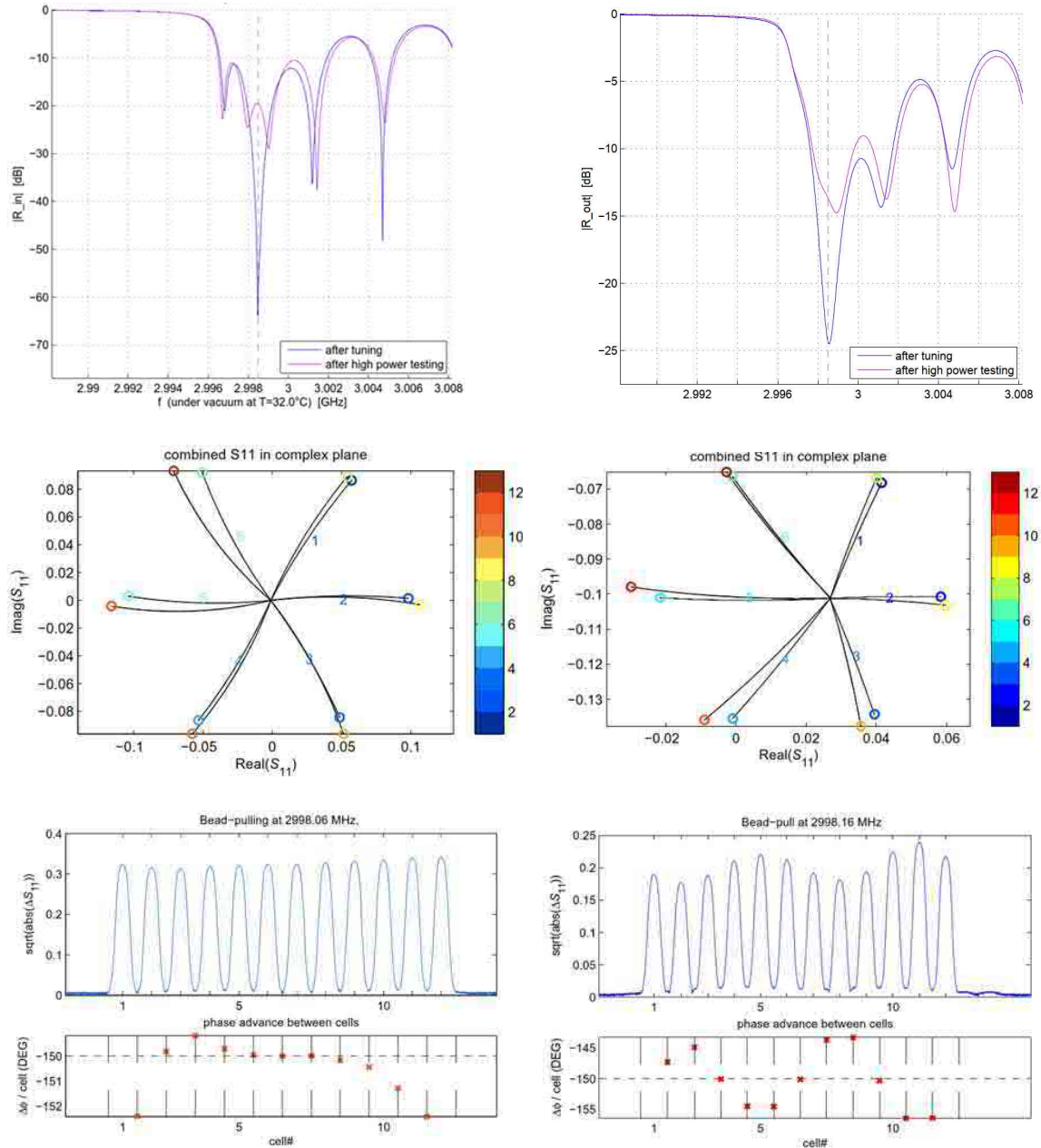


Figure 2.27: Top: Comparison of the input (left) and output (right) reflection “after tuning” and “after high power testing”. Electric field pattern along the S-band BTW HT combined  $S_{11}$  in the complex plane (middle) and in magnitude and phase advance per cell (bottom) before (left) and after high power test (right).

## Borescope inspection

After the low-power RF measurement was completed, the surface of the AS was inspected by the borescope. A picture of the borescope setup is shown in Fig. 2.28. This technology is used as a non-destructive test for recognizing defects or imperfections on the internal cavity surfaces. The observation was done to determine the location of the BDs for example to cross check against the longitudinal BD position distribution obtained from the RF measurements and to see the relative occurrence of BDs on the nose and on the coupling holes. The borescope was introduced through the beam pipe and through the input of the iris as shown in Fig. 2.29.

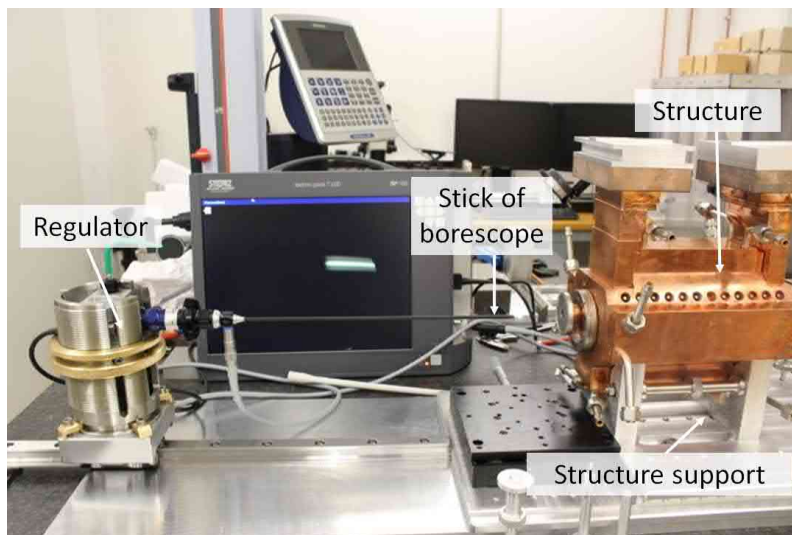


Figure 2.28: Borescope inspection of the S-band BTW HT at CERN. The regulator performs Y-adjustment, rotation and linear displacement on manual roller. [Courtesy of Serge Lebet.]

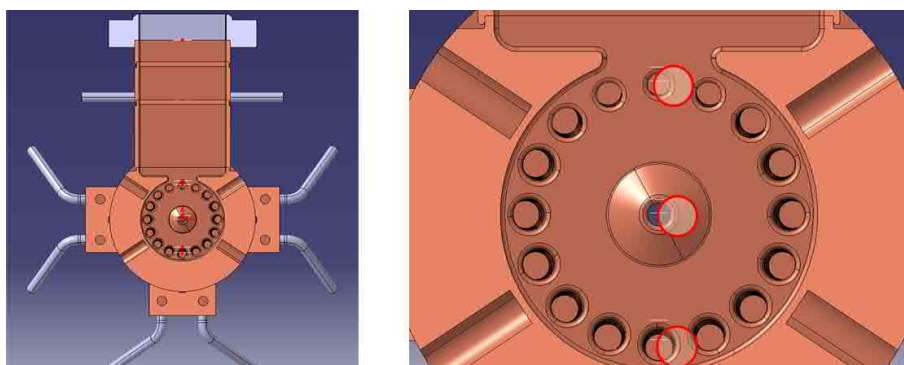


Figure 2.29: Cross section of the input waveguide (left) and enlarged areas (right) around the cell where the borescope analysis has been performed.

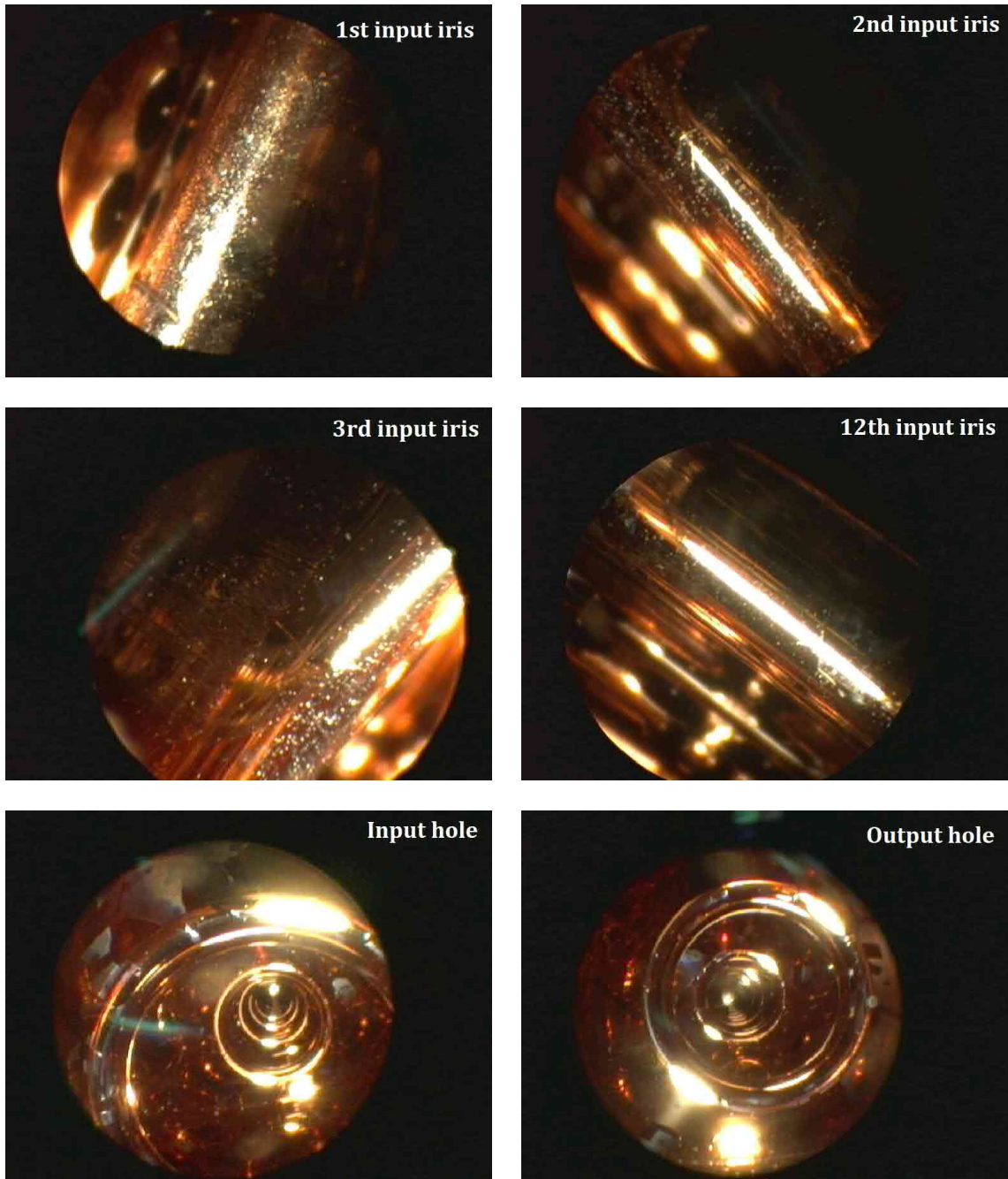


Figure 2.30: Borescopy images from the S-band BTW HT after high power test: the iris of the 1st, 2nd (top), 3rd and 12th (middle) cells, one of the coupling holes of input and output cells (bottom).

Pictures from the borescope showed that most of the BDs occurred in the first cells of the input power of the structure. The examples of the hole iris are shown in the bottom part of Fig. 2.30. No significant damage of the surface around the holes is detected. These measurements confirm the reliability of the data analysis based on the difference in time of the RF signals and that BDs occur at area of high electric field according RF field distribution presented in Fig. 2.10.

At this moment, the S-band BTW HT is stored remaining in a nitrogen environment to prevent surface contamination. The structure is scheduled to be retested in the correct position.

## 2.5 Comparative analysis of RF accelerating structures

A comparative analysis of the different conditioning histories of tested prototype allows to efficiently reduce the time to achieve their best performance and to minimize the probability of BDs. A stable mode of operation is necessary for the performance of all linear accelerators, in particular, for proton therapy. Since this requires an operation of the accelerator complex without BDs during the whole treatment session what means less than  $7.7 \times 10^{-7}$  bpp/m.

More than ten different CLIC X-band RF ASs have been tested by the CLIC RF group up to now. A detailed comparison of the their conditioning result has been made to determine the best test procedure to assess the RF design and the fabrication technology. The conditioning histories of the S-band BTW HT and three different CLIC X-band AS prototype tested at CERN have been chosen for comparison. The main features of these structures are listed below:

- **TD26CC**: a CLIC design, 11.994 GHz, 26 cells, equipped with HOMs, damped, tapered and with Compact Couplers. Discs were manufactured at VDL [79], and assembled at Bodycote [80], under the supervision of X-band production team at CERN. TD26CC N1 and TD26CC N3 were tested in Xbox-1 and 2 respectively.
- **T24 PSI N2**: a CLIC design, 11.994 GHz, 24 cells, the HOMs, without damping, tapered. The discs were manufactured at VDL, assembled at PSI [81]. The AS was tested in Xbox-3.
- **TD24CC SiC**: a CLIC design, 24 cells, tapered and damped with Silicon Carbide (SiC) absorbers. Discs and manifolds were manufactured at VDL, assembled at Bodycote, under the supervision of X-band production team at CERN. The AS was tested in Xbox-3.
- **S-band BTW HT N1**: a medical design for TULIP project, 2.9985 GHz, 10 regular and 2 coupling cells, not tapered. The discs were manufactured at Yvon boyer [82], assembled at Bodycote, under the supervision of X-band production team at CERN. The AS was tested in Sbox. A detailed description can be found in Section 2.1.

All these structures, that we will use for the comparison, have been conditioned with the same algorithm. The strategy involves a stepwise increase of input RF power at a fixed pulse length to nominal gradient. This process is repeated until the nominal input power is reached, or if the BDR does not stabilize anymore, which indicate that the maximum field has been reached at this pulse length. The structure is considered to be fully conditioned when the BDR does not decrease at nominal gradient and pulse length.

After the conditioning, all the structures met the design specifications. The electric field as a function of the number of the RF pulses are presented in Fig. 2.31. These results show that the structures are behaving quite similarly in terms of conditioning speed. The S-band BTW HT and the CLIC X-band acceleration prototypes reached an estimated gradient of 50 and 100 MV/m after 200 millions pulses, respectively. The conditioning process of each structure could be limited by the algorithm, available input RF power, or individual conditioning speed of the structure. However the accelerating gradient  $E_{acc}$  is not a relevant parameter to predict the best performance of a structure since this is a resulting characteristic depending on influence of other multiple factors. Therefore, other quantities such as the surface electric field  $E_{surf}$  and the modified Poynting vector  $S_c$ , should be also used to describe the conditioning process:  $E_{acc} = k_E E_{surf}$  and  $E_{acc} = k_S \sqrt{S_c}$ , where  $k_E$  and  $k_S$  are constants characterizing the structure. The surface electric field is difficult to compare in our particular case for S-band BTW HT, because the value of  $E_s/E_0$  is twice the value of CLIC X-band prototypes as shown in the top part of Fig. 2.32. This structure has different behaviour compared to the CLIC ones.

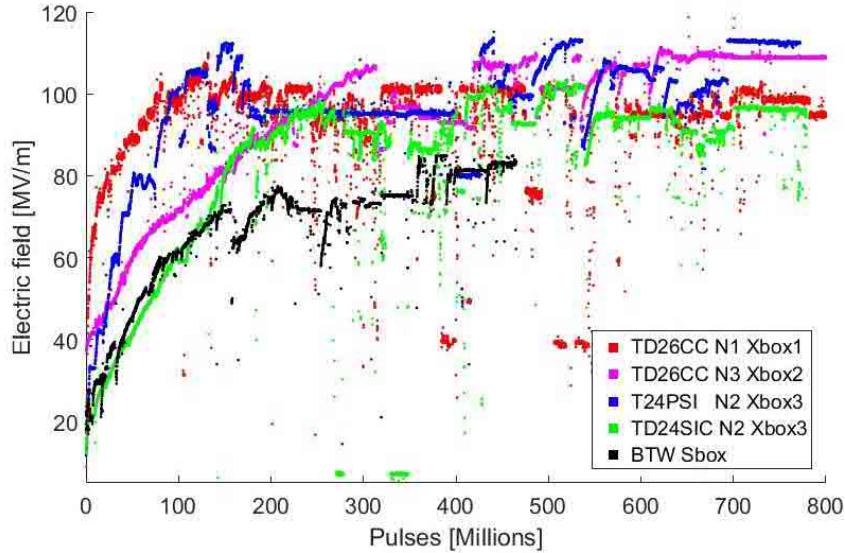


Figure 2.31: Comparison of the electric field of different prototypes with respect to the number of pulses for S-band BTW HT and CLIC X-band structures.

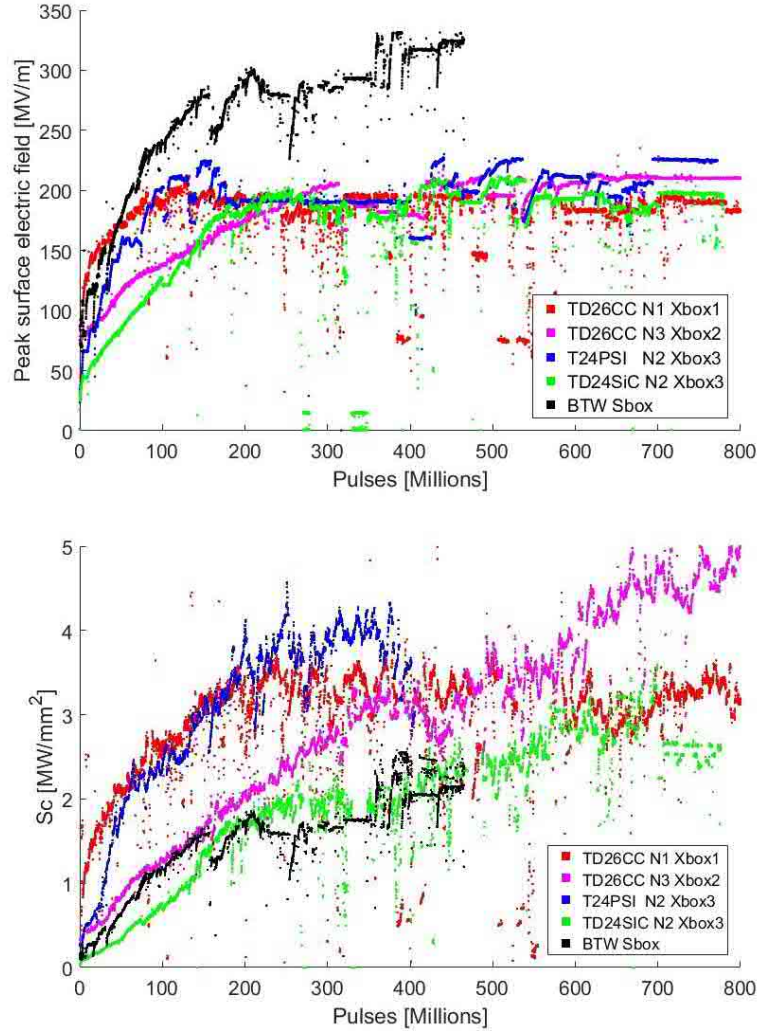


Figure 2.32: Comparison of the surface electric field  $E_{surf}$  (top) and the modified Poynting vector  $S_c$  (bottom) of different prototypes with respect to the number of pulses for S-band BTW HT and CLIC X-band structures.

In order to directly compare the behaviour of the different AS, the data must be scaled to some parameters. The most significant are the pulse length and the BDR. Based on Eq. (1.36), a **scaled gradient**  $E_{scaled}$  can be defined as:

$$E_{scaled} = \frac{E_{acc} * \tau_p^{1/6}}{BDR^{1/30}} \quad (2.5)$$

Using the established scaling laws, operational data can be represented in a smoother progression in their conditioning, despite the changes in operating conditions. Accordingly, the conditioning histories of the structures are presented in Fig. 2.33 (top), using a scaled

electric field. The data was normalized to CLIC parameters:  $BDR = 1 \times 10^{-6}$  bpp/m and  $\tau_p = 200$  ns. From this data, it is demonstrated that such normalization is quite suitable also for the S-band BTW HT. In turn, the CLIC structures have similar behaviour at late stages of conditioning. The TD26CC N3 structure shows the best performance in Fig. 2.32. Despite, the high gradient values, a total performance of the structure cannot be determined since the normalized gradient gradually increases during the entire test. The tests of T24PSI N2 and TD24SIC N2 structure were terminated due to the limitation in RF power of test bench. No significant effect is shown in case of damped and undamped AS.

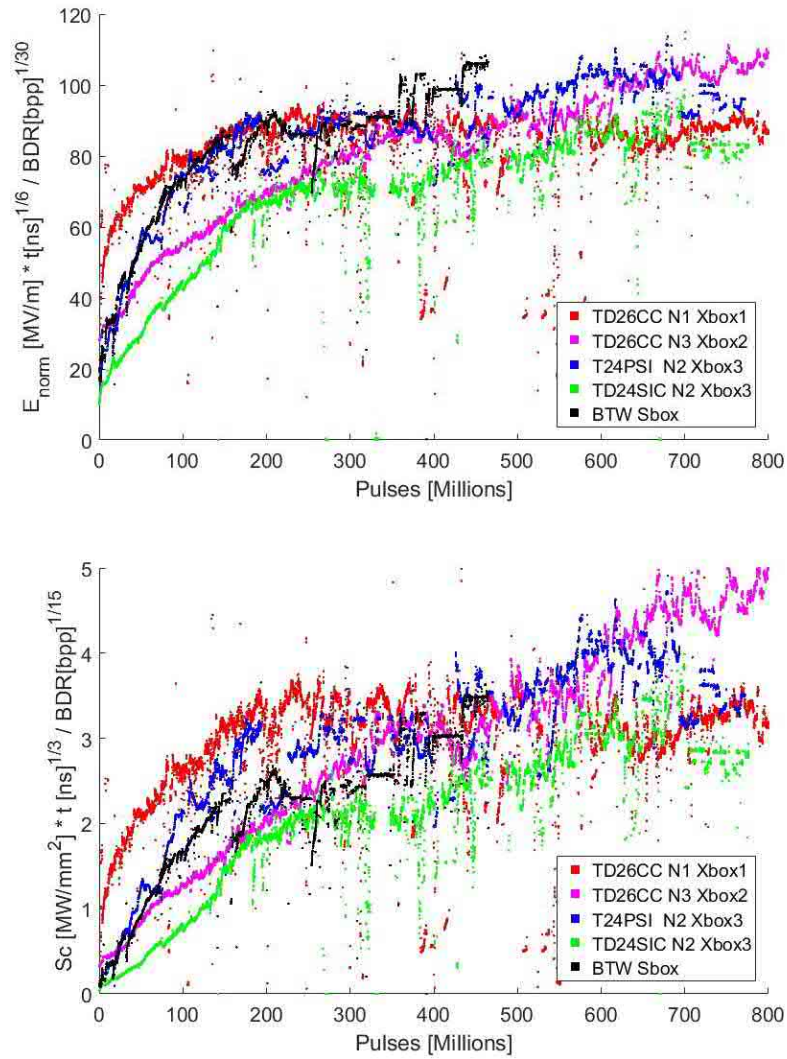


Figure 2.33: Comparison of the scaled electric field  $E_{norm}$  (top) and the scaled modified Poynting vector  $S_c$  (bottom) with respect to the number of pulses for S-band BTW HT and CLIC X-band structures.

The stabilization of the normalized curve of the TD26CC N1 indicates the complete conditioning of the structures.

The cavities have been also compared in terms of the **scaled modified Poynting vector**  $S_c$  by applying the scaling law:

$$S_c \text{ scaled} = \frac{S_c * \tau_p^{1/3}}{BDR^{1/15}} \quad (2.6)$$

These results are presented in the bottom part of Fig. 2.33. All the structures show a smaller difference when comparing the peak modified Poynting vector with respect to the peak surface electric field. The Poynting vector characterizes better the high gradient limits of these cavities. However, the BDR measurement presented in Section 2.4.1, shows a scaling law with a power of 10 for the accelerating gradient. In the future this can be used for comparison of the test results of similar design structures.

There is a particular interest in studying the long-term behaviour of this kind of AS in order to find the maximum gradient for stable operation and to estimate the time required to complete the conditioning process necessary to achieve the target performance. The CLIC prototypes and S-band BTW HT have different requirements regarding stability of the operation. However the results of the S-band cavity test seem consistent with the results from X-band experiments, and constitute the first experimental data for the prototype of proton therapy at 3 GHz frequency. The peak surface field is more than 350 MV/m at different pulse lengths, see the top part of Fig. 2.32. This value has never been achieved in similar RF structures.

The Fig. 2.34 shows the steady decrease in the BDR over multiple months of running of the S-band BTW HT as a function of the number of pulses in double-logarithmic scale.

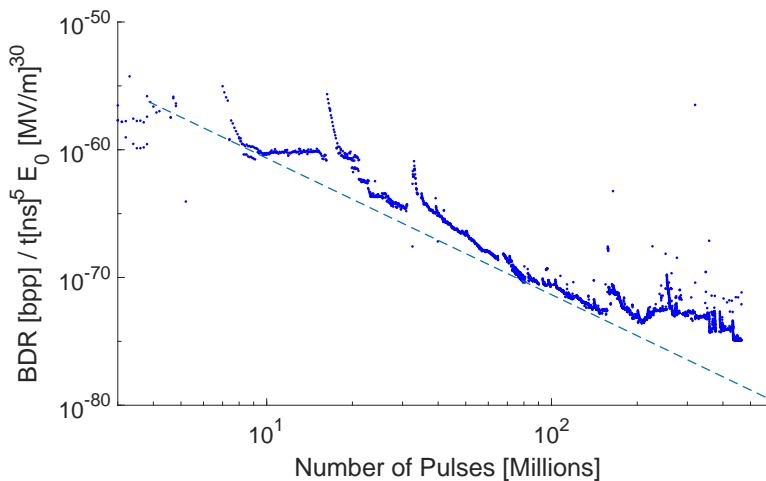


Figure 2.34: Normalized breakdown rate for the S-band BTW HT structure tested at CERN Sbox.

The behaviour of the AS actually improve with time. The structure's conditioning is performed with the intention of reducing the BDR. The conditioning trend starts to deviate from the fit after about  $2 \times 10^8$  pulses. The conditioning state, which no longer improves, will demonstrates the achievement the limiting parameters of the structure. The evidence of a conditioning limit in RF structures needs to be further investigated with longer tests that accumulates more pulses and BDs. After a gain in the HG performance, the further operation of the AS have to be performed at accelerating gradient around 10 - 20 % lower to avoid damage of the AS surface.

To summarize, we could confirm that the S-band BTW HT provides the required RF parameters of compact hadrontherapy linacs. The high power testing showed that this AS can operate with high accelerating gradient that correspond to 80 MV/m at the first cell or 65 MV/m average value for 1.2  $\mu$ s pulse length with a BDR of  $4 \times 10^{-6}$  bpp. If we recalculate to the appropriate requirements for TULIP project, taking into account the pulse length and the BDR using the scaling law  $BDR \propto E_{acc}^{30} \tau_p^5$  (Eq. 1.36), then this corresponds to 55 MV/m average gradient.



## Chapter 3

# Experimental studies of RF breakdowns in RFQs

RFQ technology has considerably progressed in recent years in terms of RF design, beam dynamics design, tuning techniques, availability and reliability of construction techniques, etc. The RFQ is widely used as injector by major laboratories and industries for ion linear accelerators [83]. The RFQ represents the best transport option between the unbunched beams that come out of ion sources and the bunched and accelerated beams that are required by downstream RF AS.

HG is a very important requirement for different types of ASs including RFQs since high fields increase the RFQ performance in areas of higher acceptance (larger emittance beams), and gives greater space charge capability and acceptance even for heavy ions with lower charge state. In addition, HG opens the possibility to reduce the overall length of accelerators, that requires higher RF frequencies. But high fields have limitations, and the study of these limitations is the main objective of this work. In particular, based on BD studies of HG CLIC prototypes, we target a high surface electric field in the RFQ while minimising risk of sparking and damage.

The typical frequencies used for proton linacs range from 200 to 750 MHz. The AS design can be realized with different kinds of resonator types which determine the efficiency of the RFQ, the cost, the size, and the construction feasibility. In order to improve the performance of the RFQ, it is necessary to increase the gradient, which means to maximize the field on the vane-tip. This can be done taking into account the proportion between transverse acceptance and efficiency of acceleration (modulation factor), and by minimising the transverse radius of curvature that leads to higher frequency. The impact of the main parameters on the choice of frequency is described in Chapter 1. Examples of RFQs with different frequencies and the main operation parameters are summarized in Table 3.1. There are the most advanced structures that are of particular importance for scientific and society applications. A number of innovative design solutions with higher frequencies and higher gradients have been adopted to minimize cost and to contribute to the future of industrialization.

Table 3.1: Parameters of the RFQs.

Structures, value	Frequency [MHz]	Energy [MeV]	Length [m]	Gradient [MeV/m]	Current [mA]
MedAustron RFQ	216.8	0.4	1.25	0.32	4
Linac4 RFQ	352.2	3	3	1	90
HF-RFQ	750	5	2	2.5	0.400

An overview of the main applications of these structures is presented below:

- The **MedAustron RFQ** is designed to accelerate protons and carbon ions from 8 keV to 400 keV for one of the most cutting-edge centers for cancer treatment and research, located in Wiener Neustadt (Austria) [84]. The center started treating patients in 2016 with protons and in 2019, with the availability of carbon ion therapy. This RFQ is 4-rod structure with slim electrodes of 1.25 m length operated at 216.8 MHz.
- The **RFQ Linac4** is the next step of the progress, that provides significantly higher gradient than other existing structures. The Linac4 RFQ has been designed to provide the beams to the PS Booster injector. The 352.2 MHz RFQ accelerates the H- beam from the RF source to the energy of 3 MeV. This RFQ has the 4-vane design.
- The **High-Frequency (HF)-RFQ** is a complex structure with higher precision requirements due to the tight tolerances and machining. The HF-RFQ targeted at low current applications requiring small dimensions, low cost, low radiation emissions, minimum maintenance, up to portability. Additional limitations come from the beam acceptance. The relatively higher operating frequency and small bore aperture radius have been realized with the 5 MeV 750 MHz RFQ for a specific proton therapy accelerator. This RFQ has been constructed as alternative to cyclotrons as injector for linacs operating at higher frequency. Its overall design is general enough to be used for other applications, such as medical radioisotopes production and ion beam analysis of industrial components or of artworks. The gradient was chosen to be safe for stable operation. The RFQ has a design similar to the one of Linac4.

In this chapter, two RFQs with high (750 MHz) and low (352.2 MHz) frequencies were studied. Notice that, this is one of the first time a systematic study of BDs in RFQ is reported.

### 3.1 Breakdown measurements in 750 MHz HF-RFQ for hadron therapy applications

The BD studies were performed in the tests of the HF-RFQ in the experimental area at building 2250, Point 2 of CERN. The measurements were made with beam during

the conditioning of the different RF components. The data have been collected without disturbing the normal operation regime.

### 3.1.1 The LIGHT system and the HF-RFQ

The Advanced Oncotherapy (AVO) company [49] is developing a next-generation proton therapy system for cancer treatment known as LIGHT system, which is the result of many years of work at CERN and ADAM company [89]. The LIGHT system has been designed to provide a high beam quality of protons with energies up to 230 MeV, required for effective proton therapy treatment of deep-seated tumours. One of the target of this facility is to significantly reduce the treatment cost of patients, and to be able to install it in small to mid-size health care centres.

The main advantages of LIGHT compared to other existing systems as:

- **High frequency.** The linac has the highest frequency ever used in proton-therapy. The high repetition rate of the very short pulses (a few  $\mu\text{s}$ ) gives the possibility to vary the energy and the pulse current on a pulse-to-pulse time scale.
- **Precision.** The system has an active longitudinal modulation along the beam propagation axis, that provides a change in treatment depth, and a dynamic transverse modulation that allows a precise 3D treatment of the tumours.
- **Modularity.** The system consists of a assembly of modular units that can be extended to higher energies by additional units or replacement with newer and improved ones.

The AVO company has successfully integrated the main sections of the linac in a testing facility in October 2018 [85]. The main parts of LIGHT accelerator are presented in Fig. 3.1. The present design uses a proton source from Pantechnik (Monogan M-1000) [86] that produces proton beams and chops them to pulses at 200 Hz. After the source, the beam is injected into RFQ, developed by CERN. The RFQ is followed by four modules of SCDTL, based on the experience of the IMPLART project of ENEA (Frascati, Italy) [87]. Finally the last section consist of CCL structures, designed by ADAM based on the experience of the LIBO prototype [47].

After a successful test of the main components of the linac at CERN, the work is progressing at Daresbury Laboratory to build and prepare the test facility ready for the installation and assembly of the full LIGHT system. The LIGHT will be installed in the basement of a townhouse in Harley Street, central London [88].

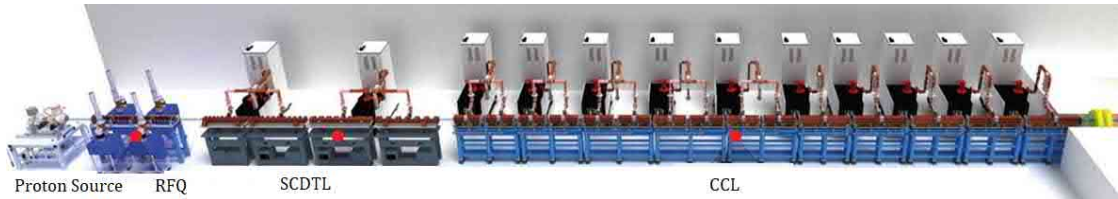


Figure 3.1: General view of full size LIGHT accelerator.

The HF-RFQ is the most compact RFQ ever build operating at 750 MHz and capable of producing low-intensity beams with no significant losses. The prototype of such RFQ has been built for ADAM company by CERN with the support of the KT, CERN medical application office. The HF-RFQ have been constructed based on experience in the design of AS for the Linac4 project, adapting the previous TERA technologies, and expertise in HG AS gathered by the CLIC group at CERN.

This structure has about double the frequency of the existing RFQs. The RFQ was constructed to accelerate protons from 40 keV to 5 MeV within only 2 m length, and to minimise beam losses above 1 MeV [90]. The length of the RFQ corresponds to  $5 \lambda$ , which is considered to be close to the limit for field adjustment using only piston tuners. It consists of four modules with a length of about half a meter each. The RFQ frequency has been selected to be a sub-harmonic of 3 GHz as required for the application in proton therapy. While the higher frequencies decrease the acceptance, increase the power loss density and make difficult the machining of the first cells [91].

The electrode voltage is designed to be constant along the RFQ that requires a constant longitudinal field distribution. Therefore there are 16 antennas or pickups along the structure (four pickups along each vane) to measure the field during the tuning process. The four power couplers are placed in the two middle segments of the RFQ, one in each quadrant. Fig. 3.2 shows a schematic configuration of the power coupler. The HF-RFQ design is optimised to use multiple units of solid-state amplifiers combined into the HG-RFQ providing high reliability, no High Voltage (HV), and low cost [54]. Each power coupler is fed by a 100 kW Inductive Output Tube (IOT) in order to maintain a nominal voltage of 67.6 kV. The maximum RF peak power is 400 kW, and the maximum electric field on the vane tip is 50 MV/m corresponding to twice the Kilpatrick limit [91]. The Q-factor due to losses in copper is about 6440 according to 3D RF design simulations. The HF-RFQ is designed and built for a maximum duty cycle of 5%, which is required for hadron therapy and other numerous applications.

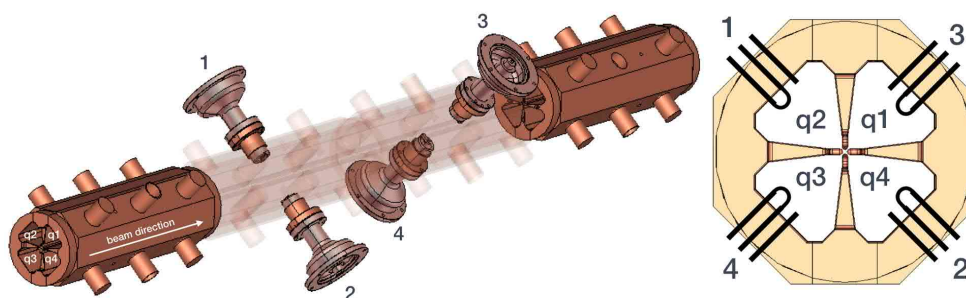


Figure 3.2: 3D drawing of the RFQ with tuners, pumping ports, and power couplers (left) and a cross section of the RFQ indicating the numbering of the quadrants and the power couplers (right).

The HF-RFQ has a high transmission efficiency, which was one of the requirements on the choice of the design parameters. The design was optimized to match the acceptance of

### 3.1. Breakdown measurements in 750 MHz HF-RFQ for hadron therapy applications

the subsequent components of LIGHT, and to minimise the losses at the transition of the two structures to avoid activation of components. The main parameters are summarized in Table 3.2.

Table 3.2: Main parameters of the HF-RFQ at the ADAM test bench.

Parameter	Value
Frequency	750 [MHz]
Length	2 [m]
Vane voltage	65 [kV]
Peak RF power	400 [kW]
Beam Input energy	40 [keV]
Beam Output energy	5 [MeV]

#### 3.1.2 Description of experimental area for the LIGHT accelerator

At the moment of writing this thesis, the first prototype of the LIGHT system was under commissioning at the ADAM testing area [89]. Installation and test of the different components were carried out in stages, starting with the proton source and the RFQ, and continued with the conditioning of the four SCDTLs and two of the high-energy CCLs. The beam commissioning of the RFQ was successfully performed in 2017 and the measurements are reported in [93]. The beam current at the output of the RFQ is  $50 \mu\text{A}$ , and the horizontal and the vertical emittances are  $0.032 \times 0.025 \pi$  mm mrad. Fig. 3.3 shows the layout of the linac during the beam commissioning of the SCDTL cavities up to an energy of 37.5 MeV.

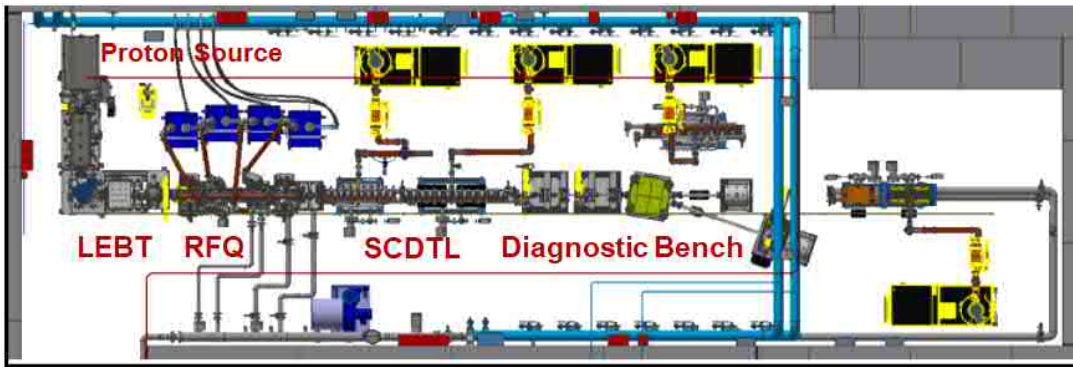


Figure 3.3: Top view of the present configuration of the LIGHT prototype with two SCDTL modules on the beam line followed by the diagnostic test-bench at CERN.

The test bench hosts a control room, a mechanical and electronic workshop, a rack room, and a bunker [94]. Standalone test systems are available to execute 200Hz pulse tests on individual accelerator devices. Fig. 3.4 shows the RFQ installed at the ADAM test facility at CERN.



Figure 3.4: The HF-RFQ after the installation at the ADAM test facility at CERN.

All systems are successfully integrated in the testing facility. The proton beam has been accelerated through all these units up to the design energy of 52 MeV [85]. Today the work is progressing at Daresbury Laboratory to build the full system providing a 230 MeV proton beam acceleration.

The proton injector, including the RFQ and the other tested acceleration modules, are controlled by a dedicated control system. A data-logging system allows to perform data analysis and monitor trends on vacuum, cooling temperature, and RF signals. The accelerator control and safety system are mainly based on commercial hardware: Siemens PLCs and PXIe based electronics.

The LLRF test bench controls the magnitude and phase of the RFQ pulse, ensuring stable system operation. The schematics view is presented in Fig. 3.5. The system provides a cavity field control function, and incorporates the machine protection functions. The cavity is filled by 4 RF ports. The required peak RF power of the cavity is 400 kW at 750 MHz with 200 Hz repetition rate and 10  $\mu$ s pulse length. The HF-RFQ is equipped with RF pickups used to monitor the RF fields inside the cavity and measure transmitted (TRA or PKR) signals. Directional couplers are located before the IOTs to allow the

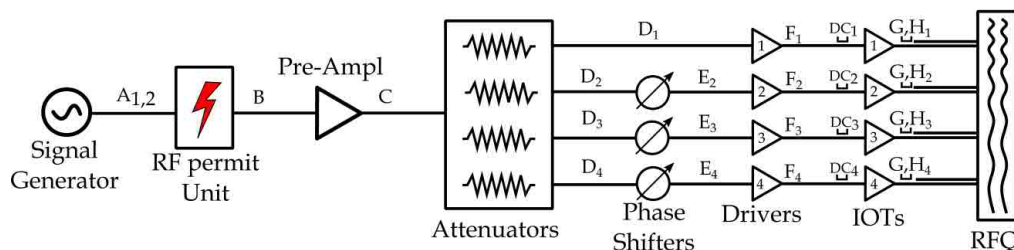


Figure 3.5: General functional block diagram of LLRF system for the HF-RFQ at the ADAM test facility at CERN.

### 3.1. Breakdown measurements in 750 MHz HF-RFQ for hadron therapy applications

measurement of the forward power from drives (Driver FWD), the forward power, and the reflected powers from the cavity (IOT FWD and RFL or REF) by coupling a small amount of power to the waveguide. In this case, the amount of coupling is small enough such that the loss of power in the cavity is less than 0.1 dB.

The RF signals are effectively read and displayed in real time at the Test Bench Control System. The data are sent to a PC in the operator's control room. The waveform graph of these signals and their average values at nominal operation are presented in Fig. 3.6. The peaks at the beginning and at the end of the RFL pulse correspond to the rising and falling time of the FRW RF pulse, where the frequency is different and the power is reflected by the cavity as it is a resonator. The amplitude of the peaks depends on how well the IOTs, the coaxial lines, the HF-RFQ are matched and on the relative amplitude and phase between the four RF signals at the RFQ input. The level of reflection in the middle of the pulse indicates that IOT2 and IOT3 are slightly out of phase. The coaxial lines do not have a circulator to suppress the RFL power, therefore the RFL peaks stay bouncing in the coaxial between the IOT and the RFQ. This creates an SW that is presented in the RFL signal from IOT3 in this example.

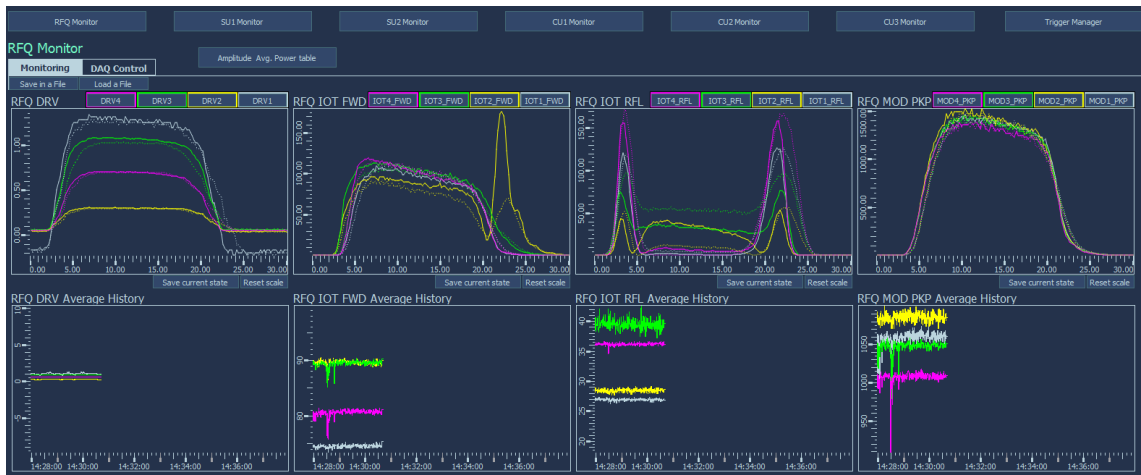


Figure 3.6: Control panel of RFQ signals at the ADAM test facility: 4 Driver FWDs, 4 IOT FWDs, 4 RFQ RFLs, 4 RFQ PKPs (top) and their average values (bottom).

#### 3.1.3 Description of the breakdown measurement set-up at ADAM test area at CERN

The high-power operation of the RFQ is limited by the undesired BDs that cause beam losses and by the capability of the RF power supplies. The primary BD study was done by measuring the FWD, RFL and pickup signals using an oscilloscope. The pickups were located along each of the vanes. Falling of the PKRs, rise of the RFLs and vacuum spikes were observed during the study. These signals can be used for the identification of the BD events. An example of RF signals during BD is shown in Fig. 3.7. The measurements are

performed from the interlock system of the test bench in the electronics room. The pickup signals were not reduced to zero after the BD and some field was kept in the structure. The vacuum system was used to keep the RF structure under UHV below  $1.5 \times 10^{-7}$  mbar. A typical event of discharge was monitored by an increasing in the vacuum pressure up to  $3 \times 10^{-7}$  mbar. The system comes back to normal operation at the next pulse without being affected by the previous discharge.



Figure 3.7: Example of RF pulses during a BD event in the HF-RFQ at the ADAM test facility: FWD (yellow), RFL (pink) and 2 RF pickups (blue, green).

For a better understanding of the BD behaviour, a dedicated DAQ for the HF-RFQ at test bench of ADAM was developed. The DAQ have been implemented in LabVIEW and connected the NI PXIe hardware through Ethernet with the services in the processing tier, i.e. SCADA (OPC UA) and configuration servers (http). Real-time control and monitoring was implemented on a FlexRIO platform with embedded FPGAs to monitor the incoming signals. This DAQ has been written based on an existing software for monitoring signals developed at ADAM. The program records 16 RF (4 Driver FWDs, 4 IOT FWDs, 4 RFLs, 4 PKPs) and vacuum signals.

This Virtual Instrument (VI) provides a user friendly interface for BD identification in a single interface parameter monitoring and data logging. The VI contains two tabs: one for signal “Control and Acquisition”, and another one to specify all the settings and inputs needed by the program. The VI creates a subscription to the Programmable Logic Controller (PLC) using an intermediate OPC (Object Linking and Embedding for Process Control) server. Each time a value in the server changes it is automatically notified to the VI, and it is also updated in the monitor. Calibration constants of each channel are used in operation together with the PLC readings. A picture of the control panel used to monitor the RF signals is given in Fig. 3.8.

Two methods have been implemented in the program in order to improve the accuracy of BDs identification. Both approaches are based on the analysis of the flat top of the RF pulses. The first one determines the average value of the selected part of the signal and compares it with the specified nominal value. If these values are significantly different,

### 3.1. Breakdown measurements in 750 MHz HF-RFQ for hadron therapy applications

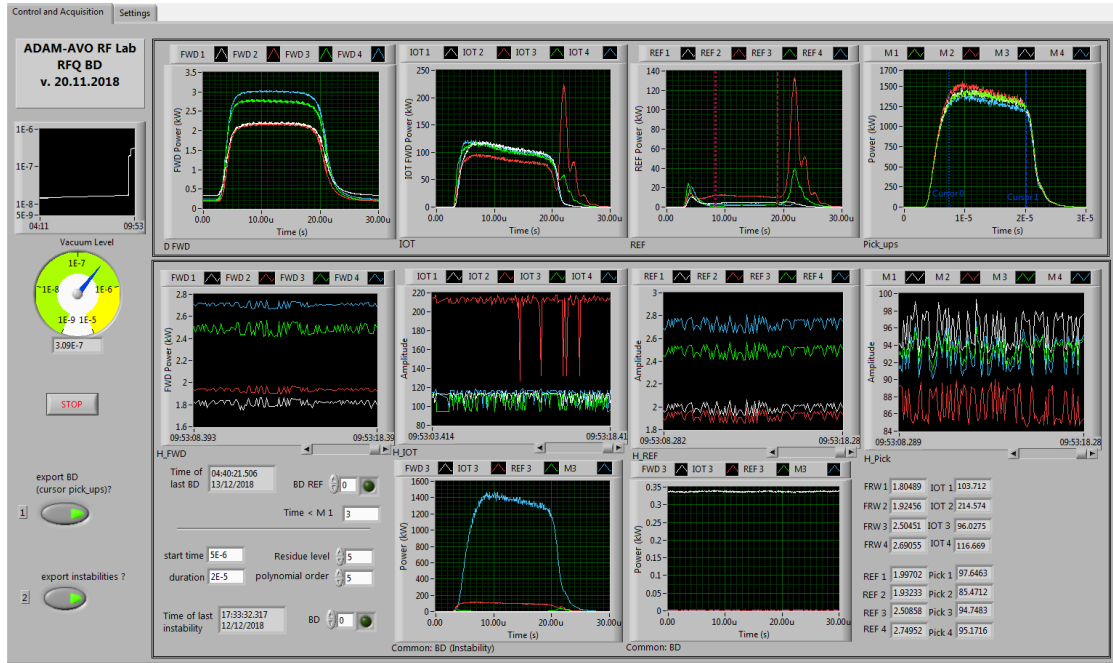


Figure 3.8: Control panel for high power test of the HF-RFQ: RF signals of 4 Driver FWDs, 4 IOT FWDs, 4 RFQ RFLs, 4 RFQ PKPs (top), their average values (middle) and the plot for BDs identification (bottom) with setting parameters.

then the RF pulses are recorded. A segment size of the pulse for calculating the average value have been selected for reasons of convenience. The second method calculates the roughness of the pulse and the deviation from the limit value gives the possibility to detect the unstable pickup signals. The parameters used to set up this analysis are shown in Fig. 3.9. The flat-top of the pulse or subsignal, is filtered by median filter to remove impulse noise and glitches. Then a polynomial data fit is applied and a residual value is calculated to indicate instability that use as trigger to start acquiring record data to the file. The date of each event is added to the filename. All threshold values can be modified from the LabVIEW Front Panel. The manual settings are saved only for the current session. To save data for the next use, the values have to be set in the software with subsequent re-compilation. A more detailed explanation can be found in Appendix B.

This program also allows to impose restrictions on the selected signal for triggering. Depending on the waveform, a more suitable approach can be used. Buttons with LED visualization are applied to select methods and indicate trigger response times. Constant green light on the BD button are used as an indicator of incorrect parameter settings that lead to record unnecessary events. In addition, the time of the last recorded event is displayed on the monitor. The recorded events by the DAQ correspond to the data from the oscilloscope and the vacuum pressure read-out. The main advantage of the DAQ that all 16 RF signals entering the system can be analysed and saved simultaneously. The restrictions given by the Ethernet-cable limit the transmission of digital signals.

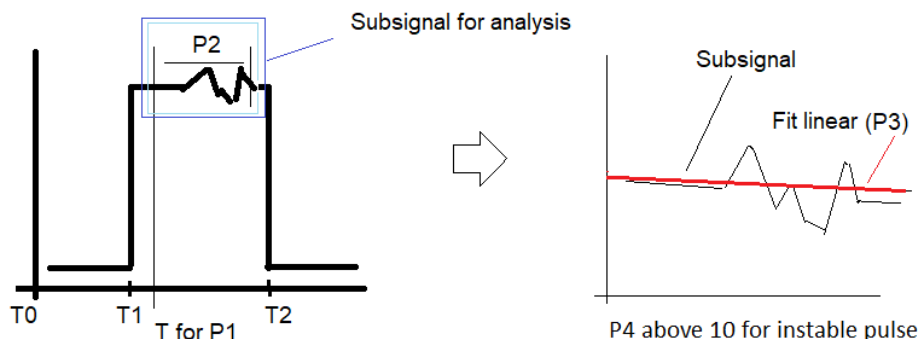


Figure 3.9: Identification parameters to determine flatness of the pickup pulse: [P1] - start time of the subsignal to use for analysis, [P2] - length of the subsignal, [P3] - the order of the polynomial fit and [P4] - residue value accepted.

The test bench operates at the maximum RF power that limits the possibility of increasing BD statistics. At the same time we are limited in flexibility to change any settings and parameters of operation as this RFQ is operated as a beam injector for LIGHT prototype.

### 3.1.4 BD measurements and data analysis

The history plot of the BD events in the HF-RFQ from June 2018 to January 2019 is presented in Fig. 3.10. The total FWD power is 400 kW and the pulse length of signals is 10  $\mu$ s. BD probability is quite low, the measured BDR is about  $1.28 \times 10^{-7}$  bpp, mainly

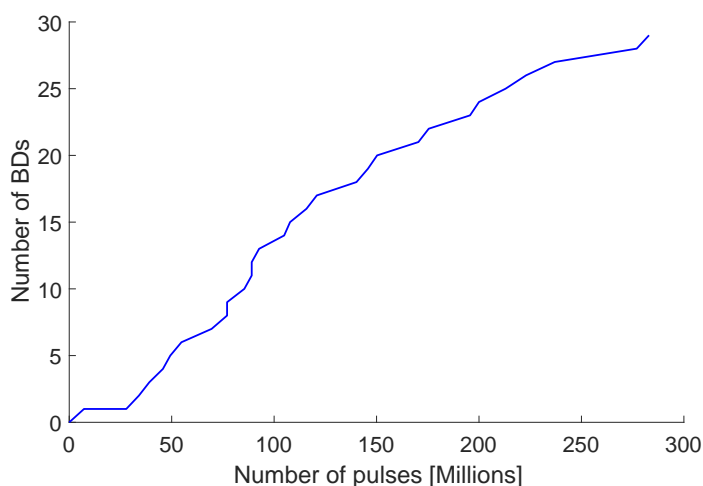


Figure 3.10: Operation history plot of the HF-RFQ at the ADAM test bench: BD number versus the number of pulses. Tests were carried out at the pulses of 400 kW and 10  $\mu$ s.

during restarting the RFQ at full power. This corresponds to less than one BD per day of operation. This value is consistent with the requirements for a medical facility to provide stable operation during treatment.

Additional analysis of each recorded signals has also been carried out for better understanding of the BD behaviour. An example of a BD event is shown in Fig. 3.11. The large rise time of the FWD pulse (about  $3 \mu\text{s}$ ) is due to the need to reduce the RFL signal. A high peak of RFL from the IOT2 is present due to a slight mismatch between a coaxial line and the HF-RFQ. After the BD, the pickup signals exponentially decayed to zero and the REFs have increased significantly following the IOT FWD signal. Note that the normal operation of the HF-RFQ with a proton beam is about  $4 \mu\text{s}$  pulse length.

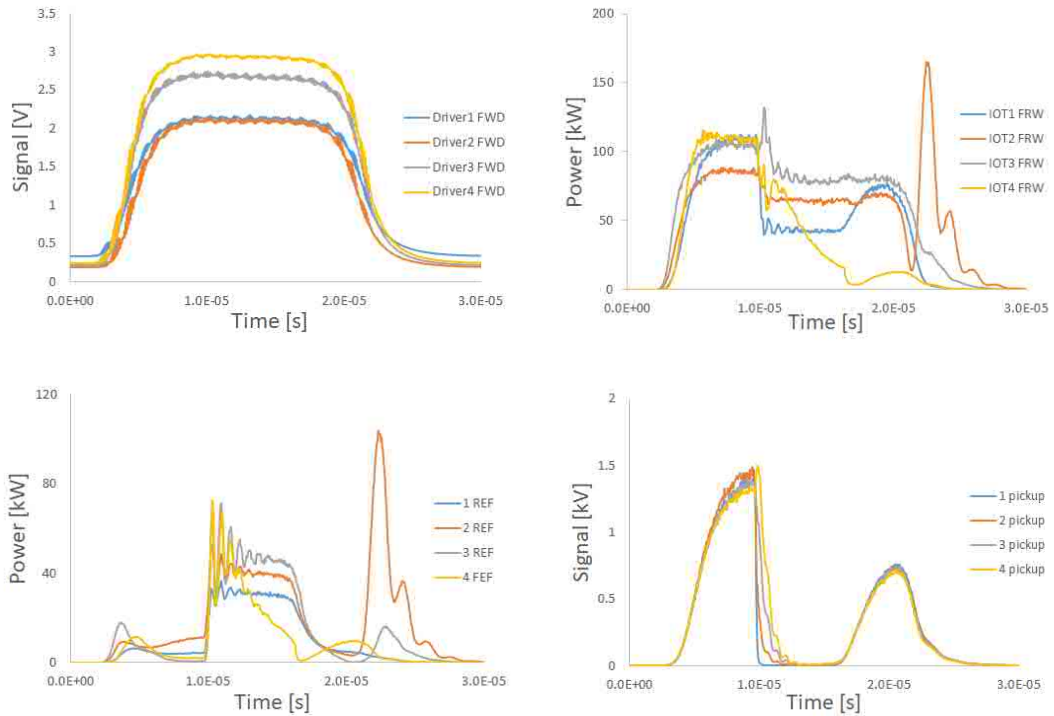


Figure 3.11: RF signals from the HF-RFQ at a BD event: Drive FWDs, IOT FWDs, REFs and pickups respectively.

The signals measured by pickups during BDs have a different behaviour. An example of such signal from two pickups located along one vane is presented in Fig. 3.12. The field rapidly decreases after the BD, but remains at some value for some time and it has a different magnitude depending on the position of the pickups. This information can be used to determine the location of BDs in the RFQ. In this example, it was suggested that the BD occurred in the area near pickup 4.

An initial understanding of the BD localization is carried out based on available RF signals from the HG-RFQ at the ADAM test facility. The waveform data shown in the example presented in Fig. 3.11 were taken with an oscilloscope that started ( $t=0$ ) after the

BD. The field is rapidly going to zero at the pickup 1, while the field measured by other pickups decays at a slower rate. This indicates that the BD occurred at the beginning of the structure, corresponding to the low beam energy part. The problem of determining the location of BDs become more complicated when they occur in the middle of the structure as the HF-RFQ is filled up by 4 ports. After the BD, the structure continues to be filled from some power coupler and the reflected wave affects the incoming signals.

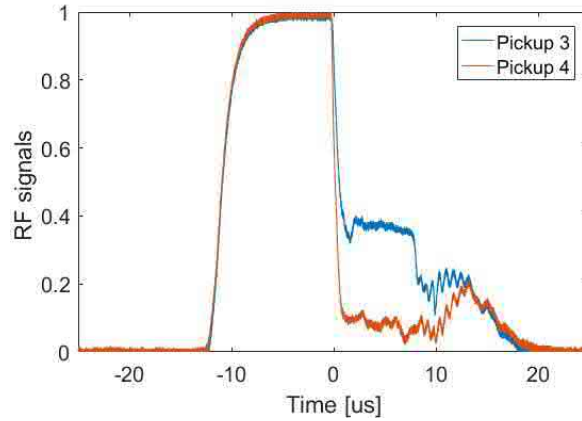


Figure 3.12: Normalized RF signals measurement by pickups during BD event.

The HF-RFQ is not equipped with a diagnostics setup that supports the measurements of all required signals to determine the location of BDs. But still, based on this study, we can conclude that the BD occurs along the structure, with a predominant amount in the central part.

To complete the analysis of the BD, the Q-factor and the dark current have been measured respectively. The Q-factor due to losses in copper is about 6500 according to 3D RF design simulations. The measurements of an effective Q for the four power couplers yield demonstrate a slight over-coupling of 3 % on average [95]. The purpose of these experiments is to see how the Q-factor is affected by the BD.

As shown in Fig. 3.13, this value significantly changed during the discharge of the cavity. The rise time method (time domain) for evaluating attenuation through the quality factor Q is used. The rise time defined as the time difference between the 90 % and the 10 % amplitude levels of the first peak pulse arrival. The difference between the two definitions is insignificant (deviation of about 5-10 %). When the RF pulse is turned off, the decay of the pulse is about  $0.85 \mu s$  for pickups 1, that correspond to 1880 of loaded Q-factor. Thus, attenuation is decreased by 3.5 times. For pickup 2 - 4, the Q-factor is about 4500. In this case, the undesired RFL power gives impact on the FWD power. Deriving the Q-factor at the BD event is also limited by the FWD/RFL power calibration. The HF-RFQ calibration has been performed during a standard S-parameter measurements. The measured FWD and RFL power always deviates from the real powers that goes into and is reflected from the cavity. This is due to RFL in the waveguide, the cables, the directivity and the coupling factor [96]. Their impact increases during BDs.

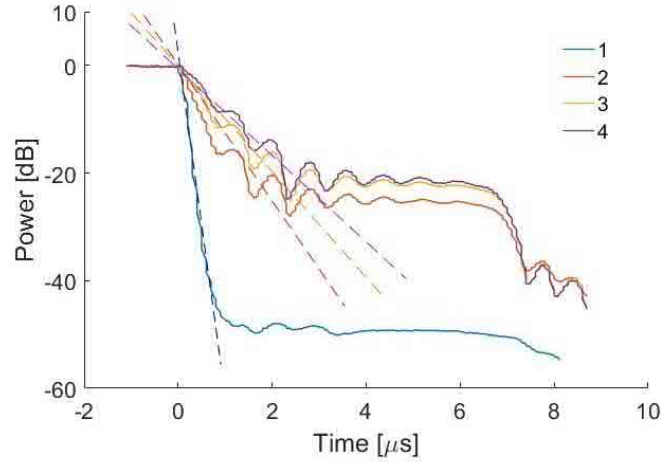


Figure 3.13: Normalized power on the falling edge of the pickups located along the RFQ at the BD event.

The operation of an AS is generally limited by BDs caused by high surface electric fields present on vanes in case of the RFQ. The high fields reached during the tests lead to high levels of field-emitted current or dark current (DC). DC can cause RF energy absorption and additional radiation that is generated by the AS.

A first approach to observe DC from the HF-RFQ has been performed. At the beginning we tried to use the existing current detectors located on the beam line. The measurement starts with use of the existing Beam Current Transformer (BCT) and Average Current Detector (ACD) that are located at the downstream position. The ACD is derived by summing the four electrodes of a BPM and it selects only 750 MHz contributions. Both detectors show the results on the noise level. The ACD is limited to approximately  $1 \mu\text{A}$  current sensitivity. This means that electrons don't go outside of the structure or their number is very small.

According to the method proposed [97], the DC level can be measured by monitoring the cavity voltage for different RF input levels. At normal operation, the nominal power  $P$  is proportional to the voltage  $V$  squared, the coefficient being the inverse of the shunt impedance (from Eq. (1.6)). The nominal vane voltage given by the beam dynamics simulations is used to calculate the corresponding nominal power  $P$ . Once this power is going into the cavity, the FRW IOT signals are recorded as the nominal RFQ level. This is the voltage on a monitoring loop inside the cavity, detected and processed in the RF chain, and proportional to the vane voltage. DC appears at high voltages and the electrons are accelerated over the cavity gaps and extract an additional power  $P = I \times V$  from the generator. When plotting  $P$  vs.  $V^2$ , the deviation from a straight line at high power gives the power driving the DC. Figure 3.14 shows the measured input power as a function of the cavity voltage for the nominal pulse length of  $10 \mu\text{s}$ . In this case, the DC is not detected. This can be explained by the fact that the nominal power (400 kW)

is not enough for a significant emission of electrons. Moreover, such a deviation from the straight line indicates that the IOTs was saturated after 330 kW at the moment of the measurement.

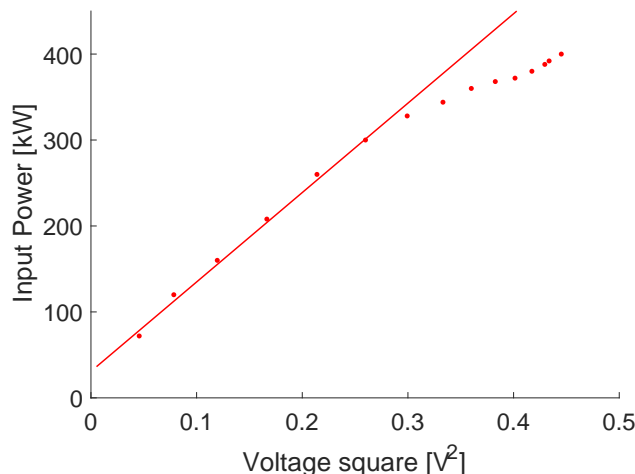


Figure 3.14: Input Power vs. vane voltage square for the HF-RFQ at the ADAM test facility.

In summary we can conclude that this setup is not ideal to perform the study of BDs but we have obtained the confirmation that this HF-RFQ is very well suited for applications with demanding HG requirements. For better understanding of the BD behaviour and identifying the main parameter limits, the test have to be performed in a dedicated set-up as we have described for a S-band structure in previous Chapter 2.

## 3.2 Breakdown measurements in 352.2 MHz Linac4 RFQ

The RFQs are one of the initial component of accelerator chains. The Linac4 RFQ is part of the injector complex of the Large Hadron Collider (LHC). The HG performance and BD behaviour of this element is crucial aspect of this study.

### 3.2.1 Description of Linac4 and 352.2 MHz Linac4 RFQ

The Linac4 is a NC linear accelerator [98], intended to replace Linac2 as injector of the Proton Synchrotron Booster (PSB) belonging to LHC injector chain. The replacement is being performed during the long shutdown for 2019 - 2020. Linac4 accelerates negative hydrogen ions ( $H^-$ ), consisting of a hydrogen atom with two electrons. The increase of energy from 50 MeV (Linac2) to 160 MeV (Linac4) allows to overcome the space charge limitations at the PSB injection. The new linac can increases the beam brightness out of the PSB by a factor of 2, making possible an upgrade of the injectors for higher intensity and eventually an increase of the LHC luminosity [99].

Linac4 is located in an underground tunnel connected to the PSB transfer line to PSB. A surface building houses the RF equipment, the power supplies, the electronics and other infrastructures. A schematic layout is presented in Fig. 3.15. The location of Linac4 is connected to the existing accelerator infrastructure by a transfer line equipped with debunching and collimation sections.

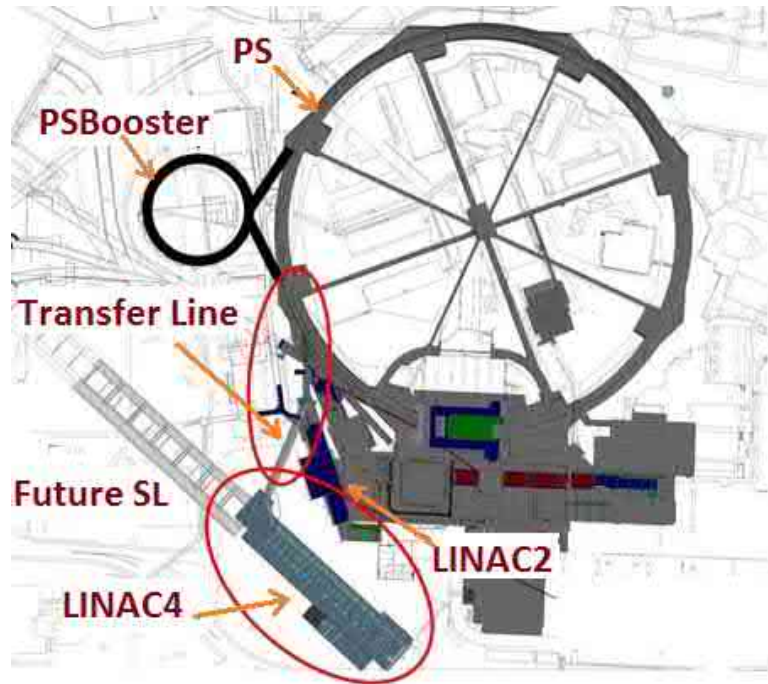


Figure 3.15: A schematic view of the connection between the Linac4 and the PS ring. The light grey colour of construction at the end of Linac4 indicates a possible extension called Superconducting Proton Linac (SPL) [100].

The  $H^-$  ions leave the ion source with an energy of 45 keV and travel along 86 m line of RFQ, chopping line, DTL, CCDTL and Pi-mode structure (PIMS) that accelerate beams to the final energy. The overall architecture of Linac4 is shown in Fig. 3.16. The main Linac4 parameters are based on the requirements for the PSB injection and the LHC respectively, and other experiments such as ISOLDE [101]. The operating frequency of Linac4 (352.2 MHz) is defined by the availability of klystrons, circulators and waveguides from the LEP RF system (Large Electron Positron Collider). This frequency is suited for a linear accelerator because it provides a good correlation between the simplified design tolerances at low frequency and the high gradients and efficiencies allowed by higher frequencies. The total number of RF chains is initially 21 at 352 MHz frequency: 1 RFQ, 3 Buncher cavities, 3 DTL, 7 CCDTL, 6 PIMS and 1 Debuncher.

Considering the limits of the source technology and the RF requirements, the Linac4 machine will pulse at a 1.2 Hz repetition rate, with up to 0.6 ms beam pulse length and up to 40 mA current. All structures have been build for the SPL duty cycle of up to 5%.

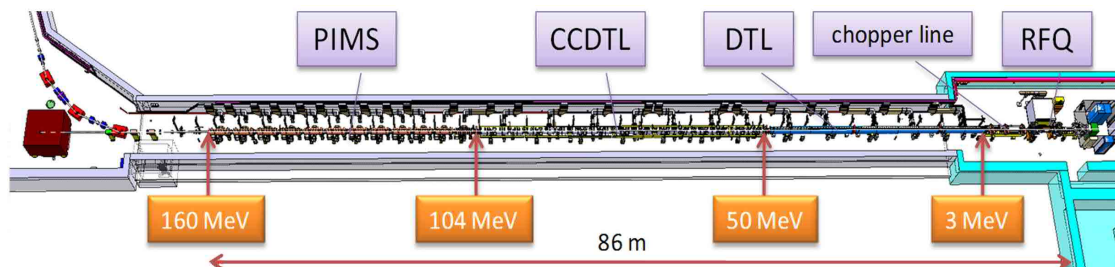


Figure 3.16: Scheme of Linac4.

The low-energy front end of Linac4 is based on a 352 MHz, 3 m long Linac4 RFQ [102]. The RFQ is designed to accelerate a 45 keV, 70 mA,  $H^-$  beam from the ion source to the energy of 3 MeV, with an efficiency of 95 % while preserving the transverse emittance. The RFQ is a 4-vane structure consisting of three modules of 1 m length with one power coupler. The electrical length is  $3.5 \lambda$  allowing the direct coupling of the three RFQ sections without using coupling cells between sections. The result of this design is a compact RFQ with an intra-vane voltage of 78 kV and a peak surface field of 34 MV/m. The Linac4 RFQ is operated at low duty cycle (0.1 %) when used as injector to the PS booster, but its design is compatible with higher duty cycle (10 %) for a possible high-intensity upgrade of the CERN linac facility [103]. The RF operational parameters of the RFQ are summarized in Table 3.3.

Table 3.3: Main parameters of the Linac4 RFQ.

Parameter	Value
Frequency	352.2 [MHz]
Length	3.06 [m]
Vane voltage	78.27 [kV]
Peak RF power	600 [kW]
Beam Input energy	45 [keV]
Beam Output energy	3 [MeV]
Coupling coefficient	1.593
Quality factory	6800

The decision to design this RFQ, as part of the injection system for Linac4, came after the chopper line elements had already been procured and assembly plans made. The initial plan was to use the RFQ developed and built by CEA and IN2P3, for the IPHI project [104]. However finally, in order to get better beam performance, CERN decided to redesign this structure. The new design has been developed in the way that the output beam parameters of the RFQ were compatible with the existing chopper line. The results of the redesign is a compact RFQ of 3 m vs 6 m of IPHI. The design of a short RFQ has helped in minimizing the RF power requirements from one klystron. A general view of RF design is presented in Fig. 3.17.

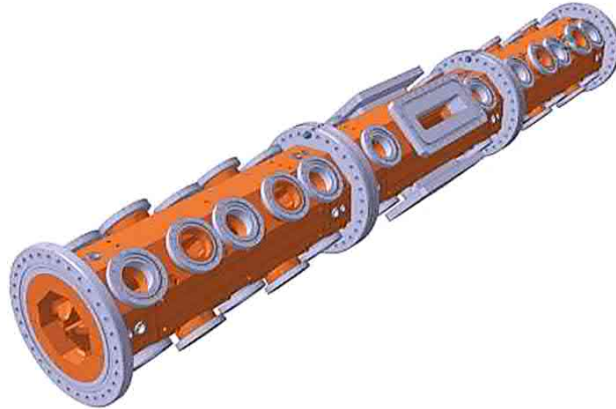


Figure 3.17: Linac4 RFQ with the characteristic 4-vane structure.

The Linac4 RFQ has been designed in collaboration with CEA/IRFU in 2008 - 2009 and fabricated at the CERN workshop, the assembly and RF tests were performed in 2013. The precise fabrication has allowed achieving a field flatness of 1 %. The high-power conditioning to the nominal power of 390 kW has been performed successfully. The RFQ has been commissioned in the tunnel with beam in October 2013. The RF chain of the RFQ consist of a LEP-type klystron feeding the structure via a circulator-waveguide system. The maximum RF power generated by the klystron is 1.3 MW. The RFQ at first phase of beam commissioning is shown in Fig. 3.18.

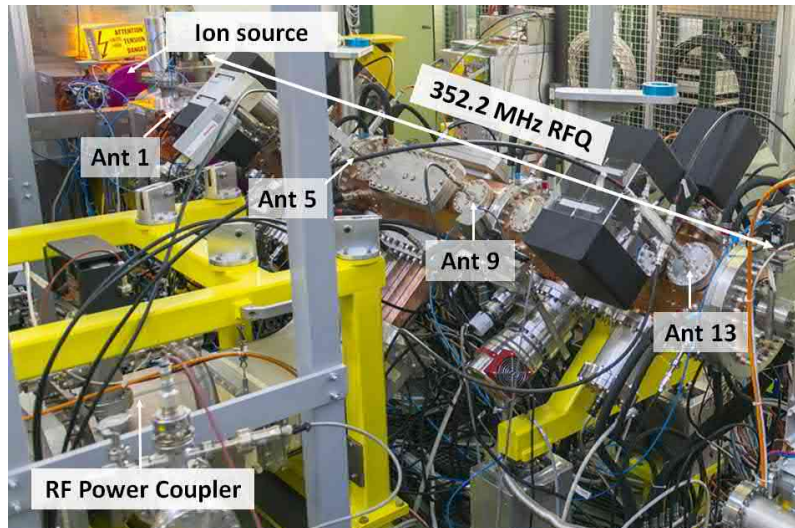


Figure 3.18: Linac4 RFQ at first commissioning phase.

The beam dynamics of the HF-RFQ have been carefully optimized to have minimum emittance growth at maximum transmission. Beam transmission was measured by a BCT

and a Beam Position Monitor (BPM) located upstream and downstream of the RFQ. The measured value is about 75 % at nominal RFQ settings (equivalent applied RF power of 390 kW at standard pressure of  $5 \times 10^{-8}$  mbar), showing good agreement between measurements and simulations. To improve the beam transition, the RF cavity voltage and, accordingly, the gradient has been increased.

The electromagnetic fields inside the RFQ cavity are monitored during operation thanks to pickup loops located on tuner axes. All signals are calibrated. To keep the field constant, temperature regulation is used. The dynamic tuning strategy is based on two cooling circuits: vanes and body water channels. Dynamic tuning of the RFQ cavity is obtained by regulating the difference in water temperature between the two circuits [102].

### 3.2.2 Update of the data acquisition system of Linac4 RFQ

The LLRF system of the RFQ consists of an I/Q feedback loop to control the magnitude and phase of the pulse, and a tuning loop to control the resonance frequency of the RFQ. An RF feedback keeps the accelerating voltage at the desired value in the presence of transient beam loading. The closed-loop delay is around 1.2  $\mu$ s, that includes generator and circulator group delay, waveguide to cavity, and cable delay in the antenna signal path and time for processing in the LLRF.

The control system interface uses the same standard hardware and software components as in the LHC LLRF. The software running in the CPU uses the CERN Front-End Software Architecture (FESA) framework [105]. FESA allows real-time synchronisation of program actions and control with timing events from the various accelerator's equipment. Important data is logged into two sets of memory: the measurement database (MDB) where it remains for 3 months, and the logging database (LDB) for long-term storage. The system can be monitored by an operator during operation, and all adjustments can be done remotely. The TIMBER application (LHC Data Storage) [106] allows grouping and plotting of data on multiple Y-axes according to their units.

The RF signals are controlled by the LLRF: the cavity field probed by an antenna, the klystron output forward power measured by a directional coupler between the klystron and circulator, and the FWD and RFL powers at the module input measured on the waveguide before the main input coupler. Directional couplers allow the measurement of forward and reflected power from the cavity by coupling a small amount of power of less than 0.1 dB. The coupling coefficient is essentially determined by the ratio of the reflected to forward power in steady-state regime. The RF is switched on 100  $\mu$ s before injection. The filling ramp raises the cavity voltage in 50  $\mu$ s. At that time the RF feedback is closed resulting in a small visible transient. Fig. 3.19 shows the antennas and reflected signal of the Linac4 RFQ, without beam, with 3.2 MV demanded voltage. The initial settings of the common DAQ allow to record the average value of the signal relating to the Linac4 RFQ.

The vacuum signals are constantly monitored at different sections of the Linac4 RFQ. Additional vacuum pump and pressure gauges to control the residual gas coming from the source are used. The vacuum level of the RFQ is maintained in the range of  $10^{-8}$  mbar.



Figure 3.19: The real-time signals measured from Linac4 RFQ and visualized at Front-End Software Architecture (FESA).

A schematic connection of the pumping systems is shown in Fig. 3.20. All signals are controlled by an interlocking system. During a BD event, a vacuum spike appears, the values of the vacuum parameters change by one order of magnitude. This does not cause a system shutdown, because the vacuum is calculated as the average value for a certain period of time.

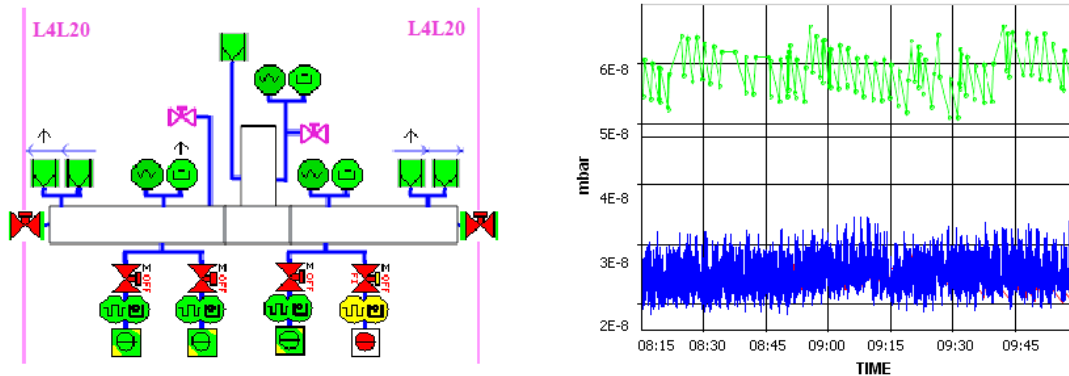


Figure 3.20: Vacuum readers in the Linac4 RFQ.

The DAQ for BD detection was based on an already existing system developed by the CERN LLRF group for test and conditioning of the Linac4 RFQ. This system allows to measure 16 pickups signals connected via coaxial cables and processes using NI PXI-6133. The graphical user interface is based on LabVIEW software. The acquisition system delivers samples proportional to the RF amplitude at pickups outputs. A schematic layout of signal connections are shown in Fig. 3.21.

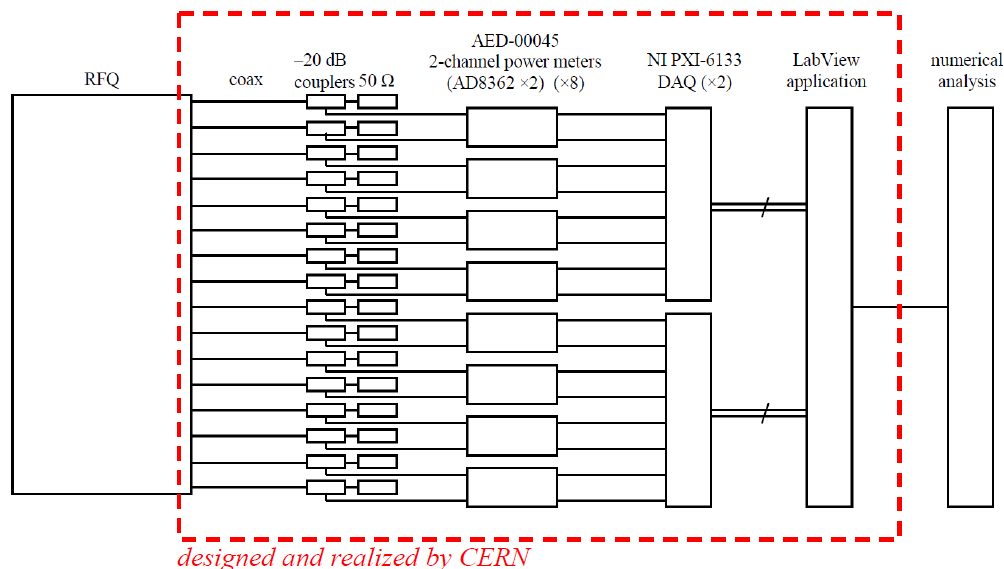


Figure 3.21: Physical and Acquisition layers of LLRF system for the Linac4 RFQ.

This system is able to calculate the maximum and the minimum values, the rise time and the fall time, the width at 50 % and 90 %, the root mean square (RMS), and the integral of a given value at a chosen point and instability of the pulses. To detect an instability, a selected part of the signal can be analysed by filtering and fitting a polynomial to the signal. If the area of the pulse is flat, the residue of the fit should be small (noise level). The results above the noise level is due to detected instability. This principle can be used for BD identification. During a BD event, there is a drop in the voltage of the signals from the antennas measured by the DAQ of the RFQ, and also a greater REF detected via TIMBER. These systems are not synchronized. This should be taken into account in subsequent analysis. The software is constantly visualizing all 16 signals from pickups and their average value. For more convenient data reading, these values are displayed near each pickups on a schematic picture as shown in Fig. 3.22.

The parameters are setted depending on the stability of the signal and its pulse length. Pickups are calibrated upon assuming that Linac4 RFQ voltage at low RF power (in the kW range) is identical to voltage derived from bead-pull measurements, otherwise an additional coefficient is affected to each pickup channel. According to the numbering given to each antenna, antennas 1 to 4 are located in the first plane in clockwise from the ion source. The rest are located in a similar manner with subsequent planes. Following this, the antennas 1, 5, 9 and 13 are located along the same vane 1, and the power coupler is between the antennas 5 and 9.

In order to perform the BD studies, some changes have been made in the existing DAQs. As part of the work of this thesis, the update of DAQ for Linac4 RFQ has been made. Some details of LabVIEW changes are shown in Appendix C. The ability to save the signal from the pickups during BDs has been added to the software related to the

RFQ. Thus, we record the signals only during BDs and the average value of signals for each regular pulse to follow the history of changes in parameters over time. The INC and REF signals from DC of each pulse are saved via the DAQ of LHC to LDB. Through the FESA class we get an array of 2063 points that correspond to the length of the pulse before the RF is turned off. Therefore the attenuation slope is not recorded to TIMBER.

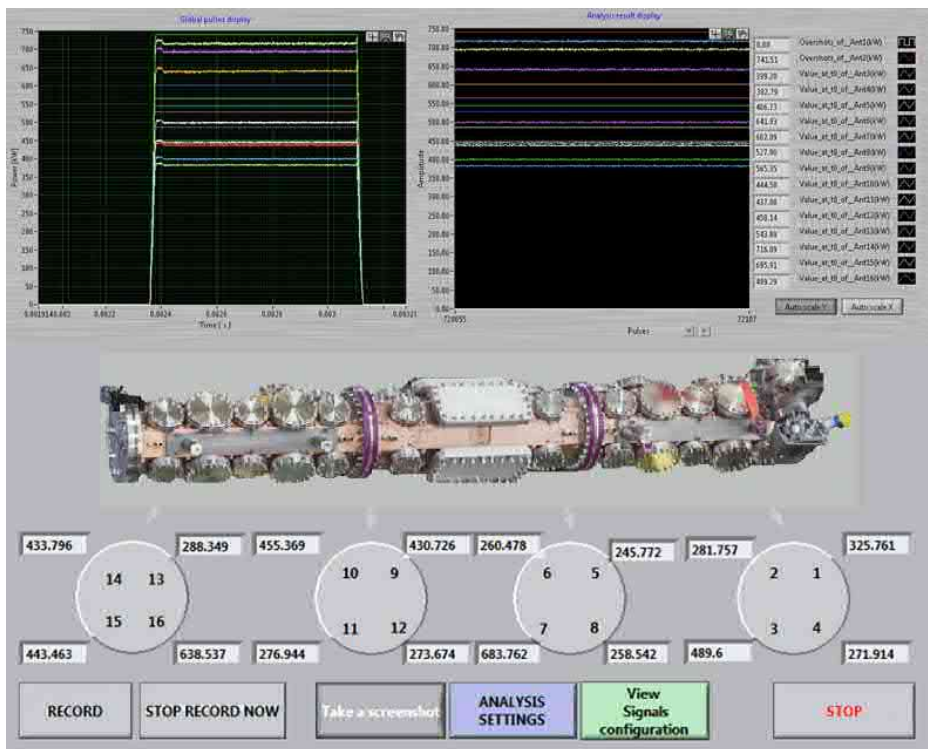


Figure 3.22: LabVIEW’s VI front panel of the automatic reading pickups signal in the Linac4 RFQ.

### 3.2.3 Linac4 RFQ breakdown measurement and data analysis

The BD studies in the Linac4 RFQ have been performed during two experimental periods. The first one, from September until mid-December 2018, was aimed to understand the BDs in the RFQ and the identification of the BD location, and the second, from March 18 to April 18, 2019, was focused on obtaining more detailed information about the BDs and the behaviour of the structure at higher power operation. The history plot of the first measurement of the BDs in the Linac4 RFQ are presented in Fig. 3.23. The operation was performed mainly with beam at FRW power of 480 kW and 1.2 Hz repetition rate. The data have been collected also without impacting the normal operation regime. A non linearly increasing number of BDs versus number of pulses indicates the appearance of BD clusters. This can adversely affect the structure. The high BD activity could be caused by external factors. Since at the time of measurements, the system parameter settings and

beam debugging have been made. A particularly large number of BDs occurred when the pulse length was changed. This indicates the need of implementing a conditioning algorithm, which ensures the target BDR and the vacuum level to maintain a safe operation. Such mechanism gives the possibility to increase the pulse length to higher levels. The measured BDR was  $3.85 \times 10^{-5}$  bpp for  $700 \mu\text{s}$  and  $6.22 \times 10^{-5}$  bpp for  $900 \mu\text{s}$ . In order to reduce the number of BDs, it was decided to return to the previous pulse length for stabilization of the BD activity.

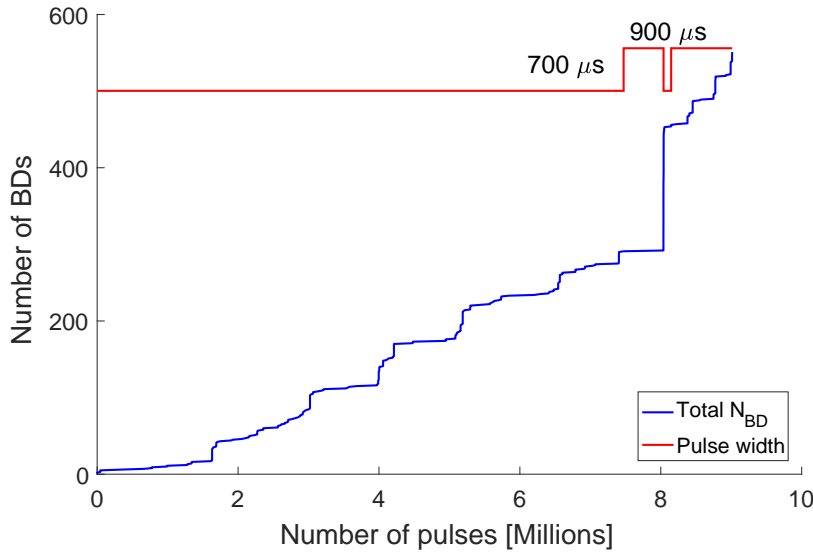


Figure 3.23: Operation history plot of the Linac4 RFQ: BD number versus the number of pulses at different pulse lengths are indicated on top.

The typical regular and during BD RF pulses measured by an oscilloscope at operation without beam are shown in Fig. 3.24. The values are normalized to the mean FWD. The RFL signal carries a contribution to the increasing FWD during the BD. This can be the main cause of subsequent BDs. The RFL has a jump in power at the beginning and the end of the pulse. This is because the rise and the fall time of the signal are longer than the filling time, which is associated with the need to reduce the REF for klystron protection. And furthermore, the Linac4 RFQ is overcoupled according to design, the INC power is reflected back through the coupler.

During a BD event, there is a drop in the voltage of the signals from the antennas, and an increase of REF signal. The moment of BD, namely when the antenna signal drops to half the initial amplitude, has been analysed. The left part of Fig. 3.25 shows that during the first month of the test the BDs occurrence when beam presents in the structure. The pulse length of RF signals was  $700 \mu\text{s}$  and the bunch length was  $400 \mu\text{s}$ , that entered structure after  $250 \mu\text{s}$ . The planned updating work has been carried out which allow to increase the power capabilities. After this, the dominant number of BDs occurs at the beginning of the pulse after full filling of the structure and are affected by

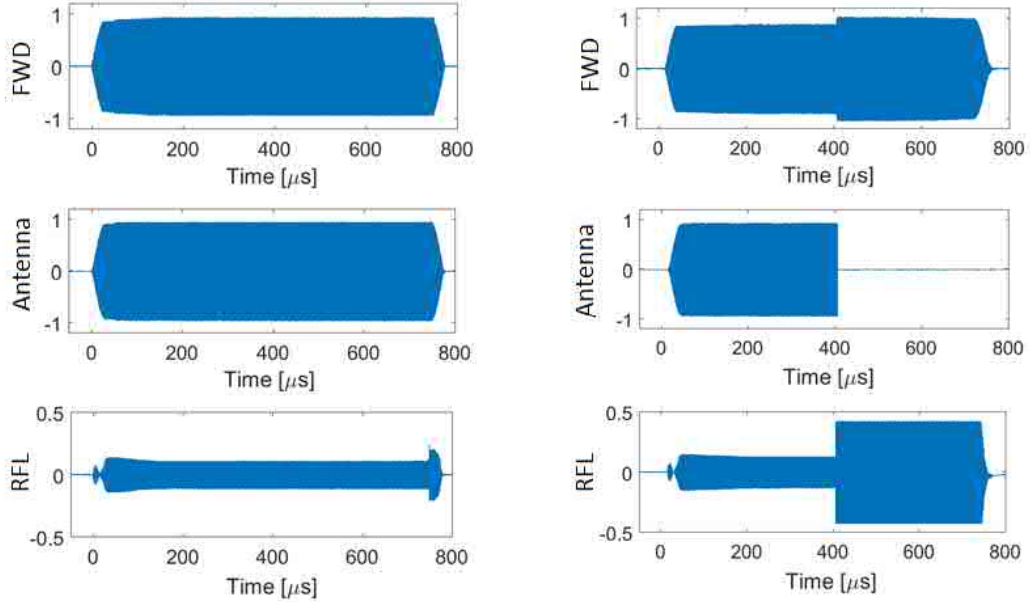


Figure 3.24: Regular (left) and BD (right) RF pulses from the Linac4 RFQ: FWD, signal from antennas and RFL.

closing the feedback loop. The beam passes the structure immediately after feeding of the RF power, that causes an overshoot in the power. The effect of the beam on the FWD and RFL signals are presented in Fig. 3.26. A power increase of 7 % is observed in the presence of the beam. This increase depends on the actual beam length. The slight excess at the beginning of the pulses was due to LLRF settings. According to the result (see Fig. 3.25 (right)), the most BDs occur during operation with beam in the first 50  $\mu\text{s}$ .

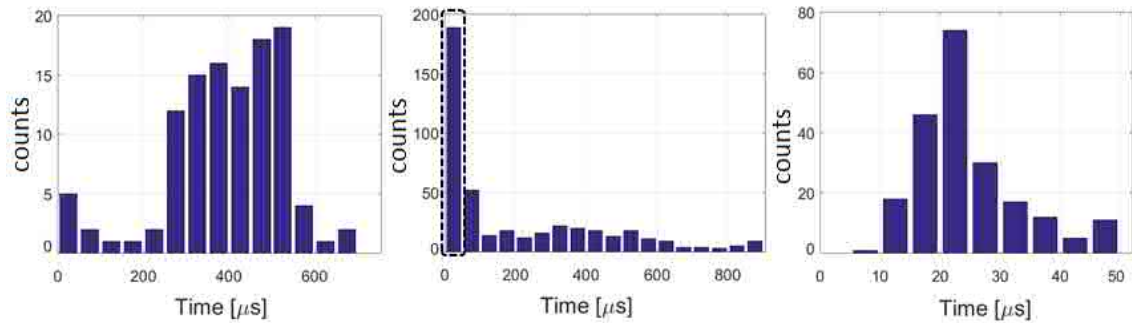


Figure 3.25: BD positioning in the pulse for Linac4 RFQ with beam: at the first stage of conditioning (left), after the update of LLRF and HPRF (middle) and zoom of the first histogram area from middle plot (right).

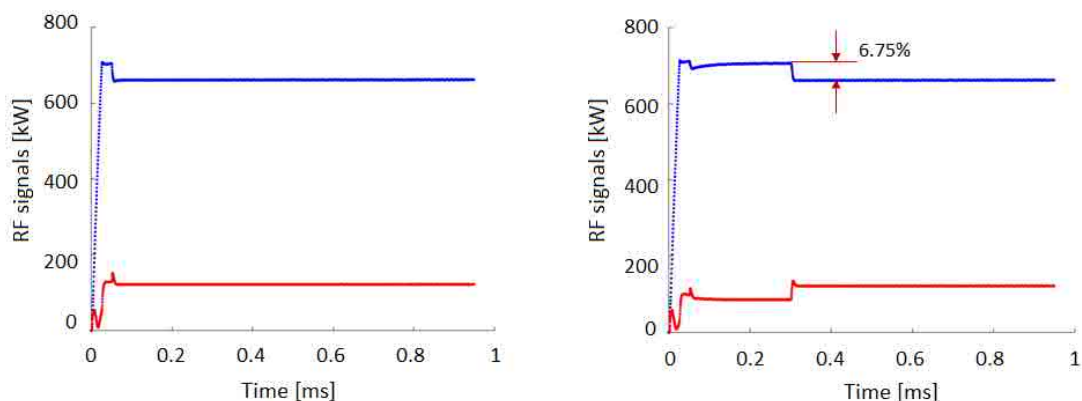


Figure 3.26: FWD and RFL signals of the regular pulse without beam (left) and with beam (right) in the Linac4 RFQ.

As a complement to the BD studies, the measurements of the quality factor has also been performed in the Linac4 RFQ. The stored energy was measured with the pickups. A dramatic decrease of the quality factor during the BD is observed, the decay time of the stored energy varied from event to event. For regular pulses the quality factor is 6880, but in case of a BD event the value was reduced to 2650 as shown in Fig. 3.27, where we can observe that all pickups have similar decay with some small oscillation at the end of pulse. The decay of the stored energy took about  $5 \mu\text{s}$  to decrease by 20 dB. In general, the quality factor of the structure during BD has been elevated in the range from 2800 to 5700, that are twice smaller compared to normal operating regime. The DAQ of the RFQ has a limitation in the resolution of registered signals. Therefore this cannot be used to identify the BD location.

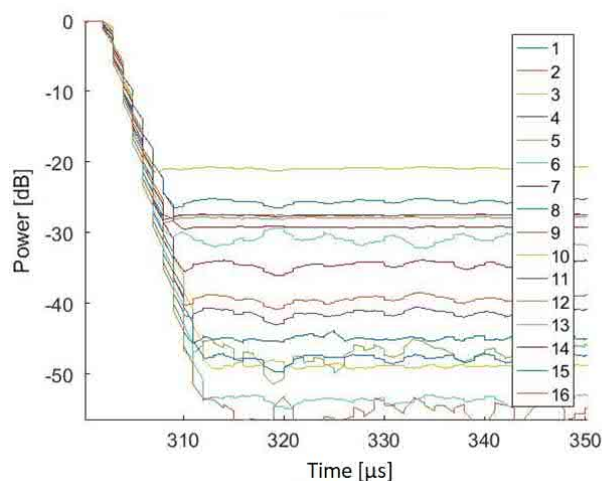


Figure 3.27: Decay measurement with the RF pickups in the RFQ Linac4 at BD event.

A large variation of the stored energy in the decay rate was observed in the cavity after the input power have been tuned off. The signals measured by the antennas in different areas of the structure during BD have different behaviour. For instance the majority go to zero, but some of them record the residual value and much lower RF power continues to enter the structure. In the following, we will consider two common behaviours of the signals from the antennas. The first example is shown in Fig. 3.28. The amplitude of the signals are normalized to maximum values for better comparison. The signals from antennas 13 - 16, that are located at the same transverse section at the end of the structure, drop to zero after the BD. Some antennas still measure a certain value, moreover, the maximum values are at the beginning of the structure, followed by an attenuation. When a BD occurs, the cavity is divided in two sections: the power continues to flow into the section with the coupler, and the other section is blocked. Based on these assumptions, we can conclude that the BD occurred at the end of the structure for this example. About 60 % of BD events have similar signal behaviour, that can be caused by the high-energy of the beam.

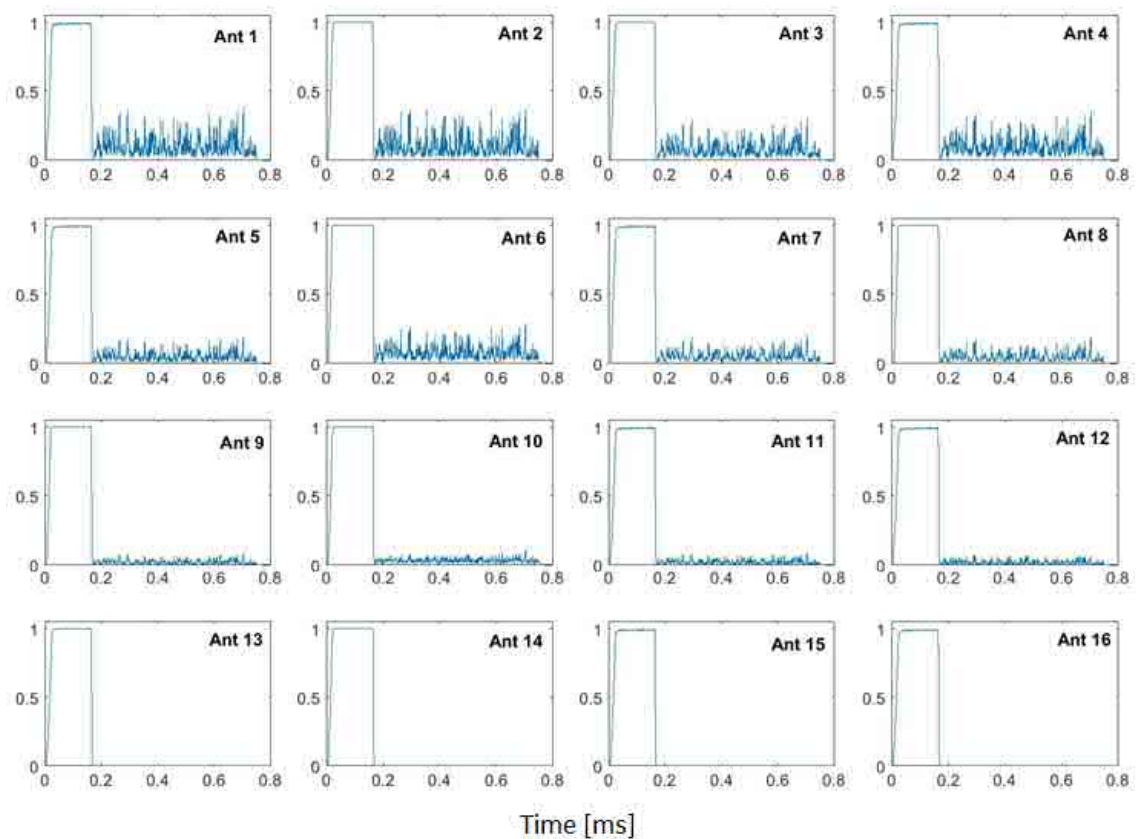


Figure 3.28: Antenna signals during a BD in the Linac4 RFQ: 60 % of all events have similar behaviour.

Another example of a BD event is shown in Fig. 3.29. A BD event like this occurs in 20 % of the cases. Antennas 3, 5, 9 and 15 drop to zero, antennas 1, 7, 11 and 13 keep very small value, and the rest of the antennas that are located along the vane 2 and 4 measure constantly present voltage. Based on this, we can assume that the BD occurs in the middle of the structure, namely in the area between antennas 5 and 9, and this affects all the length of vanes 1 and 3. Notice that the power coupler is located between 5 and 9. A small mismatch in the power flow, that feeds the RFQ, can lead to high surface field that causes the BD. This area requires careful supervision as damage of the surface of this area can have an impact on the reflection coefficient of the coupler.

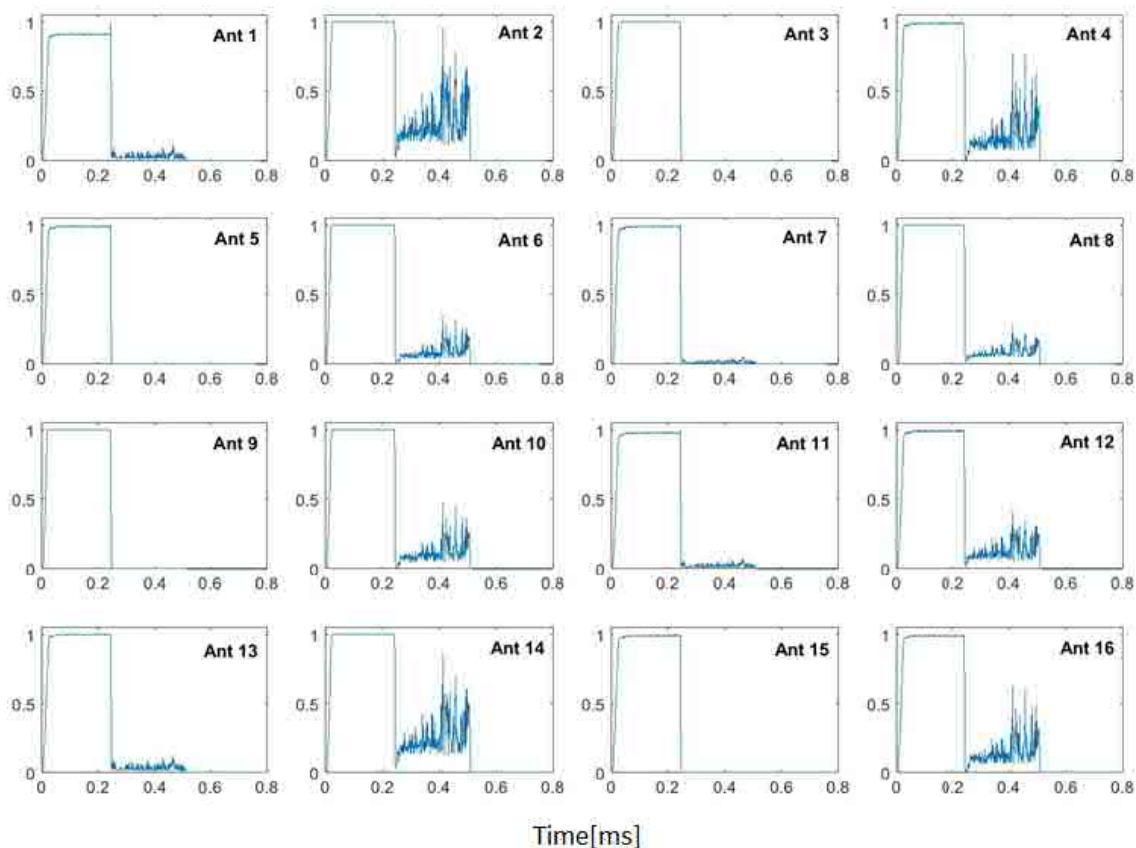


Figure 3.29: Antenna signals during a BD in the Linac4 RFQ: 20 % of all events have similar behaviour

According to the preliminary review of BDs location, the main number of BDs, about 60 %, were at the end, 20 % - in the middle, 10 % - at the beginning of the structure, and 10 % are difficult to determine.

A study of the cavity modes of the decay spectra for various pickups in the Linac4 RFQ have been performed. Measurements of the probe power for the regular pulse and

BD event are shown in Fig. 3.30. The Fourier Transform (FT) of the probe power has been applied in the downstream section after power-off. The frequency of the regular pulse corresponds to the design parameter of 352.2 MHz, other frequencies appear during BD. The values depend on the section of BD location. To explore this phenomenon in detail, more dedicated measurements are required.

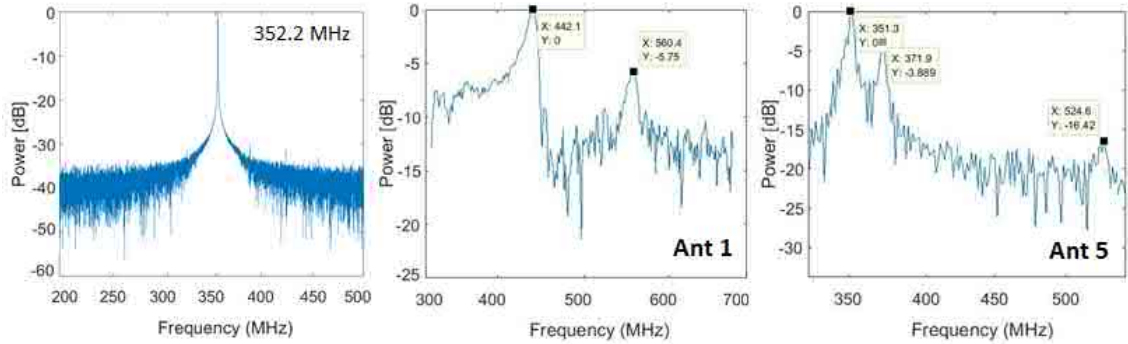


Figure 3.30: Frequency domain study of BDs in the Linac4 RFQ.

During second period, a more detailed study of the BDs was continued. The Linac4 RFQ has been operated with different powers at 900  $\mu$ s pulse length. The history plots of the operation with and without beam are presented in Fig. 3.31. The high BD activity in the test without beam can be explained by the fact that the structure was not conditioned with such high power before. The maximum power of the previous test was 440 kW at 900  $\mu$ s. The BDR dependence on gradient demonstrates  $E^{25.5}$  and  $E^{40}$  with and without beam accordingly as shown in the bottom part of Fig. 3.31. However, the BDR dependence on the pulse length has not been taken into account. These results are close to the established law for CLIC prototypes, where  $BDR \propto E^{30} \tau^5$ . This allows to determine the BD probability for certain forward power. For example for 440 kW unloaded forward power:  $BDR = 1.4 \times 10^{-5}$  bpp and loaded case:  $BDR = 7.1 \times 10^{-5}$  bpp.

The measurements taken in the first phase of the testing period show that frequency information can be useful for the study of BD locations. Therefore the DAQ requires further changes. The easiest solution was to split the signals read from antennas to the existing system, that continuously monitors the power on the vane of the Linac4 RFQ, and to the ‘oscilloscope readers’. Four oscilloscopes were connected to the front panel of the Linac4 RFQ pick-up acquisition matrix (crate) as shown in Fig. 3.32. The connection was performed to the -20 dB output with 50  $\Omega$  attenuation on the oscilloscopes. These devices have been set to identify BDs and to record them to external memory cards. The ratio between the resolution of detected signals and speed signal processing was determined to have precise measurement of the frequency. This measurement allows to observe changes of the field along the structures.

The analysis of the field in the Linac4 RFQ measured by the antennas located in one plate (transverse section) shows that new frequencies appear during a BDs. The Fig. 3.33

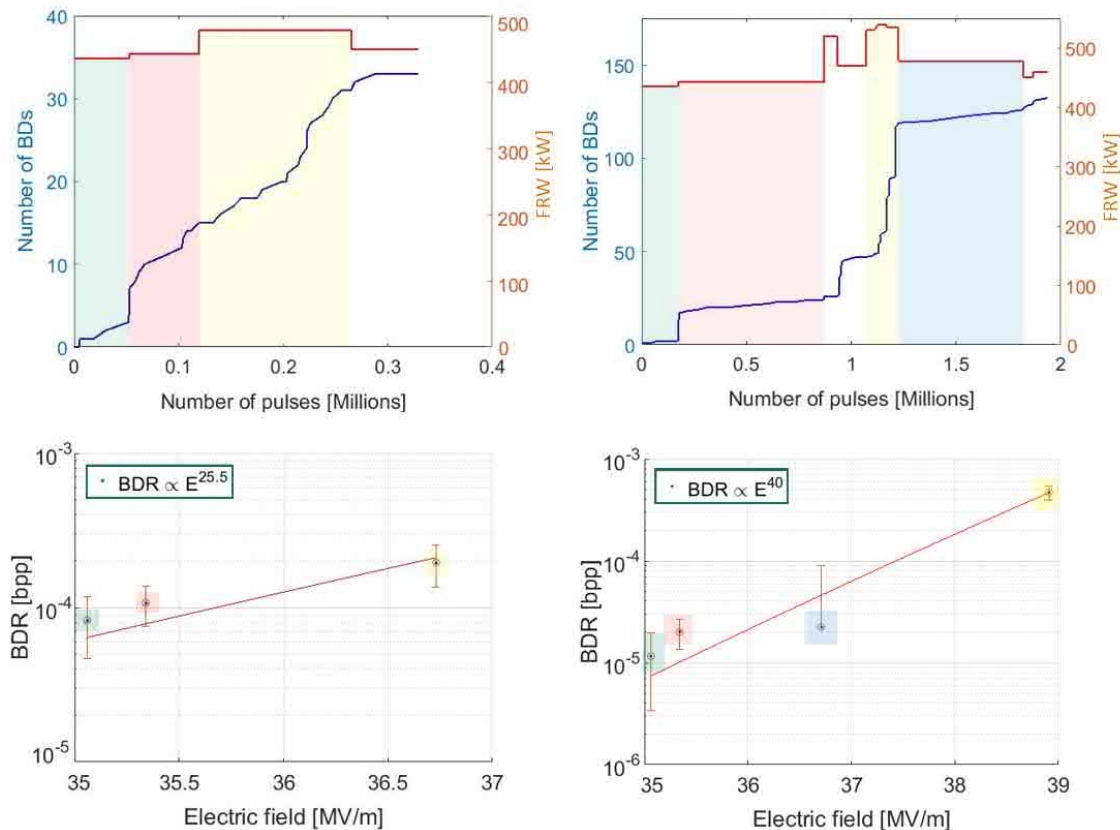


Figure 3.31: History plot (top) of the Linac4 RFQ with different operation regimes: with beam (left) and without beam (right), and BDR versus electric field measurements (bottom).

shows the frequencies of 346.1 MHz and 355.3 MHz at each antennas of the same plate. However they are different along the vane. Longitudinal analysis of BDs presents a wide spectrum of frequencies. BDs divide the volume in two areas: with minimal frequency variation, and with a large frequency range that depends on the BDs location. Transmitted signals in area blocked from the power flow from the coupler go to zero. As shown in Fig. 3.34, the frequency at the end of the structure are kept unchanged, while the rest of the structure has higher frequencies.

The difficulty of this experiment is that the klystron/modulator generates additional frequencies after a BD due to a big reflection back to the klystron creating a standing waves in the waveguide. Fig. 3.35 presents non resonant frequencies that go from incident power and provoke secondary BDs. It is important to note that these frequencies have an interval around 350 MHz between peaks that correspond to the operation frequency of the Linac4 RFQ.

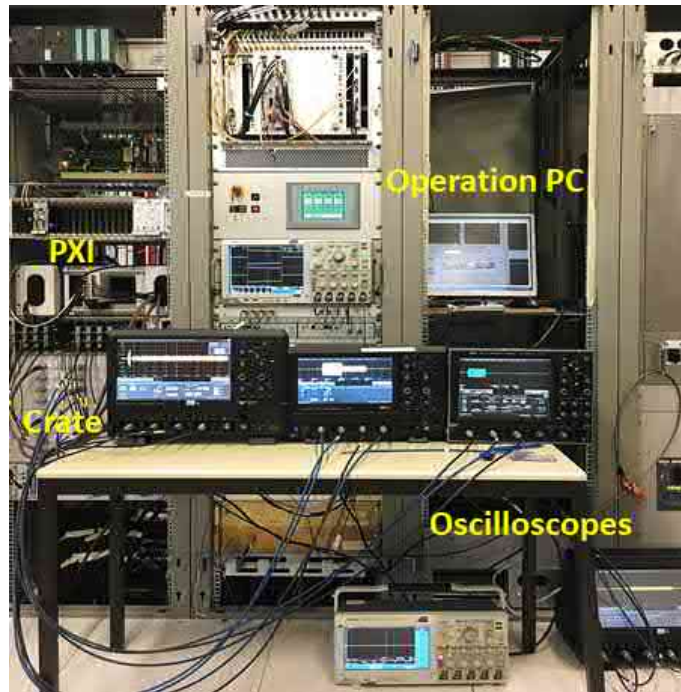


Figure 3.32: Set-up of acquisition system of the Linac4 RFQ.

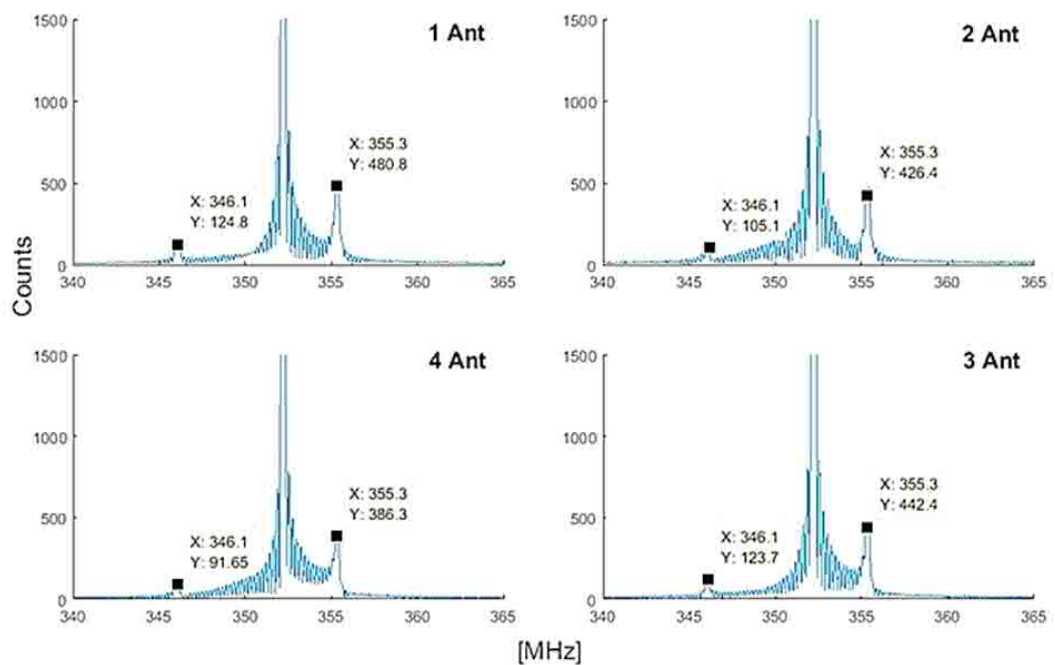


Figure 3.33: Frequency spectrum of the probes power located at the transverse section of the Linac4 RFQ.

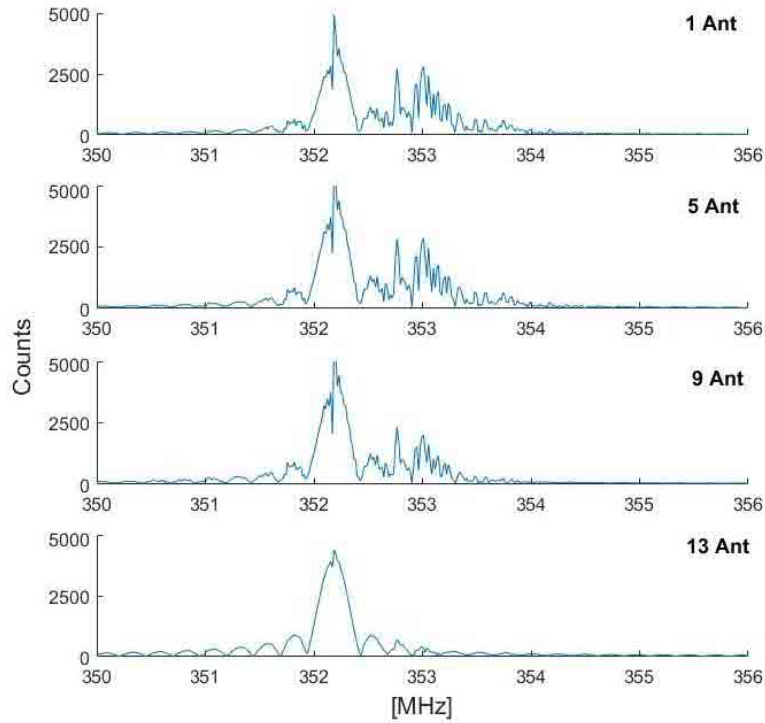


Figure 3.34: Frequency spectrum of the probes power located along the vane of the Linac4 RFQ.

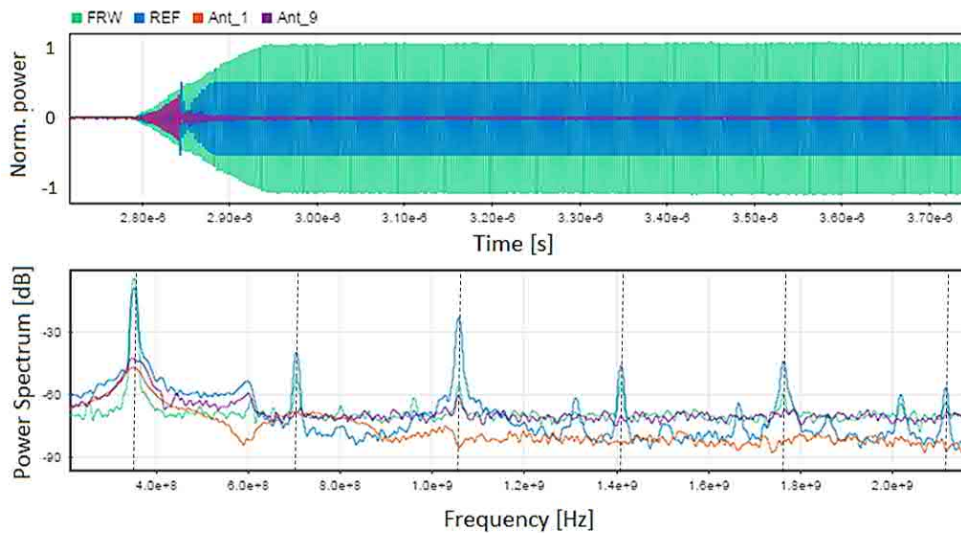


Figure 3.35: Power spectrum of FWD, RFL and two power probes signals located along one vane in time (top) and frequency domain (bottom) measured from the Linac4 RFQ.

Similar to previous measurements made for the HF-RFQ at the ADAM test bench (see Section 3.1.4), a field emission measurement has been realized in the Linac4 RFQ. According to the assumptions, the emission of electrons are caused by the high electric field from the vane at negative RF potential and then accelerated to the adjacent positive vane, absorbing power from the generator. This process has been observed in the RF signals for the RFQ at Linac2 [107]. Some part of the power from the generator was not going into establishing the voltage across the vanes, but a certain amount of this power was going somewhere else. Therefore the dependence of the RF power measured by the probe on the square of the accelerating voltage has to be determined. The measurements have been performed for power exceeding the nominal parameters (3.2 MV that correspond to 440 MW) with variations pulse length. Fig. 3.36 shows the power scan for the voltage ranged from 2.7 to 3.7 MV with pulse length of 400  $\mu$ s. Several measurements have been taken per each given amplitude values to increase measurement accuracy. From a direct proportionality between  $P$  and  $V^2$ , no deviations are observed putting of evidence that there is no DC.

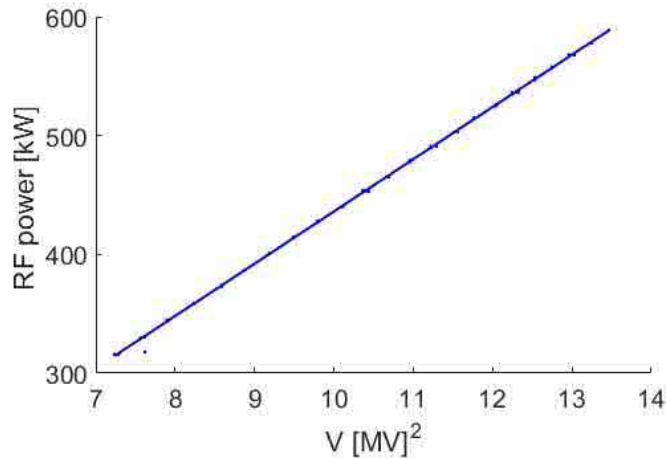


Figure 3.36: Input Power versus vane voltage square for the Linac4 RFQ.

Finally, simulations of the field distribution have been performed for Linac4 RFQ. To obtain a design model, 3D drawings of the structure in AutoCAD format have been converted to the STEP file format. After that, this file was imported to CST as 3D model. A general view of the electric field distribution in a total structure and in one cell randomly chosen from the central part of the structure, are shown in Fig. 3.37. A TE<sub>21</sub> mode is observed along all cells. In our case, the most interesting zone is near the irises, where the surface electric field is the highest. In accordance with this result, the electric field is perpendicular to the Z-coordinate or the direction of the beam propagation, as shown in Fig. 3.38. Therefore the emitted electrons remain inside the structure. The beam is accelerated due to the modulation of the vanes. It is important to note that the distance between the irises is not symmetrical in cross section as was previously demonstrated on a simplified model of HF-RFQ in Chapter 1 (see Fig. 1.6).

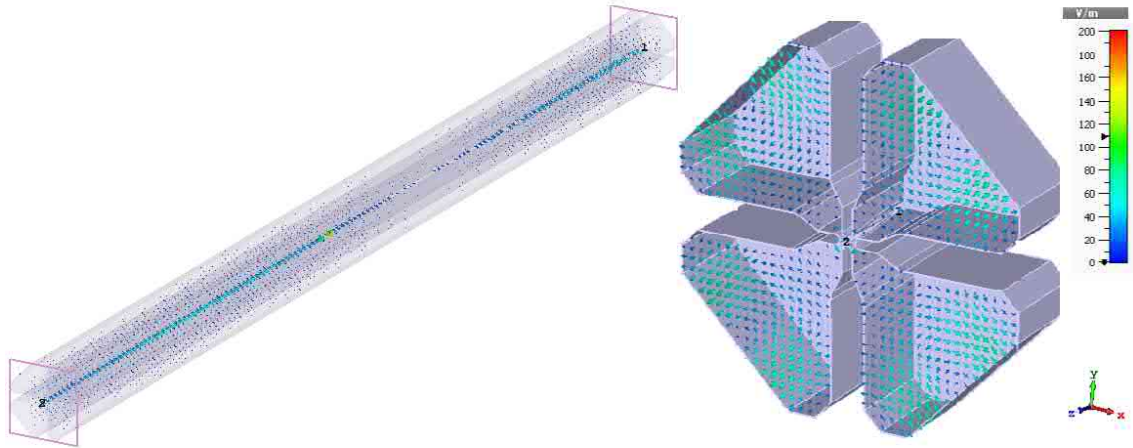


Figure 3.37: Electric field distribution along the entire length (left) and one cell (right) of the Linac4 RFQ.

This model can be used to simulate the field distribution during BDs. If a BD is presented as a short circuit between nearest vanes, the cavity is divided in two sections: with and without field. The distribution may vary based on the position and the size of short circuit. But we will not consider such simulations in this work, since it does not carry physical meaning because many other processes have to be implemented. BDs are very complex processes as there are many physical parameters involved such as the electric field, the pulse heating, and the modified Poynting vector.

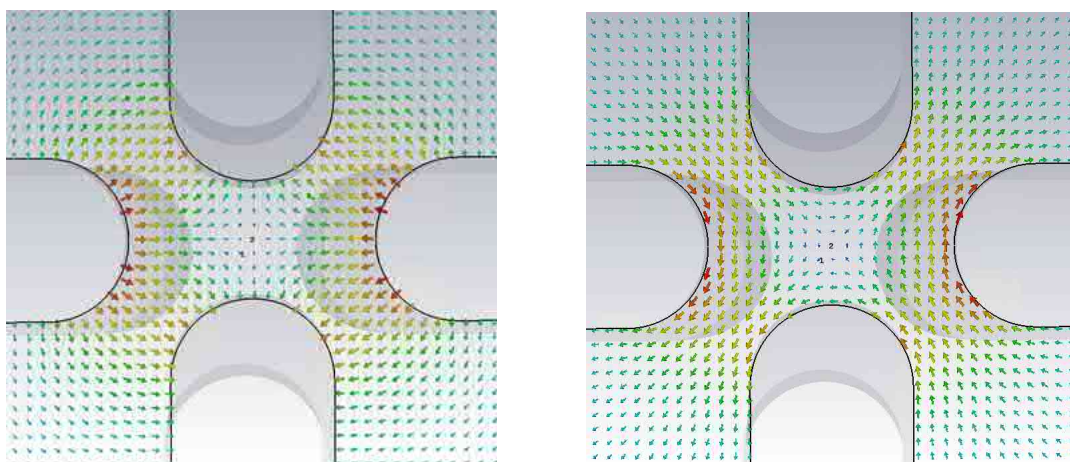


Figure 3.38: Simulation results of the electric (left) and magnetic (right) field distribution near the vane tip of the Linac4 RFQ calculated in CST.

In summary, we can conclude that the Linac4 RFQ is running quite stable at nominal RF parameters without beam. The measurement shows that the incident power can be increased without impact on the performance of the structure. With beam the situation is coming differently. The BDR has increased factor five. Therefore we need to take the beam into consideration in the next generation design of RFQ if we want to increase the gradient from 36 to 50 MV/m (40 %).

The BD measurements in the RFQ requires proper conditions in order to avoid the influence of additional factors as: the gas and the charge particle from the ion source, and the reflected power from the structure. Only after the elimination of these external factors, we could properly study a RFQ performance.



## Chapter 4

# Conclusions

HG RF technology gives the possibility to construct very compact and efficient linear accelerators extending its applications outside of high-energy physics. HG operation of AS, which is carried out under UHV conditions, is limited by the BDs or the vacuum arcs, and is characterized by the BDR. The AS after fabrication initially operate at a reduced performance, and must be high-power conditioned in order to reach the maximum operational gradient. A better understanding of the BD phenomenon could decrease the time required for conditioning and improve the structure performance. This thesis has been focused on the BD studies in various ASs: a 3 GHz HG structure dedicated to medical application, and two RFQs with low (352.2 MHz) and high (750 MHz) frequencies. The main contributions of the thesis work to this field are summarized in this chapter. Further more, the DAQs upgrade have been developed to record the BDs, and to perform the analysis of each of theses ASs.

The first study concerns a prototype of S-band BTW AS for medical applications. The Sbox at CERN has been optimized to test the AS and RF components at higher power. After a conditioning process have been used to safely operate the structure. A peak power level of 32 MW that corresponds to a gradient of 82 MV/m and bunch length of 1.6 ms with a BDR of  $2 \times 10^{-6}$  1/pulse has been obtained. This power level is above the nominal design parameters of 21 MW at 2.5 ms that corresponds to 55 MV/m.

Different studies have been performed to provide a better understanding of the BD limitations in the S-band BTW HT AS. BD localization techniques are used as edge, phase and FC methods. Of particular interest was the location of the BDs around the noses and the coupling holes, since the modified Poynting vector, which is used as one of the main parameters for the design of AS, has maximum value around these areas. According to the results obtained by the post-processing analysis, the BDs occur mainly on the noses. This indicates that the modified Poynting vector cannot be used as the main parameter for the design of AS. Further measurements are required to confirm these results.

The radiation control and the dark current measurements of the structure have also been performed during all the testing period. The electron field emission depends on different parameters such as: the RF input power, the pulse length, and the BD activity. It has to be noted that the dark current, and accordingly the radiation, decreases at a

stable operation of the system when the BDR decreases and BDs occur in one area.

The statistical analysis of the occurrences of BDs have been also performed. The results have shown that BDs are not a random sequence of events and they follow a combination of double Poisson distribution. The probability of BDs event can be described by a two-rate process which assumes primary and secondary BDs. Long term operation demonstrates that the primary BDs are dominant in the first stages of the conditioning, and over time when BDR is decreasing, the probability of secondary BDs and the interval between them are increasing. The conditioning process requires deep studies to explain this phenomena.

The comparative analysis of the conditioning histories obtained from the test of different RF prototypes have shown that the S-band BTW HT and CLIC X-band AS behave in a quite similar way in terms of conditioning speed. The conditioning is limited by the algorithm and the available RF input power. The scaled electric field and scaled modified Poynting vector have been used to directly compare the conditioning histories in order to avoid the influence of the operational parameters of the tests. The results of comparison demonstrate that such normalization is quite suitable also for the S-band BTW HT. However the measured BDR dependence on gradient is quite different from the empirical scaling law determined for other HG prototypes. The conditioning state improves with the number of RF pulses, therefore the high repetition rate of the updated HPRF of CERN S-box gives the possibility to reduce the testing time.

All these results confirm that the S-band BTW HT provides the required parameters for hadron therapy application as well as an additional information on the BD occurrence in the NC HG AS with different designs. The knowledge gained through the work on this thesis can be used to develop a further test stand for conditioning of AS and RF components, in order to calculate the required shielding of the facility and also to perform other studies of vacuum arcs. A deeper study requires further measurement with higher statistics.

A general review of the most leading RFQs that have particular importance for scientific and medical applications have also studied from the point of view of BDs. The main focus of this study was to confirm the possibility to reach higher gradient, which is one of the most important issues in AS optimization.

Two RFQ with high (750 MHz) and low (352.2 MHz) frequencies known as HF-RFQ and Linac4 RFQ respectively have been considered in this work to determine the main limiting parameters of the HG performance, in particular to understand the BD phenomena. The high-power operation of the Linac4 RFQ and HF-RFQ and also their RF systems are described in detail. The data have been collected without disturbing the normal operational regime. It is important to note that, this is one of the first times BD studies have been carried out systematically in these type of devices.

The behaviour of RFQs during a BD event is very different from previous studies of HG AS. In the RFQs, the RF energy is reflected from the structure during BDs without being absorbed. Based on the observations of BD events, an attempt to develop techniques for determining the BD location were made using all available RF signals. EM-fields in the RFQ collapse just after BD starts, and the stored energy is dramatically decreased. The RF resonance cause a shift in the working frequency due to power reflecting from the pole-

---

tip of the vanes. The BD occurring on the pole-tips blocks the coupling between cells, therefore the measured signals from the pickups in the longitudinal direction can have different amplitudes and frequencies. Based on the assumptions of the BD behaviour, the main number of BDs in the Linac4 RFQ occurs at the end of the structure can be caused by the high-energy of the beam at the end of the structure. While for HF-RFQ, the BDs occurred along the structure with a small predominant amount in the central part. This could be related to the location of the power couplers and to small mismatch in the power flow that feeds the structure.

The BDR and RF parameters of HF-RFQ are consistent with the requirements to provide stable operation during treatment. However, the measured BDR of the Linac4 RFQ is quite high. According to observations from the high-power test, most of BDs occur when the fields are building-up and the beam enter in the structure. This could be an indication that the beam and its long length are the main cause of the BDs. In addition, there are also many external factors that have an impact on the system as: the gas and the charge particle from the ion source, and the extra resonant frequencies coming from the klystron. Only after the elimination of external factors, the RFQ performance can be determined.

The measurement of BDR versus gradient have been performed during operation with and without beam in the linac4 RFQ. The high BD activity have been observed in both cases because the structure was not conditioned at such high power before. However, these results are close to the established law for CLIC prototypes.

According to the results, the frequency signal is one of the most relevant parameter of BD location in the RFQs. The frequency shift gives a precise information about BDs. To explore this approach, a dedicated system with high resolution of signal logging is required. The experimental equipment for BD diagnostic can help to draw further conclusions about the BD limitations in HG AS.

Based on all the results presented in this thesis, we can conclude that an all-linac facility for hadron therapy is now a perfectly feasible base on the HG NC AS and the HF-RFQ. These structures can also be used for other facilities where a HG is needed. Another important aspect that has been developed in these thesis is the updates of the DAQs for Sbox, Linac4 RFQ and ADAM RFQ in order to perform the BD studies. All these developments could be used in future studies of the BD phenomenon.



# Appendix A

## DAQ upgrade at CERN's Sbox

The DAQ at CERN's Sbox that was used during the conditioning of the S-band BTW HT have been based on an adapted version of the DAQ system from the CERN's Xbox-2. Due to insufficient computing resources for this software and numerous internal errors, the DAQ has been rewritten to a simplified version of the Xbox-3 LabVIEW. The front panel window of the main Virtual Instrument (VI) is presented in Fig. A.1. The general view is very similar to previous version. The system has been successfully tested with a pulse RF generator. The settings concerning the phase of the pulse have been included in

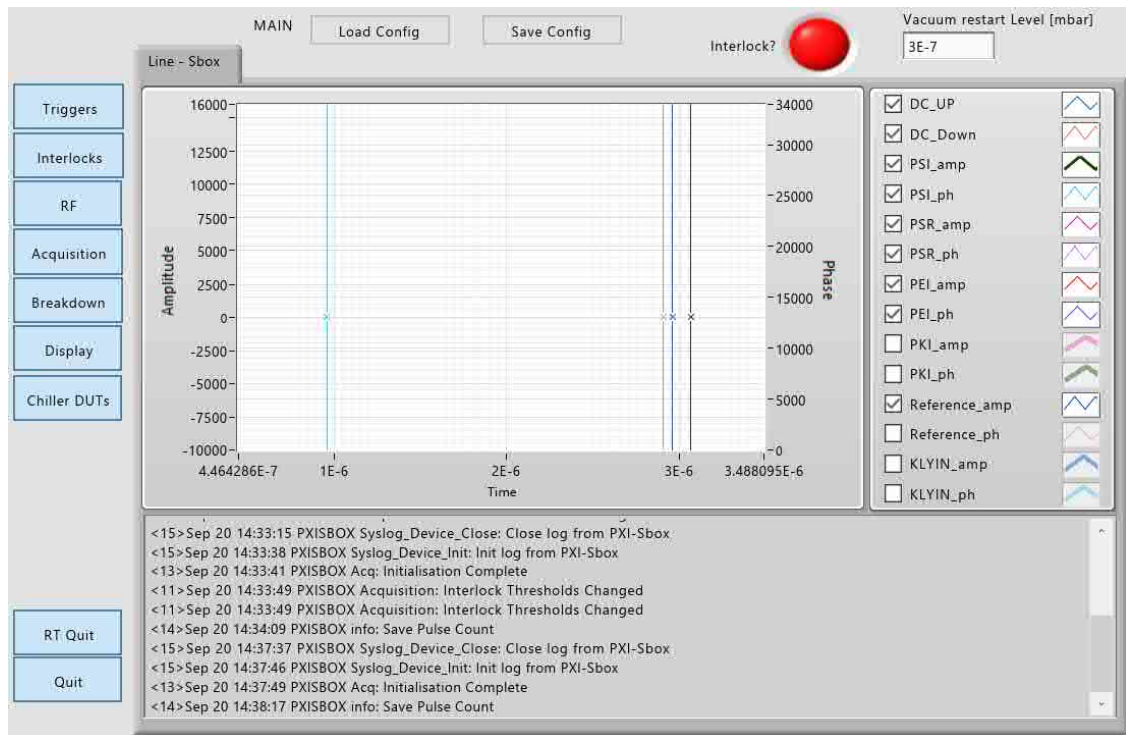


Figure A.1: Control panel of CERN Sbox for high power test.

the DAQ. The current and the previous pulses in case of an interlock have been added to a waveform display as shown in Fig. A.2, this could be useful for comparative analysis of the RF and the DC signals. The BD flags have been assigned to the triggering signals.

Acquisition and threshold systems have been reorganized, the block diagram of acquisition VI is presented in Fig. A.3. A list of items to which access is available through the DAQ is also displayed in this figure. The acquisition control contains all the data and settings needed by the acquisition loop. One of the main tasks was to increase the efficiency of the system.

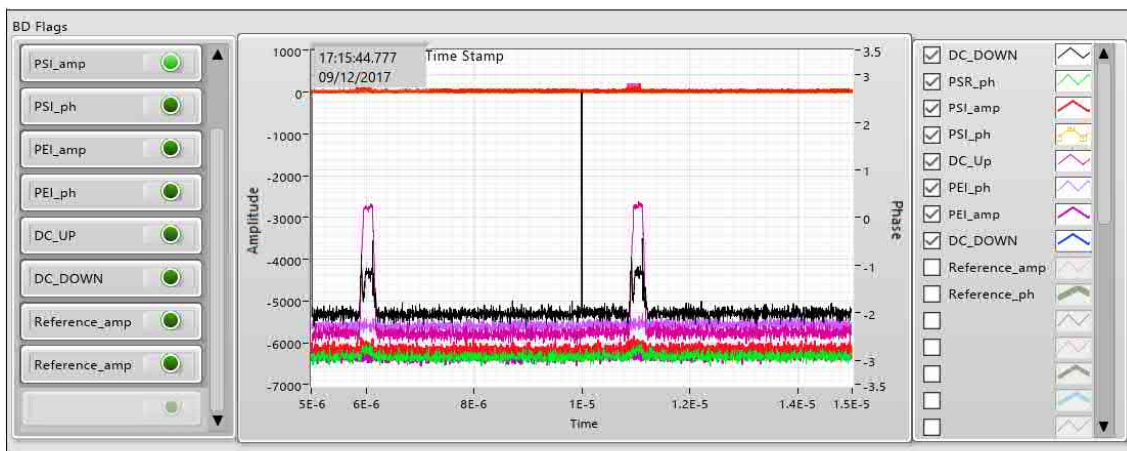


Figure A.2: BD detection VI with flags corresponds to triggering a signal and waveform display of current and previous pulse in case of BD for Sbox at CERN.

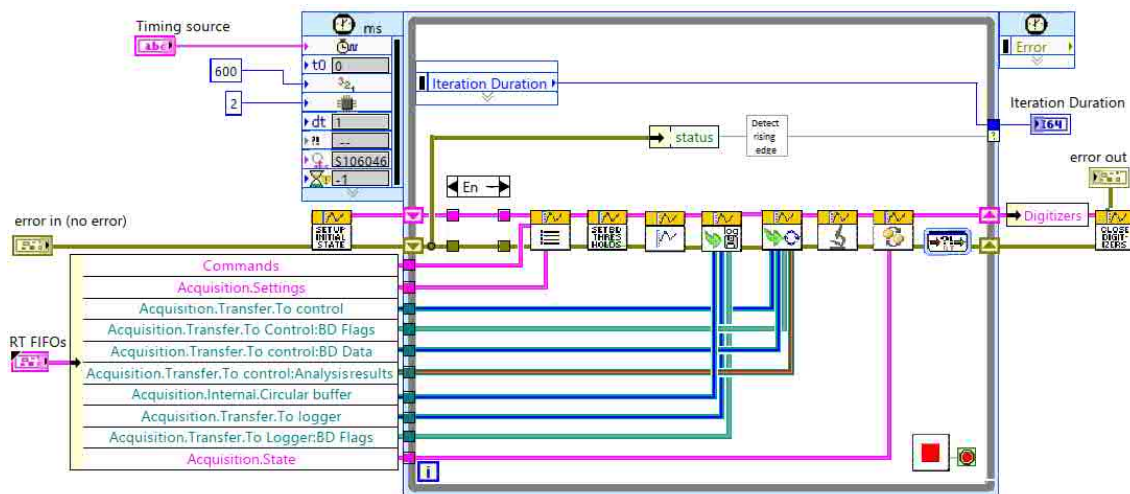


Figure A.3: Block diagram of Acquisition VI in Sbox at CERN.

The initial stage for BD set up is displayed in Fig. A.4. This VI calculates the length of the array and the indexes for the various channels. The data from all cards is stored in a single 1D array. The first element in the data array starts from zero. After that, an analysis is carried out to determine the BD and subsequent generating TDMS file.

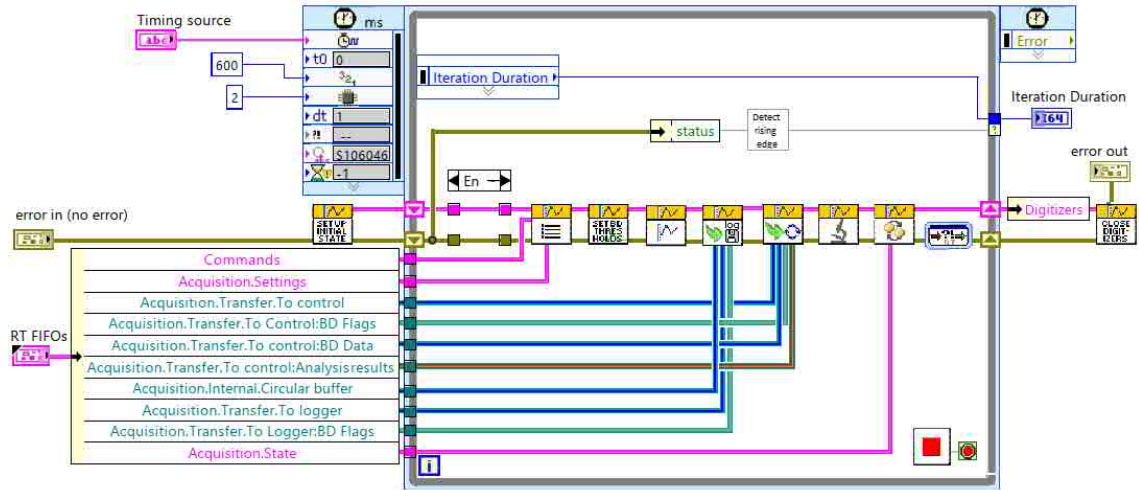


Figure A.4: VI for the set up of the initial state for a BD detection in Sbox at CERN.

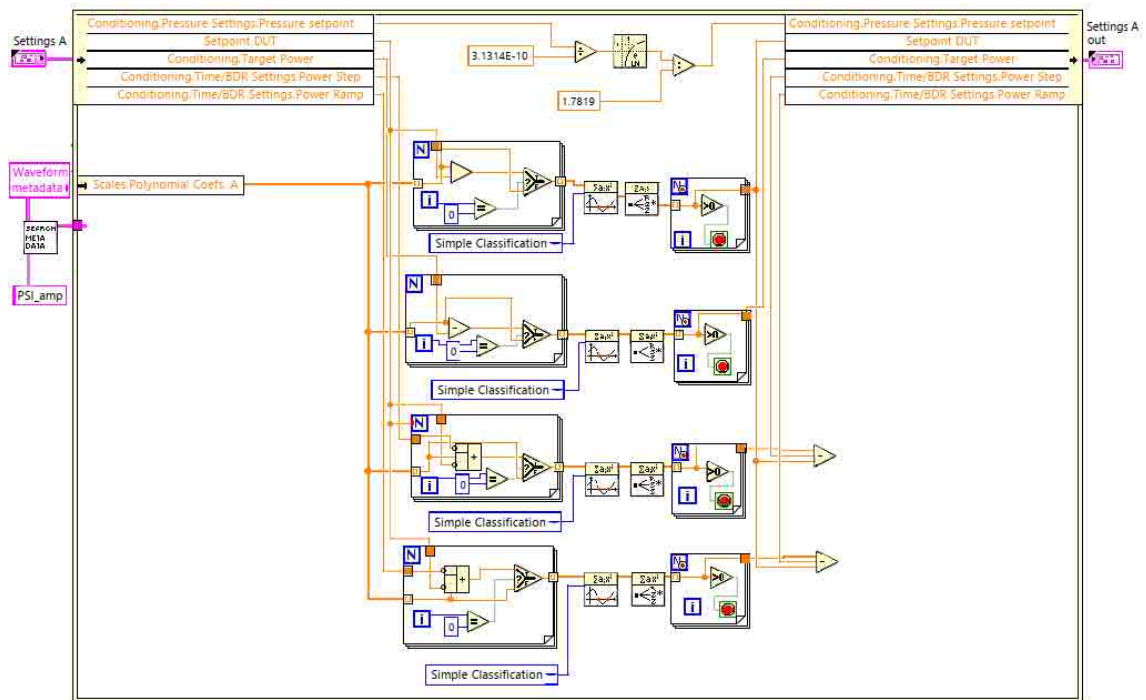


Figure A.5: Conditioning algorithm settings used for Sbox at CERN.

The number of BD pulses is counted through the BD buffer by a pulse counter that is used to calculate the BDR. The conditioning algorithm is similar to the one used in the Xbox-3 (see Fig. A.5), that was developed for CLIC X-band AS. Input settings as the target power, the power step and the power ramp are also used for conditioning. Additional settings are imposed through the triggers used for BD detection that could be set manually depending on the input power. This approach allows to respond more effectively in the case of BD clustering.

## Appendix B

# DAQ upgrade of HF-RFQ at the ADAM test stand at CERN

The initial DAQ version at the ADAM test stand was developed for the high power tests of the different type of AS implementing: signal generation control, signal acquisition and calibration, PLC parameters monitoring and data logging. The upgrade have been performed to logging all available RF signals related to the HF-RFQ during BD events.

This DAQ provides a single interface parameter monitoring and data logging. The VI contains two tabs: one for signal “Control and Acquisition” and another one for “Settings” all the inputs needed by the program. Logging is performed in an automatic way. When the program is running, all the data is monitored constantly. The list of signals read by the program and the main processes of reading and writing files with set the properties and specifies the property names of the specified channel group are displayed in Fig. B.1. The program reads 16 RF signals in the following order: 4 forward from drivers, 4 forward from IOTs, 4 reflected and 4 pickups.

The VIs of two methods of the BD identification that have been implemented in the program are shown in Fig. B.2. Both approaches are based on the evaluation of the flatness of RF pulses. The conditions for BD identification can vary, depending on the field stability in the RFQ and the mismatch between the coaxial line and the structure. The first one determines the average value of the selected part of the signal and compares it with the specified nominal value. The acquisition window responsible for the “Breakdown detection” based on this approach is presented in Fig. B.2. For this case, the reflected power from one of the directional coupler have been selected as a reference signal. The second method named as “Detect instability” calculates the roughness of the pulse and the deviation from the value specified in the settings gives possibility to detect the unstable pickup signals. The block diagram of this process is shown in Fig. B.3.

The “Export BD” or “Export instability” switch has to be activated (as show in Fig. 3.8) to save the RF signals. The logging occur when the calculation and specified parameters are met. The date is added in the automatically generated filename. Errors related with data logging are shown in the error field of this group. The scheme of signal logging is presented on the block diagram in the bottom part of Fig. B.3. Such analysis is

applied to each input pulse.

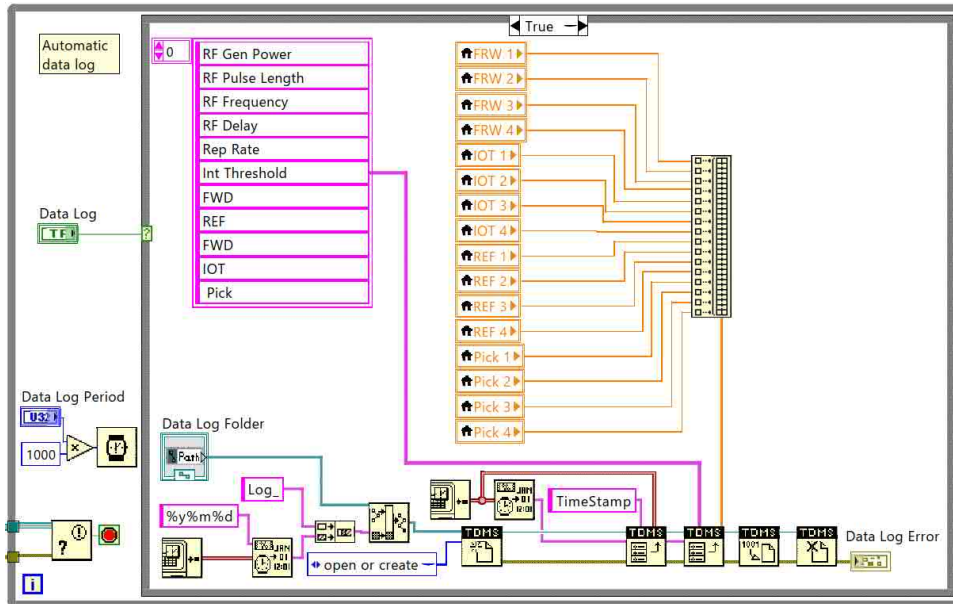


Figure B.1: Automatic data log in the DAQ for monitoring RF signals in the HF-RFQ.

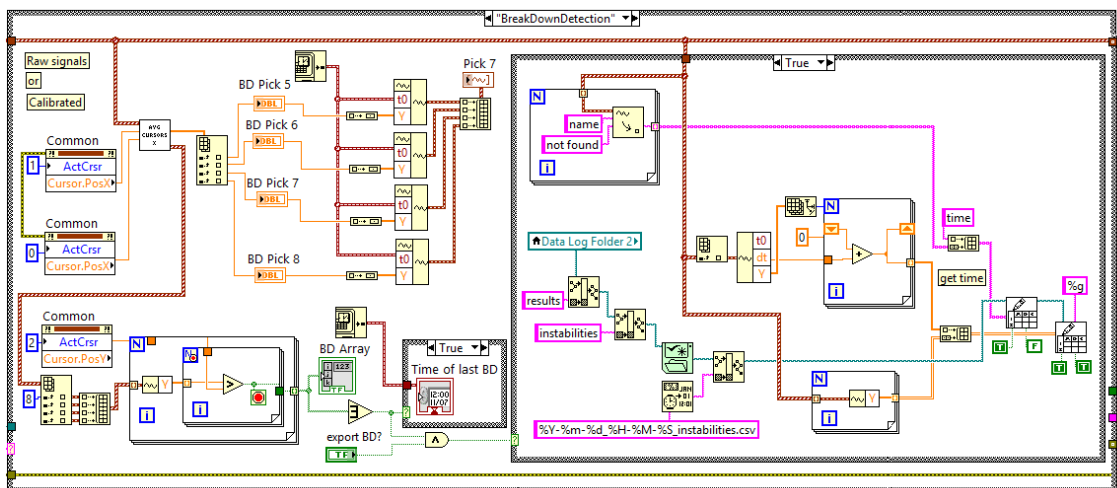


Figure B.2: BD detection technique implemented in the DAQ of the HF-RFQ.

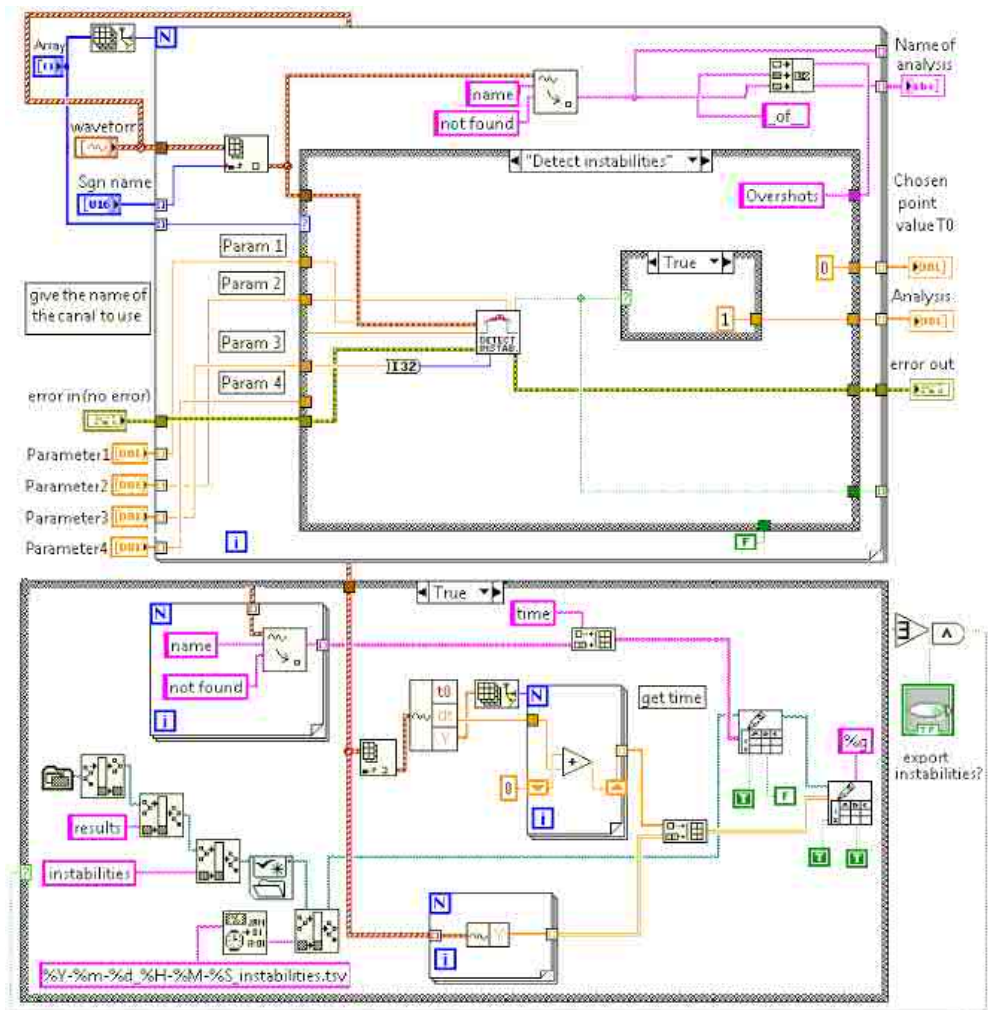


Figure B.3: Block diagram used for detect instabilities in the DAQ of HF-RFQ.



## Appendix C

# DAQ update of Linac4 RFQ

Different versions of the DAQ were developed and used for the high power test and commissioning of the Linac4 RFQ at the 3 MeV Test Stand and after in the tunnel driven by a fully digital LLRF system. The purpose of this system was to control the uniformity of field along the structure by pickups reader. The last updated version of the DAQ has been reorganized to constant monitoring of the system and logging signals in the case of BD events.

The detection of BDs in the DAQ of Linac4 RFQ have been accomplished by implementing a general polynomial fit to the flat-top of the read signal (see Fig. C.1). This algorithm is applied to one of the pickup signals. While for the remaining signals, we indicate the time to determine the value of the signal for visualization in analysis result display with further recording to a history file. The block diagram of the pulse instability detection implemented in the DAQ of Linac4 RFQ is shown in Fig. C.2.

Besides, other calculations can be performed, for example: the maximum and the minimum values, the rise time and the fall time, the width at 50 % and 90 %, the root mean square (RMS) of the pickup signals. To accomplish this, the following parameters must be set: type of analysis, read signal and required parameters. All explanations are indicated in the program. A window, where all requirements for execution are indicated, is shown in Fig. C.3.

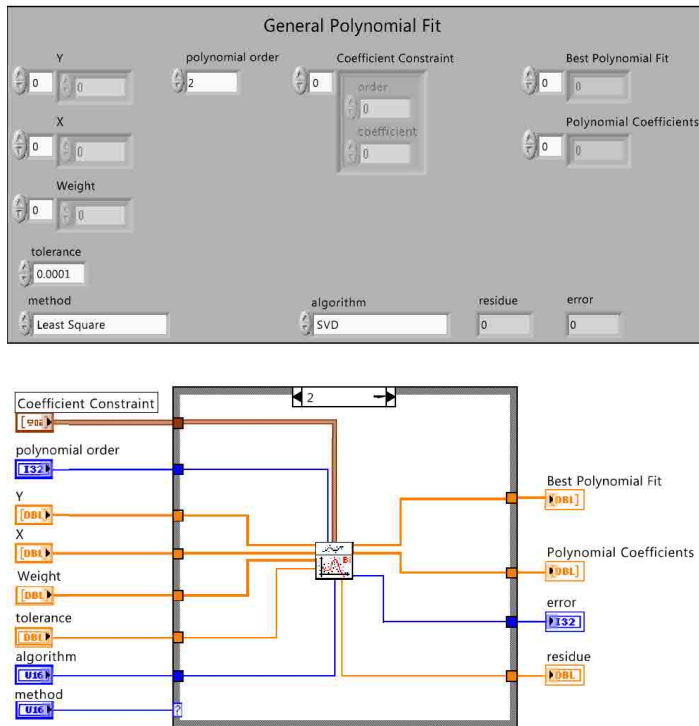


Figure C.1: VI of general polynomial fit implemented in the DAQ of Linac4 RFQ: the front panel window (top) and the block diagram (bottom).

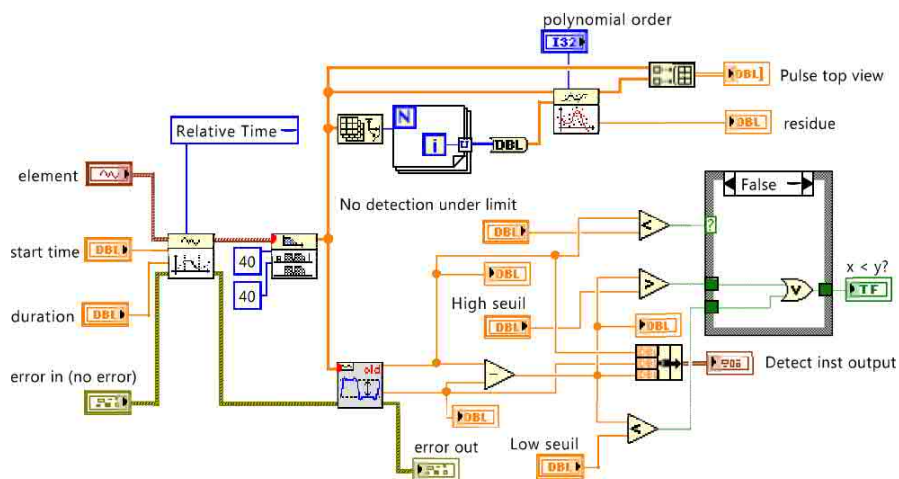


Figure C.2: The block diagram of the pulse instability detection in the DAQ of Linac4 RFQ.

EDIT ANALYSIS PARAMETERS					
Analysis	Channel	Parameter 1	Parameter 2	Parameter 3	Parameter 4
Value at t0	Ant3(kW)	0.00278	0	0	0
Value at t0	Ant4(kW)	0.00278	0	0	0
Value at t0	Ant5(kW)	0.00278	0	0	0
Maximum	t16(kW)	0.00278	0	0	0
Minimum	t17(kW)	0.00278	0	0	0
Risetime	t18(kW)	0.00278	0	0	0
Falltime	t19(kW)	0.00278	0	0	0
Width at 50%	t10(kW)	0.00278	0	0	0
Width at 90%	t11(kW)	0.00278	0	0	0
RMS	t12(kW)	0.00278	0	0	0
Detect instabilities	t13(kW)	0.00278	0	0	0
Detect instabilities point 2	t14(kW)	0.00278	0	0	0
Integral	t15(kW)	0.00278	0	0	0
✓ Value at t0	Ant16(kW)	0.00278	0	0	0
Maximum_within_t1_t2	Ant1(kW)	0.00235	0.003	1	520
Value at t0	<13>	0	0	0	0

**EXIT**

Figure C.3: Example of the parameters for analysis in the DAQ of Linac4 RFQ.



# Bibliography

- [1] JLC Design Study. KEK-Report-97-1, April 1997, <http://lss.fnal.gov/archive/other1/kek-report-97-1.pdf>.
- [2] CLIC Project website: <http://clic-study.web.cern.ch/clic-study/>.
- [3] A Multi-TeV linear collider based on CLIC technology. CLIC Conceptual Design Report edited by M. Aicheler, P. Burrows, M. Draper, T. Garvey, P. Lebrun, K. Peach, N. Phinney, H. Schmickler, D. Schulte and N. Toge. CERN, 2012: <http://project-clic-cdr.web.cern.ch/project-CLIC-CDR/>.
- [4] Next Linear Collider (NLC) website: <http://www-project.slac.stanford.edu/lc/nlc>.
- [5] A. Descoedres, Y. Levinsen, S. Calatroni, M. Taborelli, and W. Wuensch, Investigation of the dc vacuum breakdown mechanism, *Phys. Rev. ST Accel. Beams* 12, 092001, 2009.
- [6] V.A. Dolgashev and S.G. Tantawi, SLAC Report No. 10175, 2003.
- [7] K. Nordlund and F. Djurabekova, Defect model for the dependence of breakdown rate on external electric fields, *Phys. Rev. ST Accel. Beams* 15, 071002, 2012.
- [8] T. Wangler. Principles of RF Linear Accelerators. John Wiley and Sons, 1st edition, 1998.
- [9] K.-J. Kang, Y.-X. Wei, B. Dwersteg, The Computer Aided Test System for RF Superconducting Cavity High-Q Measurement, In *Proceedings of the Fifth Workshop on RF Superconductivity*, DESY, Hamburg, Germany, August, 1991.
- [10] F. Gerigk. Cavity types. In Proceedings of the CERN Accelerator School CAS 2010, 2011. Presented at the CAS 2010: RF for accelerators, Ebeltoft, 8-17 June 2010; CERN-2011-007.
- [11] R.B. Neal et al., The Stanford Two-miles Accelerator, Stanford University, W.A. Benjamin, *Inc.*, New York, 1968.
- [12] A. Degiovanni, High gradient proton linacs for medical applications. PhD thesis, École Polytechnique Fédérale de Lausanne, 2014.

- [13] S. Benedetti et al., Fabrication and testing of a novel S-band backward traveling wave accelerating structure for proton therapy linacs. In *Proceedings of the 28th Linear Accelerator Conference, LINAC2016*, East Lansing, MI, USA, 2016.
- [14] A. M. Lombardi, The radio frequency quadrupole (RFQ), CAS - CERN Accelerator School and KVI: Specialised CAS Course on Small Accelerators, Zeegse, The Netherlands, 24 May - 2 Jun 2005, pp.201-207 (CERN-2006-012), <https://doi.org/10.5170/CERN-2006-012.201>.
- [15] R.H. Stokes and T.P. Wangler, Radio Frequency Quadrupole and their applications, *Annual Review of Nuclear and Particle Science*, 1989.
- [16] K.R. Crandall, R.H. Stokes and T.P. Wangler, RF quadrupole beam dynamics design study. In *Proceedings of the Linear Accelerator Conference*, 1979.
- [17] C.E. Hill, A.M. Lombardi, W. Pirkel, E. Tanke, and M. Vretenar, Performance of the CERN Linac 2 with a High Intensity Proton RFQ. In *Proceedings of the International Linac Conference*, Tsukuba, Japan, 1994.
- [18] J. Rodnizki, Z. Horvitz, RF and Heat Flow Simulations of the SARAF RFQ 1.5 MeV/nucleon. In *Proceedings of Linear Accelerator Conference LINAC2010*, Tsukuba, Japan, 2010.
- [19] C. Schmidt, J. Tuning and Optimization of the Field Distribution for 4-Rod Radio Frequency Quadrupole Linacs. Dissertation, Johann Wolfgang Goethe-Universität, Frankfurt am Main, 2014.
- [20] A. Palaia, Beam Momentum Changes due to Discharges in High-gradient Accelerator Structures, Ph.D. thesis, Uppsala U., 2013.
- [21] D. González Iglesias, Analysis of the multipactor effect in microwave waveguides and transmission lines, Ph.D. thesis, Phys. Dept., Valencia, Spain, 2017.
- [22] W. Wuensch, Advances in the Understanding of the Physical Processes of Vacuum Breakdown, *Tech. Rep.*, CLIC-Note-1025, CERN, Geneva, May 2013.
- [23] W.D. Kilpatrick, *Rev. Sci.Instrum*, 28(10), p. 824, 1957, <http://dx.doi.org/10.1063/1.1715731>.
- [24] D.E. Young, D.E., *Proc. Heavy Ion Fusion Workshop*, Brookhaven National Laboratory Report BNL 50769, p. 17, 1977.
- [25] R.H. Fowler and L. Nordheim, Electron Emission in Intense Electric Fields, *Proc. R. Soc. Ser. A* 119, pp. 173-181, 1928.
- [26] F. Rohrbach. Recent developments in the application of high voltage gas breakdown in high energy nuclear physics. In *Proceedings of 4th International Conference on Gas Discharges*, Swansea, UK, pp. 433-438, 1976.

- 
- [27] J. Giner-Navarro, Breakdown studies for high gradient RF warm technology in: CLIC and hadrontherapy linacs, Ph.D. thesis, Phys. Dept., Valencia, Spain, 2016.
- [28] W. Wuensch. Observations about RF Breakdown from the CLIC High Gradient Testing Program. *CERN CLIC Notes*, (700), December 2006, <https://doi.org/10.1063/1.2409116>.
- [29] W. Wuensch et al. A High-Gradient Test of an 30 GHz Molybdenum-Iris Structure. In *Proceedings of EPAC06*, Edinburgh, Scotland, 2006.
- [30] Shao Jiahang. Investigations on rf breakdown phenomenon in high gradient accelerating structures, Springer Theses, Recognizing Outstanding Ph.D. Research, 2190-5053, 2018.
- [31] J.W. Wang and G.A. Loew. Field Emission and RF Breakdown in High-Gradient Room-Temperature Linac Structures. *Stanford Linear Accelerator Center Technical Report*, SLAC-PUB-7684, 1997.
- [32] A. Grudiev, S. Calatroni, and W. Wuensch, New local field quantity describing the high gradient limit of accelerating structures, *Phys. Rev. ST Accel. Beams* 12, 102001, 2009, <https://doi.org/10.1103/PhysRevSTAB.12.102001>.
- [33] ANSYS HFSS: High Frequency Electromagnetic Field Simulation, [www.ansys.com/Products/Electronics/ANSYS-HFSS](http://www.ansys.com/Products/Electronics/ANSYS-HFSS).
- [34] CST: Computer Simulation Technology, <https://www.cst.com/products/csts2>.
- [35] Perry B. Wilson. Scaling linear colliders to 5 TeV and above. In *ITP Conference on Future High Energy Colliders*, University of California, Santa Barbara, 1996.
- [36] H. Braun, R. Corsini, J. P. Delahaye, A. de Roeck, S. Dbert, A. Ferrari, G. Geschonke, A. Grudiev, C. Hauviller, B. Jeanneret, E. Jensen, T. Lefvre, Y. Papaphilippou, G. Riddone, L. Rinolfi, W. D. Schlatter, H. Schmickler, D. Schulte, I. Syratchev, M. Taborelli, F. Tecker, R. Toms, S. Weisz, and W. Wuensch. CLIC 2008 parameters, *Tech. Rep.*, CERN CLIC-Note-764, October 2008.
- [37] W. Wuensch, Advances in the Understanding of the Physical Processes of Vacuum Breakdown, *Tech. Rep.*, CLIC-Note-1025, CERN, Geneva, May 2013.
- [38] D. Schardt, T. Elsässer, D. Schulz-Ertner. Heavy-ion tumor therapy: physical and radiobiological benefits. *Rev Mod Phys*, 82, pp. 383–425, 2010, <https://doi.org/10.1103/RevModPhys.82.383>.
- [39] T. Haberer, W. Becher, D. Schardt, G. Kraft. Magnetic scanning system for heavy ion therapy. *Nucl Instrum Methods Phys Res A* 330, pp. 296–305, 1993.
- [40] E. Pedroni, R. Bacher, H. Blattmann, T. Böhringer, A. Coray, A. Lomax, et al. The 200-MeV proton therapy project at the Paul Scherrer Institute: conceptual design and practical realization. *Med Phys*, 22, pp. 37–53, 1995.

- [41] World Health Organization: WHO, <https://www.who.int/cancer/en/>.
- [42] Particle Therapy Cooperative Group (PTCOG), <https://www.ptcog.ch/index.php/facilities-in-operation/>.
- [43] C. Baumgarten, Cyclotrons with fast variable and/or multiple energy extraction, *Physical Review Special Topics-Accelerators and Beams*, vol. 16, no. 10, p. 100101, 2013.
- [44] B. Marchand, D. Prieels, B. Bauvir, R. S epulche, M. G erard, IBA proton pencil beam scanning: an innovative solution for cancer treatment, *Proc. Eur. Part. Accel. Conf.*, Vienna, Austria, pp. 2539–2541, 2000.
- [45] R.W. Hamm, K.R. Crandall, and J.M Potter. Preliminary design of a dedicated proton therapy linac. In *Proceedings of the IEEE Particle Accelerator Conference PAC'91*, pp. 2583-2585, San Francisco, USA, 1991.
- [46] U. Amaldi, M. Grandolfo and L. Picardi, The RITA Network and the Design of Compact Proton Accelerators, Chapter 9. Eds, INFN, Frascati, 1996.
- [47] U. Amaldi, P. Berra, K. Crandall, D. Toet, M. Weiss, R. Zennaro, E. Rosso, B. Szeless, M. Vretenar, C. Cicardi, C. De Martinis, D. Giove, D. Davino, M.R. Masullo and V. Vaccaro, LIBO - A Linac-Booster for Protontherapy: Construction and Tests of a Prototype. *Nucl. Instr. and Meth. A*, vol. 521, pp. 512-529, 2004.
- [48] C. De Martinis et al., Acceleration tests of a 3 GHz protonlinear accelerator (LIBO) for hadron therapy, *Nucl. Instrum. Methods Phys. Res., Sect. A* 681, 10, 2012.
- [49] ADAM website: <https://www.avoplc.com/Our-Technology/Overview-of-the-LIGHT-System>.
- [50] C. De Martinis et al, Acceleration tests of a 3 GHz proton linear accelerator (LIBO) for hadrontherapy. *Nuclear Instruments and Methods A*, 681:10-15, July 2012.
- [51] A. Degiovanni and U. Amaldi, Proton and carbon linacs for hadron therapy. In *Proceedings of the 27th Linear Accelerator Conference, LINAC2014*, Geneva, Switzerland, FRIOB02, pp. 1207-1212, 2014.
- [52] M. Vretenar, E. Montesinos, M. Timmins, M. Garlasch e, A. Grudiev, A. Dallochio, S. Mathot, V. Dimov, and A. Lombardi, A compact high-frequency RFQ for medical applications, in *Proceedings of the 27th Lineac Accelerator Conference, LINAC2014*, Geneva, Switzerland, 2014.
- [53] A.M. Lombardi et al, Beam Dynamics in a high frequency RFQ. In *Proceedings of the 6th International Particle Accelerator Conference IPAC'15*, Richmond, USA, 2015.

- 
- [54] M. Vretenar, A. Dallocchio, V. A. Dimov, M. Garlasché, A. Grudiev, A. M. Lombardi, S. Mathot, E. Montesinos and M. Timmins. A compact high-frequency RFQ for medical applications. In *Proceedings of the 27th Linear Accelerator Conference, LINAC14*, pp. 935-938, Geneva, Switzerland, 2014, <https://cds.cern.ch/record/2062619>.
- [55] S. Benedetti, A. Grudiev, A. Latina. High gradient linac for proton therapy. *Phys. Rev. Accel. Beams*, 20(4): 40101, 2017. <https://doi.org/10.1103/PhysRevAccelBeams.20.040101>.
- [56] E. Chesta, F. Caspers, W. Wuensch, S. Sgobba, T. Stora, P. Chiggiato, and M. Taborelli. Overview of CERN Technology Transfer Strategy and Accelerator-Related Activities, May 2013.
- [57] J. Shi, A. Grudiev and W. Wuensch. Tuning of x-band traveling-wave accelerating structures. *Nuclear Instruments and Methods in Physics Research Section A: Accelerators, Spectrometers, Detectors and Associated Equipment*, 704:1418, 2013, <https://doi.org/10.1016/j.nima.2012.11.182>.
- [58] S. Benedetti. High-gradient and high-efficiency linear accelerators for hadron therapy. Lausanne, EPFL, 2018, <https://doi.org/10.5075/epfl-thesis-824>.
- [59] W. Farabolini, F. Peauger, J. Barranco, S. Bettoni, B. Constance, R. Corsini, M. Csatari, S. Doebert, A. Dubrovskiy, T. Persson, G. Riddone, P. K. Skowronski, F. Tecker, D. Gudkov, A. Solodko, M. Jacewicz, T. Muranaka, A. Palaia, R. Ruber, and V. Ziemann. Two beam test stand experiments in the CLEX CTF3 facility. In *Proceedings of International Particle Accelerator Conference, IPAC'11*, pp. 29-31, San Sebastian, Spain, 2011.
- [60] F. Peauger, A. Hamdi, S. Curt, S. Doebert, G. McMonagle, G. Rossat, K.M. Schirm, I. Syrathev, L. Timeo, S. Kuzikhov, A.A. Vikharev, A. Haase, D. Sprehn and A. Jensen. A 12 GHz RF power source for the CLIC study. In *Proceedings of the International Particle Accelerator Conference IPAC2010*, pp. 3990-3992, Kyoto, Japan, 2010.
- [61] A. Vnuchenko et al., High Gradient Performance of an S-Band Backward Travelling Wave Accelerating Structure for Medical Hadron Therapy Accelerators, in *Proceedings of the 9th. International Particle Accelerator Conference, IPAC'18*, Vancouver, Canada, 2018: <http://ipac2018.vrws.de/papers/mopml043.pdf>.
- [62] G. Geschonke, A. Ghigo. CTF3 Design Report, CERN, Geneva, CERN-PS-2002-008-RF. CTF3-NOTE-2002-047. LNF-2002-008-IR, May, 2002, <https://cds.cern.ch/record/559331>.
- [63] LabVIEW, National Instruments, <http://www.ni.com/labview/>.
- [64] B.J. Woolley, High Power X-band RF Test Stand Development and High Power Testing of the CLIC Crab Cavity, Ph.D. thesis, Lancaster University, 2015.

- [65] A. Degiovanni, W. Wuensch and J. Giner Navarro, Comparison of the conditioning of high gradient accelerating structures, *Phys. Rev. Accel. Beams* no.3, 19, 032001, 2016, <https://doi.org/10.1103/PhysRevAccelBeams.19.032001>.
- [66] Testing the CONV-TTL-BLO, <https://www.ohwr.org/project/conv-ttl-blo-tst/wikis/Testing>.
- [67] N. Catalan Lasheras et al., Construction and commissioning Xbox 3: a very high capacity X-band test stand, in *Proceeding IEEE Power Modulator and High Voltage Conference*, San Francisco, USA, 2016.
- [68] A. Degiovanni, S. Doebert, W. Farabolini, A. Grudiev, J. Kovermann, E. Montesinos, G. Riddone, I. Syratchev, R. Wegner, W. Wuensch, A. Solodko and B. Woolley. High-gradient test results from a CLIC prototype accelerating structure: TD26CC. In *Proceedings of the International Particle Accelerator Conference, IPAC'14*, pp. 2285-2287, Dresden, Germany, 2014, <https://doi.org/10.18429/JACoW-IPAC2014-WEPME015>.
- [69] N. Catalan-Lasheras, A. Degiovanni, S. Doebert, W. Farabolini, J. Kovermann, G. McMonagle, B. Woolley, and J. Tagg. Experience Operating an X-Band High-Power Test Stand at CERN. In *Proceedings of the 5th International Particle Accelerator Conference*, Dresden, Germany, 2014.
- [70] A. Degiovanni, S. Doebert, W. Farabolini, I. Syratchev, W. Wuensch, J. Giner Navarro, J. Tagg and B. Woolley. Diagnostics and analysis techniques for high power X-band accelerating structures. In *Proceedings of the 27th Linear Accelerator Conference, LINAC14*, pp. 490-492, Geneva, Switzerland, 2014.
- [71] A. Palaia, V. Dolgashev, J. Lewandowski and S. Weathersby. Diagnostics of RF breakdowns in high-gradient accelerating structures. In *Proceedings of the International Particle Accelerator Conference, IPAC'13*, pp. 527-529, Shanghai, China, 2013.
- [72] W. Wuensch, The Scaling of the Travelling-Wave RF Breakdown Limit, CLIC-Note-649, 2006.
- [73] W. Wuensch, CLIC Accelerating Structure Development, in *Proceedings of EPAC08*, Genoa, Italy, pp. 2922-2926, 2008.
- [74] J.W. Wang and G.A. Loew, Field emission and RF breakdown in high-gradient room-temperature linac structures. SLAC PUB 7684, Oct. 1997.
- [75] D. Banon-Caballero, M. Boronat, N. Catalán Lasheras, A. Faus-Golfe, B. Gimeno, T.G. Lucas, W.L. Millar, J. Paszkiewicz, S. Pitman, V. Sánchez Sebastián, A. Vnuchenko, M. Volpi, M. Wadorski, W. Wuensch, and V. del Pozo Romano. Dark Current Analysis at CERN's X-band Facility, in *Proceeding of the 10th International Particle Accelerator Conference, IPAC'19*, Melbourne, Australia, pp. 2944-2947, 2019, <https://doi.org/10.18429/JACoW-IPAC2019-WEPRB059>.

- 
- [76] C. Adolphsen, SLAC Technical Report No. SLAC-PUB-9906, 2003.
- [77] T. Higo, T. Abe, Y. Arakida, S. Matsumoto, T. Shidara, T. Takatomi, M. Yamanaka, A. Grudiev, G. Riddone, and W. Wuensch, Comparison of High-Gradient Performance in Varying Cavity Geometries, in *Proceedings of the 4th International Particle Accelerator Conference, IPAC'13*, Shanghai, China, 2013.
- [78] W. Wuensch, A. Degiovanni, S. Calatroni, A. Korsbäck, F. Djurabekova, R. Rajamäki, and J. Giner-Navarro, Statistics of vacuum breakdown in the high-gradient and low-rate regime, *Phys. Rev. Accel. Beams* 20, 011007, 2017, <https://doi.org/10.1103/PhysRevAccelBeams.20.011007>.
- [79] VDL Enabling Technologies Group, <https://www.vdletg.com/nl>.
- [80] Bodycote Engineering Services, <https://www.bodycote.com/>.
- [81] Paul Scherrer Institute PSI, <https://www.psi.ch/en>.
- [82] Yvon boyer, <https://www.boyer-mecanique-precision.com/>.
- [83] Reiser, Martin. Theory and design of charged particle beams (2nd ed.). Weinheim: Wiley-VCH. p. 6. ISBN 9783527407415, 2008.
- [84] Medaustron website, <https://www.medaustron.at/en>.
- [85] News, Technological update 52 MeV beam generated: <https://polaris.brighterir.com/public/advancedoncotherapy/news/rns/story/xompdmr>.
- [86] Panttechnik website, <http://www.panttechnik.com/>.
- [87] C. Ronsivalle et al., First acceleration of a proton beam in a side coupled drift tube linac, *EPL Journal*, vol. 111, p. 14002, 2015.
- [88] News, Advanced Oncotherapy hails contribution of landlord as development of London proton beam facility passes important milestone: <https://www.proactiveinvestors.co.uk/companies/news/224253/advanced-oncotherapy-hails-contribution-of-landlord-as-development-of-london-proton-beam-facility-passes-important-milestone-224253.html>.
- [89] A. Degiovanni, P. Stabile, D. Ungaro, LIGHT: A linear accelerator for Proton Therapy. A.D.A.M. SA, Geneva, Switzerland on behalf of A.D.A.M. SA, In *2016 North American Particle Accelerator Conference*, Chicago, IL, USA, 2016, pp. FRB1I002, <https://doi.org/10.18429/JACoW-NAPAC2016-FRB1I002>.
- [90] A.M. Lombardi, V.A. Dimov, M. Garlasché, A. Grudiev, S. Mathot, E. Montesinos, S. Myers, M. Timmins, M. Vretenar. Beam dynamics in a high frequency RFQ, in *Proceedings of the 6th International Particle Accelerator Conference, IPAC'15*, Richmond, USA, 2015.

- [91] M. Vretenar, V. Dimov, M. Garlaschè, A. Grudiev, B. Koubek, A. Lombardi, S. Mathot, D. Mazur, E. Montesinos, M. Timmins, High-frequency compact RFQs for medical and industrial applications, in *Proceedings of the 29th Linear Accelerator Conference, LINAC16*, TH1A06, 2017, <https://doi.org/10.18429/JACoW-LINAC2016-TH1A06>.
- [92] M. Vretenar, A. Dallochio, V. A. Dimov, M. Garlasché, A. Grudiev, A.M. Lombardi, S. Mathot, E. Montesinos, M. Timmins. A Compact High-Frequency RFQ for Medical Applications, A Compact High-Frequency RFQ for Medical Applications. In *Proceedings of the 27th Linear Accelerator Conference, LINAC14*, Geneva, Switzerland, THPP040, 2014, <https://cds.cern.ch/record/2062619>.
- [93] V. Dimov, M. Caldara, A. Degiovanni, L. Esposito, D.A. Fink, M. Giunta, A. Jeff, A. Valloni, A. Lombardi, S. Mathot, M. Vretenar. Beam Commissioning of the 750 MHz Proton RFQ for the LIGHT Prototype. In *Proceedings of the 9th International Particle Accelerator Conference, IPAC'18*, Vancouver, Canada, pp. 658-660, TUPAF002, 2018, <https://doi.org/10.18429/JACoW-IPAC2018-TUPAF002>.
- [94] R. Moser, M. Cerv, S. Magnoni, H. Pavetits, P. Paz Neira K. Stachyra, Control and Interlock Systems for the LIGHT Prototype. In *Proceedings of the 16th Int. Conf. on Accelerator and Large Experimental Control Systems (ICALEPCS17)*, Barcelona, Spain, pp. 1683-1687, 2017, <https://doi.org/10.18429/JACoW-ICALEPCS2017-THPHA130>.
- [95] B. Koubek, A. Grudiev, M. Timmins. RF measurements and tuning of the 750 MHz radio frequency quadrupole. *Phys. Rev. Accel. Beams* 20, 080102, 2017, <https://doi.org/10.1103/PhysRevAccelBeams.20.080102>.
- [96] A. Brandt, Development of a Finite State Machine for the Automated Operation of the LLRF Control at FLASH, University of Hamburg, 2007-05-25.
- [97] J. Broere, B. Krietenstein, H. Kugler, U. Ratzinger, M. Vretenar, High Power Conditioning of the 202 MHz IH Tank 2 at the CERN LINAC3. In *Proceedings of the 19th International Conference, LINAC'98*, Chicago, USA, August 23-28, pp. 771-773, 1998.
- [98] Linac4 project, <http://linac4-project.web.cern.ch/linac4-project/>.
- [99] L. HEIN, A. LOMBARDI, Upd ate of the Linac4-PSB Transfer Line, CERN, Geneva, Dec. 2010, <https://cds.cern.ch/record/1326339>.
- [100] J.B. Lallement, A. Akroh, G. Bellodi, J.F. Comblin, V.A. Dimov, et al., First commissioning experience with the LINAC4 3 MeV front-end at CERN, CERN CDS, 2013.
- [101] ISOLDE Radioactive Ion Beam facility, <http://isolde.web.cern.ch/>.

- [102] C. Rossi, P. Bourquin, J.B. Lallement, A.M. Lombardi, S.J. Mathot, A. Timmins, G. Vandoni, M. Vretenar, S. Cazaux, O. Delferrière, M. Desmons, R.D. Duperrier, A. France, D. Leboeuf, O. Piquet. The Radiofrequency Quadrupole Accelerator for the Linac4. In *Proceedings of the Linear Accelerator Conference, LINAC08*, Victoria, BC, Canada, pp. 157-159, 2008.
- [103] F. Gerigk editor, Conceptual design of the SPL II, a high-power superconducting H- linac at CERN, CERN Report, Geneva: CERN, p. 104, 2006, <https://doi.org/10.5170/CERN-2006-006>.
- [104] S.J. Mathot et al., Mechanical Design, Brazing and Assembly Procedures of the Linac4 RFQ. In *Proceedings of the International Particle Accelerator Conference, IPAC10*, Kyoto, Japan, 2010.
- [105] M. Arruat, S. Jackson, J.L. Nougaret and M. Peryt, Equipment software modelling for accelerator controls, in *Proceeding of the 10th International Conference on Accelerator and Large Experimental Physics Control Systems*, Geneva, Switzerland, 2005.
- [106] Timber application, <https://twiki.cern.ch/twiki/bin/view/ABPComputing/LhcDataStorage>.
- [107] M. Vretenar. Field emission measurements on RFQ2 and recalibration of the vane voltage. CERN-PS-RF-NOTE-97-11, CERN, Geneva, CERN-PS-RF-NOTE-97-11, Aug. 1997, <http://cds.cern.ch/record/957814>.